The Mechanical Behavior of Shales

Johannes Herrmann

Kumulative Univ.-Diss.

zur Erlangung des akademischen Grades

"doctor rerum naturalium"

(Dr. rer. nat.)

in der Wissenschaftsdisziplin Petrologie

Eingereicht an der

Mathematisch-Naturwissenschaftlichen Fakultät

Institut für Erd- und Umweltwissenschaften

der Universität Potsdam

Ort und Tag der Disputation: Potsdam, 22.05.2019

Hauptbetreuer: Prof. Dr. Georg Dresen
                                   Prof. Dr. Michael Alber

weitere Gutachter: Prof. Dr. Heinz Konietzky

Eidesstattliche Erklärung

Hiermit versichere ich an Eides statt, dass

- die eingereichte Arbeit oder wesentliche Teile derselben in keinem anderen Verfahren zur Erlangung eines akademischen Grades vorgelegt worden sind;

- bei der Anfertigung der Dissertation die Grundsätze zur Sicherung guter wissenschaftlicher Praxis der DFG eingehalten wurden, die Dissertation selbständig und ohne fremde Hilfe verfasst wurde, andere als die von mir angegebenen Quellen und Hilfsmittel nicht benutzt worden sind und die den benutzten Werken wörtlich oder sinngemäß entnommenen Stellen als solche kenntlich gemacht wurden.

Ort/Datum   Unterschrift

Abstract

The thesis comprises three experimental studies, which were carried out to unravel the short- as well as the long-term mechanical properties of shale rocks. Short-term mechanical properties such as compressive strength and Young's modulus were taken from recorded stress-strain curves of constant strain rate tests. Long-term mechanical properties are represented by the time–dependent creep behavior of shales. This was obtained from constant stress experiments, where the test duration ranged from a couple minutes up to two weeks. A profound knowledge of the mechanical behavior of shales is crucial to reliably estimate the potential of a shale reservoir for an economical and sustainable extraction of hydrocarbons (HC). In addition, healing of clay-rich forming cap rocks involving creep and compaction is important for underground storage of carbon dioxide and nuclear waste.

Chapter 1 introduces general aspects of the research topic at hand and highlights the motivation for conducting this study. At present, a shift from energy recovered from conventional resources e.g., coal towards energy provided by renewable resources such as wind or water is a big challenge. Gas recovered from unconventional reservoirs (shale plays) is considered a potential bridge technology.

In Chapter 2, short-term mechanical properties of two European mature shale rocks are presented, which were determined from constant strain rate experiments performed at ambient and in situ deformation conditions (confining pressure, $p_c \leq 100$ MPa, temperature, $T \leq 125$ °C, representing p_c, T - conditions at < 4 km depth) using a Paterson–type gas deformation apparatus. The investigated shales were mainly from drill core material of Posidonia (Germany) shale and weathered material of Bowland (United Kingdom) shale. The results are compared with mechanical properties of North American shales. Triaxial compression tests performed perpendicular to bedding revealed semibrittle deformation behavior of Posidonia shale with pronounced inelastic deformation. This is in contrast to Bowland shale samples that deformed brittle and displayed predominantly elastic deformation. The static Young's modulus, E, and triaxial compressive

strength, σ_{TCS}, determined from recorded stress-strain curves strongly depended on the applied confining pressure and sample composition, whereas the influence of temperature and strain rate on E and σ_{TCS} was minor. Shales with larger amounts of weak minerals (clay, mica, total organic carbon) yielded decreasing E and σ_{TCS}. This may be related to a shift from deformation supported by a load-bearing framework of hard phases (e.g., quartz) towards deformation of interconnected weak minerals, particularly for higher fractions of about 25 – 30 vol% weak phases. Comparing mechanical properties determined at reservoir conditions with mechanical data applying effective medium theories revealed that E and σ_{TCS} of Posidonia and Bowland shale are close to the lower (Reuss) bound. Brittleness B is often quoted as a measure indicating the response of a shale formation to stimulation and economic production. The brittleness, B, of Posidonia and Bowland shale, estimated from E, is in good agreement with the experimental results. This correlation may be useful to predict B from sonic logs, from which the (dynamic) Young's modulus can be retrieved.

Chapter 3 presents a study of the long-term creep properties of an immature Posidonia shale. Constant stress experiments (σ = const.) were performed at elevated confining pressures (p_c = 50 – 200 MPa) and temperatures (T = 50 – 200 °C) to simulate reservoir p_c, T - conditions. The Posidonia shale samples were acquired from a quarry in South Germany. At stresses below $\approx$ 84 % compressive strength of Posidonia shale, at high temperature and low confining pressure, samples showed pronounced transient (primary) creep with high deformation rates in the semibrittle regime. Sample deformation was mainly accommodated by creep of weak sample constituents and pore space reduction. An empirical power law relation between strain and time, which also accounts for the influence of p_c, T and σ on creep strain was formulated to describe the primary creep phase. Extrapolation of the results to a creep period of several years, which is the typical time interval for a large production decline, suggest that fracture closure is unlikely at low stresses. At high stresses as expected for example at the contact between the fracture surfaces and proppants added during stimulation measures, subcritical crack growth may lead to secondary and tertiary creep. An empirical power law is suggested to describe secondary creep of shale rocks as a function of stress, pressure and temperature. The predicted closure rates agree with typical production decline curves recorded during the extraction of hydrocarbons. At the investigated

conditions, the creep behavior of Posidonia shale was found to correlate with brittleness, calculated from sample composition.

In Chapter 4 the creep properties of mature Posidonia and Bowland shales are presented. The observed long-term creep behavior is compared to the short-term behavior determined in Chapter 2. Creep experiments were performed at simulated reservoir conditions of p_c = 50 – 115 MPa and T = 75 – 150 °C. Similar to the mechanical response of immature Posidonia shale samples investigated in Chapter 3, creep strain rates of mature Bowland and Posidonia shales were enhanced with increasing stress and temperature and decreasing confining pressures. Depending on applied deformation conditions, samples displayed either only a primary (decelerating) or in addition also a secondary (quasi-steady state) and subsequently a tertiary (accelerating) creep phase before failure. At the same deformation conditions, creep strain of Posidonia shale, which is rich in weak constituents, is tremendously higher than of quartz-rich Bowland shale. Typically, primary creep strain is again mostly accommodated by deformation of weak minerals and local pore space reduction. At the onset of tertiary creep most of the deformation was accommodated by micro crack growth. A power law was used to characterize the primary creep phase of Posidonia and Bowland shale. Primary creep strain of shale rocks is inversely correlated to triaxial compressive strength and brittleness, as described in Chapter 2.

Chapter 5 provides a synthesis of the experimental findings and summarizes the major results of the studies presented in Chapters 2 – 4 and potential applications in the Exploration & Production industry.

Chapter 6 gives a brief outlook on potential future experimental research that would help to further improve our understanding of processes leading to fracture closure involving proppant embedment in unconventional shale gas reservoirs. Such insights may allow to improve stimulation techniques aimed at maintaining economical extraction of hydrocarbons over several years.

Zusammenfassung

Die vorliegende Dissertation befasst sich mit drei separaten, experimentellen Studien, die durchgeführt wurden, um die mechanischen Eigenschaften, wie Druckfestigkeit, Elastizitätsmodul und Langzeit-Kriecheigenschaften von Schiefergesteinen zu untersuchen. Dabei wurden die aufgezeichneten Spannungs-Verformungskurven von kurzzeitigen (wenige Minuten) Deformationsexperimenten bei konstanter Verformungsrate genutzt, um mechanische Druckfestigkeit und elastische Parameter zu bestimmen. Um die zeitabhängigen Kriecheigenschaften zu charakterisieren, wurden Deformationstests bei konstanter Spannung durchgeführt. Hier variierte die Testdauer zwischen wenigen Minuten und zwei Wochen. Ein verbesserter Kenntnisstand auf diesem Gebiet ist notwendig, um das Potential eines unkonventionellen Schiefergesteinsreservoirs im Hinblick auf eine wirtschaftliche und nachhaltige Förderung von Kohlenwasserstoffen zuverlässig abzuschätzen.

Im ersten Kapitel wird eine allgemeine Einleitung in das Thema der Dissertation gegeben, wobei im Besonderen auf die Motivation für die vorliegende Studie eingegangen wird. Die Einleitung fokussiert sich dabei auf die aktuell vorherrschende Herausforderung, die Energieversorgung durch konventionelle Ressourcen, wie beispielsweise Kohle, durch regenerative Ressourcen, wie z.B. Wind oder Wasser, zu ersetzen. Üblicherweise wird der Energiezeugung aus unkonventionell gewonnenem Erdgas dabei die Rolle einer Brückentechnologie zugewiesen. Die Motivation zur Durchführung dieser Arbeit ist es, das mechanische Verhalten von Gasschiefern zu untersuchen, die auch in Europa einen substantiellen Beitrag zur Gasförderung liefern können.

Im Kapitel 2 werden die Ergebnisse von Experimenten dargestellt, die exemplarisch auf die Bestimmung der Druckfestigkeit und des Elastizitätsmoduls von zwei reifen, europäischen Schiefergesteinen abzielen. Dazu wurden in einer Gasdruckapparatur Deformationsexperimente an Proben durchgeführt die senkrecht zur Schichtung orientiert entnommen wurden. Die Versuche wurden bei konstanter Verformungsrate und bei nachgestellten in situ Umgebungsbedingungen bis etwa 4 km Tiefe durchgeführt (Manteldruck, $p_c \leq 100$ MPa, Temperatur, $T \leq 125$ °C). Die

untersuchten Schieferproben stammen hauptsächlich aus Kernmaterial von erbohrtem Posidonienschiefer aus Niedersachsen und aus englischen Bowlandschiefer, das aus natürlichen Aufschlüssen gewonnen wurde. Zusätzlich wurden einige nordamerikanische Schieferproben zum Vergleich untersucht. Die triaxialen Kompressionstests zeigen ein semi-sprödes Deformationsverhalten mit ausgeprägter inelastischer Verformung des untersuchten Posidonienschiefers, wohingegen sich Bowlandschiefer spröde und bis zum Bruch vorzugsweise elastisch verformt. Der Elastizitätsmodul, E, und die Druckfestigkeit, σ_{TCS}, weisen bei erhöhten Drücken und Temperaturen eine starke Abhängigkeit vom Manteldruck und der Gesteinsmineralogie auf. Der Einfluss von Temperatur und Verformungsrate auf E und σ_{TCS} ist dagegen vernachlässigbar. Mit ansteigendem Anteil an mechanisch weichen Mineralphasen, z.B. Ton, Glimmer und organisch gebundenem Kohlenstoff, nehmen E und σ_{TCS} der untersuchten Schiefergesteine ab. Dies ist durch eine verändertes Verformungsverhalten begründet, das von der Deformation eines lasttragenden Gerüstes aus mechanisch festen Mineralen, wie beispielsweise Quarz, bis zu einer Verformung von miteinander verbundenen mechanisch weichen Mineralen reicht. Der Übergang wurde ab einem Volumenanteil von etwa 25 – 30 vol% weicher Mineralphasen beobachtet. Beim Vergleich der experimentell ermittelten mechanischen Eigenschaften (E, σ_{TCS}) mit Vorhersagen, in denen die Zusammensetzung der Schiefer berücksichtigt wird (effective medium theories, Voigt-Reuss Grenzen) ist erkennbar, dass E und σ_{TCS} nahe an der unteren (Reuss) Grenze liegen. Die aus dem Elastizitätsmodul berechnete Sprödfestigkeit (brittleness, B) von Posidonien- und Bowlandschiefer stimmt gut mit dem gemessenen Spannungs-Verformungsverhalten überein. Die Sprödfestigkeit eines Gesteins wird oft als Indiz zur Abschätzung des möglichen Erfolges von Stimulationsmaßnahmen betrachtet. Daher ist der Zusammenhang zwischen elastischen Eigenschaften, die sich mit Ultraschallmessungen (sonic-log) in Bohrungen abschätzen lassen und dem mechanischen Verhalten von Gasschiefern für eine schnelle und kostengünstige Beurteilung wichtig.

Im dritten Kapitel werden die Langzeit-Kriecheigenschaften von Schiefergesteinen untersucht. Dafür wurden Deformationsexperimente bei konstanter Spannung (σ = konst.) und erhöhten Umlagerungsdrücken (p_c = 50 – 200 MPa) und Temperaturen (T = 50 – 200 °C) an

einem unreifen Posidonienschiefer, welcher in einem aktiven Steinbruch in Süddeutschland gewonnen wurde, durchgeführt. Bei Spannungen unterhalb ≈ 84 % der Druckfestigkeit des Schiefers und hohen Temperaturen und niedrigen Manteldrücken zeigen die deformierten Schieferproben transientes (primäres) Kriechen im semi-spröden Regime mit relativ hohen Verformungsraten. Der größte Teil der Deformation wird dabei durch die Verformung von mechanisch weichen Mineralphasen und Porenraumreduktion aufgenommen. Ein empirisches Potenzgesetz wurde aufgestellt, um die zeitabhängige primäre Kriechphase in Abhängigkeit von Manteldruck, Temperatur und Spannung zu charakterisieren. Dabei wurde festgestellt, dass ein mögliches Rissschließen über einen typischen Zeitraum von wenigen Jahren bei der Annahme von ausschließlich primären Kriechen unwahrscheinlich ist. Typischerweise entstehen an den Kotaktflächen zwischen hydraulisch stimulierten Rissen innerhalb der Schieferformation und dem Stützmittel, welches dem Stimulationsfluid hinzugefügt wird, um offene Risse aufrecht zu erhalten, hohe Differentialspannungen. Dadurch kann zusätzliches (subkritisches) Risswachstum initiiert werden, welches bei den untersuchten Proben unter hoher Differentialspannung zusätzlich zum primären auch zum sekundären und tertiären Kriechen bis zum Versagen der Probe führte. Bei Verwendung eines empirischen Potenzgesetzes zur Beschreibung der sekundären Kriechphase kann eine, im Vergleich zur primären Kriechregime, substanziell höhere Rissschließungsrate abgeschätzt werden. Diese erscheint wesentlich zuverlässiger, da sie mit den Zeiträumen typische gemessener Produktionsrückgänge einer Bohrung übereinstimmt. Zusätzlich wurde eine inverse Korrelation zwischen gemessener Verformung und Sprödigkeit, basierend auf der Schiefermineralogie, festgestellt.

In Kapitel 4 werden weiterführende Untersuchungen vorgestellt, in dem die Kriecheigenschaften von reifem Posidonien-und Bowlandschiefer gemessen und mit den mechanischen Eigenschaften, bestimmt in Kurzzeit-Deformationsversuchen bei konstanter Verformungsrate (Kapitel 2) verglichen werden. Dafür wurden Kriechversuche an Posidonien- und Bowlandschiefermaterial, wie in Kapitel 2 beschrieben, bei simulierten Reservoirdrücken und -temperaturen durchgeführt (p_c = 50 – 115 MPa, T = 75 – 150 °C). Auch für diese Schiefergesteine wurde eine erhöhte Verformung bei erhöhten Spannungen und Temperaturen und niedrigen

Manteldrücken gemessen. In Abhängigkeit von den vorherrschenden Deformationsbedingungen wiesen die Proben beider Schiefergesteine entweder nur eine primäre oder zusätzlichen zur primären auch eine sekundäre und tertiäre Kriechphase auf. Bei gleichem Umlagerungsdruck und gleicher Temperatur erwies sich der tonreiche Posidonienschiefer als deutlich weniger fest als der quarzreiche Bowlandschiefer. Während der Großteil der Deformation in der primären Kriechphase durch die Verformung von weichen Mineralen und Porenraumreduktion aufgefangen wurde, ist eine Mikrorissbildung bezeichnend für das tertiäre Kriechen. Um das primäre Kriechverhalten der unterschiedlichen Schiefergesteine zu charakterisieren, wurde auch hier ein Potenzgesetz genutzt, welches einen Vergleich mit den Kriecheigenschaften anderer Schiefergesteinen erlaubt. Die gewonnenen Ergebnisse zeigen eine deutliche inverse Korrelation zwischen primärer Verformung und der gemessenen Druckfestigkeit und der berechneten Sprödigkeit. Dies ermöglicht es die Langzeit-Kriecheigenschaften von Schiefergesteinen mit den, aus einem Kurzzeittest gemessenen, mechanischen Eigenschaften grob abzuschätzen, solange die angenommen Zeitintervalle zwischen zwei Stimulationsoperationen in dem in der Praxis typischen Zeitintervall von einigen Jahren liegt.

Im fünften Kapitel werden die erzielten Ergebnisse nochmals im Zusammenhang dargestellt. Hier wird im Besonderen auf eine potentielle Anwendung der Ergebnisse in der E & P - Industrie eingegangen.

Abschließend wird im sechsten Kapitel auf mögliche Experimente eingegangen, die zukünftig durchgeführt werden könnten, um unser Verständnis in Bezug auf die spannungsinduzierte Rissschließung in Schieferlagerstätten durch die Einbettung der Stützmittel in die Formation zu verbessern. Diese Erkenntnisse wären wiederum hilfreich, um eine ökonomische und nachhaltige Förderung von Kohlenwasserstoffen von stimulierten Bohrungen zu gewährleisten, die in unkonventionelle Lagerstätten abgeteuft wurden.

Statement of contribution

The cumulative thesis entitled 'The Mechanical Behavior of Shales' consists of two published peer-reviewed papers and one submitted paper that is currently under review. In two out of these three papers the Ph. D. candidate is the first author. The published articles and the submitted manuscript constitute individual single chapters of this thesis (Chapters 2, 3 and 4) with their own abstract, introduction, experimental technique, discussion, conclusion and acknowledgement. Additionally, a general introduction (Chapter 1) and conclusion (Chapter 5) as well as an outlook (Chapter 6) form the framework for the entire experimental efforts presented in this thesis. A combined reference list is given at the end of the thesis. The experimental findings are published or submitted for publication in:

Chapter 2: J. Herrmann, E. Rybacki, H. Sone and G. Dresen, 2018. "Deformation Experiments on Bowland and Posidonia Shale – Part I: Strength and Young's modulus at Ambient and In Situ p_c-T Conditions" published in *Rock Mechanics and Rock Engineering, doi: 10.1007/s00603-018-1572-4* was authored by the Ph. D. candidate. Revisions made by the co-authors helped to substantially improve the paper.

Chapter 3: E. Rybacki, J. Herrmann, R. Wirth and G. Dresen, 2018 "Creep of Posidonia Shale at elevated Pressure and Temperature" published in *Rock Mechanics and Rock Engineering, doi: 10.1007/s00603-017-1295-y* was authored by Dr. Erik Rybacki. The PhD candidate co-authored the paper.

Chapter 4: J. Herrmann, E. Rybacki, H. Sone and G. Dresen, 2018. "Deformation Experiments on Bowland and Posidonia Shale – Part II: Creep Behavior at In Situ p_c-T Conditions" submitted (under review) to Rock Mechanics and Rock Engineering, was authored by the Ph. D. candidate. Revisions made by the co-authors helped to substantially improve the manuscript.

Declaration

Danksagung

An erster Stelle gilt mein Dank meinem Betreuer und Doktorvater Georg Dresen, der es mir ermöglicht hat meine Doktorarbeit in der Sektion Geomechanik und Rheologie am GeoFoschungsZentrum (GFZ) Potsdam anzufertigen.

Besonders bedanken möchte ich mich bei meinem Mentor Erik Rybacki, der mich bei der Anfertigung der Arbeit und der Manuskripte in jeglicher Hinsicht permanent unterstützt hat und ohne welchen die Anfertigung der Dissertation mindestens die doppelte Zeit in Anspruch genommen hätte. Ich kann die Stunden nicht zählen, die wir gemeinsam damit verbracht haben über die erzielten Ergebnisse zu diskutieren. Außerdem hat er mich ständig dazu angeregt, kritisch die Beobachtungen zu begutachten. Zuletzt sei ihm auch für die sämtliche nichtwissenschaftliche Unterstützung besonders gedankt.

Nicht nur für die Lösung sämtlicher technischer Herausforderungen und für die Einführung in die Paterson–Apparatur, sondern auch für seinen Humor gilt mein großer Dank Michael Naumann. Stefan Gehrmann danke ich für die exzellente Anfertigung sämtlicher Probenpräparate. Hiroki Sone bin ich für seine fachliche Unterstützung, die die Qualität der Manuskripte erheblich verbessert haben, sehr dankbar Bei Rita Hamlischer möchte ich mich explizit für ihre ständige Unterstützung in sämtlichen Anliegen abseits der Dissertation bedanken.

Besonderer Dank gilt auch meinen Mit–Doktoranden Livia Nardini, Stephan Bentz und Bernhard Schuck, ohne welche nur die Hälfte aller Erkenntnisse „unraveled" geworden wären. Die vielen Gespräche zwischen uns waren die beste Unterstützung, die man sich nur wünschen kann. Ohne euch wären die letzten Jahre nur halb so schön gewesen.

Sebastian Rehde zusammen mit Werner, Pülz und Sam danke ich für die unzähligen Stunden an bester Laune, absurd-paradoxen Gesprächen und geteiltem Leid.

Zu guter Letzt möchte ich meiner Familie und Freunden für ihre uneingeschränkte Unterstützung in den letzten Jahren bedanken. Ihr seid die besten!

Table of contents

Chapter 1: General Introduction

1.1 Energy production from conventional and unconventional resources

Energy production from natural resources has more than doubled between 1971 and 2016 (**Fig. 1**). Although energy production still relies mostly on burning oil and coal in 2016, energy extracted from natural gas has grown significantly from $\approx$ 883 million tonnes oil equivalent (Mtoe) in 1971 up to $\approx$ 3027 Mtoe in 2016.
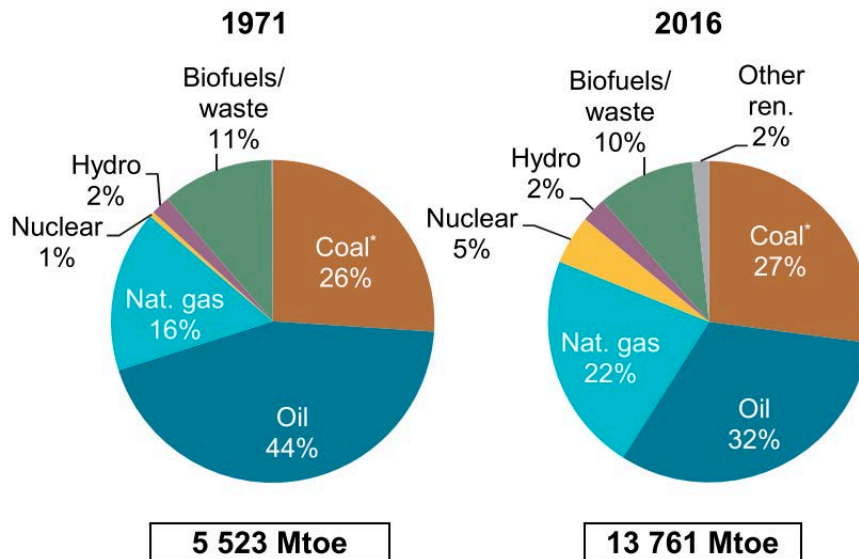
Figure 1 Total primary energy supply by fuel (International Energy Agency 2018)

A major technological and economic challenge is the replacement of conventional resources such as coal or oil by renewable energies, e.g., wind, solar or water. In Germany, the contribution of renewables to annual production of electric power has increased from about 8 % in 2003 to 40 % in 2018 (Burger 2018). However, we still rely on conventional resources to produce electricity or heat at least for the next decades considering a global increase in energy demand of $\approx$ 0.7 % per year (International Energy Agency 2018). Since many conventional reservoirs are increasingly

depleted, unconventional resources become progressively important. Several types of unconventional reservoirs exist: shale oil, oil sands, coal bed methane or shale gas. A common feature of these unconventional reservoirs is that the rocks have very low permeability and economic production requires more sophisticated technology compared to conventional reservoirs. Shale gas reservoirs are currently considered the most prospective unconventional reservoir type since energy provided from gas shales is believed to act as bridge technology between conventional and renewable resources and therefore is key to successfully implement the envisioned shift towards renewables (Hausfather 2015; Zhang et al. 2016). Therefore, the potential energy supply recovered from unconventional shale rocks has gained interest significantly during the past years. Several interdisciplinary initiatives such as GASH (Gas Shales in Europe) and SXT (ShaleXenvironmenT) have been performed, which aimed at investigating the prospects in Europe to economically and securely produce gas from shale reservoirs. Thus, we focus on shale plays as unconventional reservoir type in the following.

1.2 Shale gas exploitation

Energy recovered from unconventional rather than from conventional reservoirs may be regarded as 'clean' since burning gas releases $\approx$ 50 % less CO_2 than burning coal (Dong et al. 2018) and therefore has become of major interest over the past years (Kuchler 2017). In particular, the United States of America, which host an estimated technically recoverable shale gas volume of $\approx$ 2462 trillion cubic feet (tcf) (Energy Information Administration 2016) strongly invested in the extraction of gas from tight shale reservoirs (**Fig. 2**). The result is a nationwide gas production with > 62 % of unconventional shale gas in 2017 (Energy Information Administration 2018). The number is believed to be still increasing over the next decades.

trillion cubic feet

From Gas Wells   From Oil Wells   From Coalbed Wells   From Shale Gas Wells
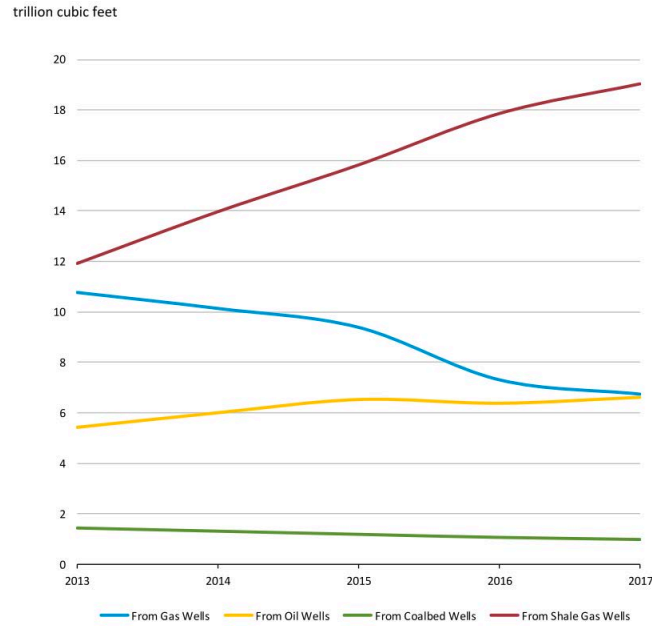
Figure 2 Gross withdrawals of natural gas in the United States, by type of well, 2013 – 2017 (Energy Information Administration 2018)

China with its huge shale plays such as the Tarim or South China Basin also shows a large potential to produce gas from shale gas reservoirs with an estimated technically recoverable shale gas volume of $\approx$ 1115 tcf (Energy Information Administration 2015a). Since China currently displays the largest Total Primary Energy Supply (TPES) (**Tab. 1**), the country strongly invests in the extraction of hydrocarbons (HC) from unconventional shale reservoirs. Currently the goal is that after a peak in carbon emissions by 2030 that emissions decrease rapidly afterwards as stated at the Asia-Pacific Economic Cooperation (APEC) forum 2014 (Guo et al. 2016). Along with the US and China, Europe shows as well a potential for an economical and sustainable production of gas from unconventional shale plays (Green et al. 2012; Gasparik et al. 2014).Potential shale gas reservoirs are expected in the Posidonia (Germany), the Alum (Denmark) or the Bowland-Hodder (England) formations, which are believed to contain relatively large amounts of hydrocarbons (Andrews 2013). The US Energy Information Administration reported an estimated technically recoverable shale gas volume of $\approx$ 16.9 tcf for the Posidonia and $\approx$ 31.7 tcf for the Alum shale (Energy Information Administration 2015b). For the Bowland shale, a technically recoverable shale gas volume of 822 – 2281 tcf was estimated (Andrews 2013).

Germany's government suggested to enhance the energy supply based on burning gas to overcome the energy production gap that is expected to arise as nuclear energy production will be fully terminated by 2022 in Germany (Horsfield et al. 2011).

Table 1 Total Primary Energy Supply (TPES) – top ten countries in 2016 and 1971

Country	TPES [Mtoe]	Share in world TPES [%]	
		2016	1971
People's Rep. of China	2958	22	7
United States	2167	16	29
India	862	6	3
Russian Federation	732	5	N/A
Japan	426	3	5
Germany	310	2	6
Brazil	285	2	1
Korea	282	2	0.3
Canada	280	2	3
Islamic Rep. of Iran	248	2	3
Rest of the world	5211	38	44
World	**13761**	**100**	**100**

Mtoe = million tonnes of oil equivalent, after (International Energy Agency 2018)

For a successful exploration and exploitation of unconventional reservoir rocks, also with respect to sustainability and the protection of the environment, a profound knowledge of the processes during the extraction of hydrocarbons is necessary. Commonly used extraction techniques, which have been applied in conventional reservoirs, are not applicable (Meier 2017). This is due to the almost impermeable matrix of shale rocks as well as their relatively low thickness. To overcome these restrictions, long deviated wells drilled horizontally within the target zones, also defined as 'sweet spots' are necessary to increase the inflow area for the hydrocarbons (Rickman et al. 2008). Typically, these 'sweet spots' are characterized by in situ stress state, rock brittleness, natural fracture network, high thermal maturity, porosity, permeability and content of organic material

(TOC), which is assumed to be directly correlated to the prospectivity of the shale formation. Based on several criteria such as mineralogy, geochemistry, petrology and geomechanical properties, these regions within a shale formation can be identified. In addition, repeated hydraulic fracturing (HF) stimulations need to be performed to create new fractures and to reactivate pre-existing cracks within the reservoir rocks to significantly increase the permeability of the shale formation (Li et al. 2015).

1.3 Fracture closure and proppant embedment

Although proppants made of quartz, ceramic or bauxite are added to the stimulation fluid to maintain open fractures created by HF, the productivity of a fractured well drilled in an unconventional reservoir typically declines over time following a hyperbolic or exponential trend (**Fig. 3**)(Hughes 2013; Wang 2016; Al-Rbeawi 2018). This may be either due to reservoir depletion, fracture sealing caused by fines migration or most likely due to proppant embedment-induced fracture closure with time (Sone and Zoback 2014; Wang 2016; Cerasi et al. 2017; Mittal et al. 2018).
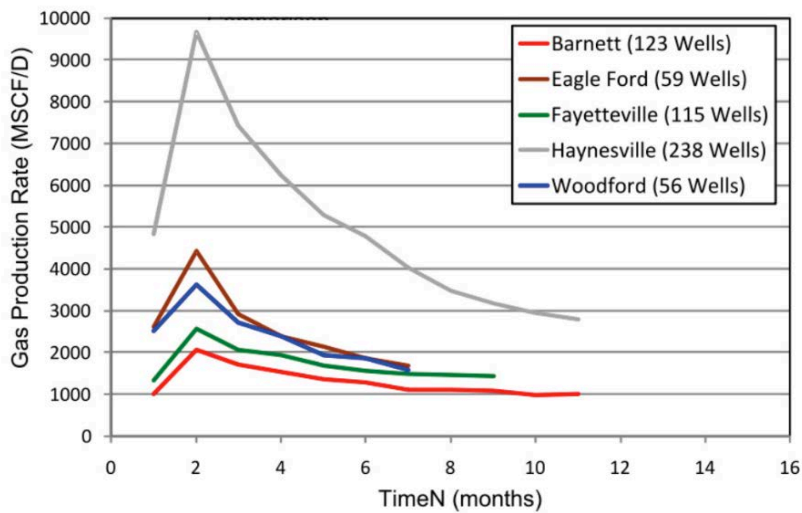
Figure 3 Gas production rate in different shale gas basins (Wang 2016)

The fracture closure rate due to proppant embedment in shale reservoirs is strongly influenced by confining pressure (p_c), temperature (T), stress conditions (σ), petrophysical properties as well as the short-term (strength, Young's modulus) and long–term (creep) properties of these rocks (**Fig. 4**) (Herrmann et al. 2018). We performed two deformations test at a constant load of $\sigma \approx 70$ MPa, $p_c = 75$ MPa, T = 90 °C, simulating reservoir p_c, T - conditions of about 3 km depth, on two fractured, different shale samples containing strong quartz proppants. One experiment was performed on relatively ductile Posidonia (POS) shale, which is rich in mechanically weak mineral phases (clay, mica, TOC). Using Scanning Electron Microscopy (SEM) on a polished thin section of the Posidonia sample shows that the strong proppants indent into the weak matrix of the shale (**Fig. 4a**). In contrast, indentation of quartz proppants into more brittle, quartz-rich Bowland (BOS) shale matrix is minor, but fines are generated by proppant crushing (**Fig. 4b**).
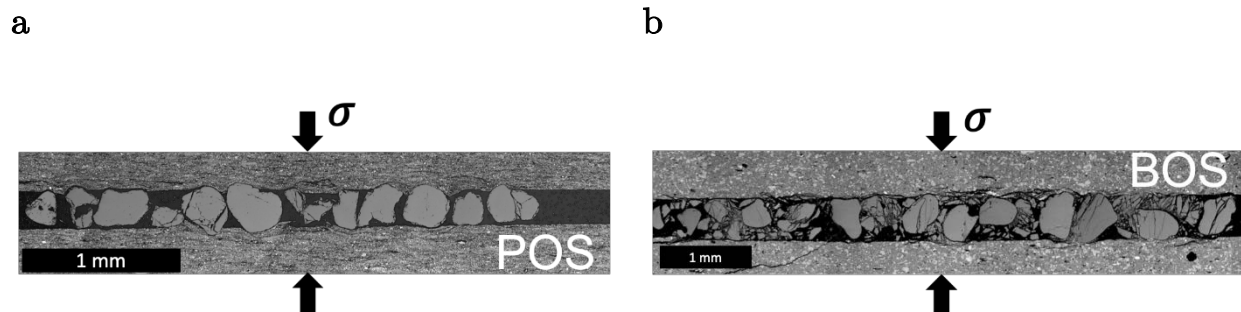
Figure 4 High resolution photographs (SEM) of deformed Posidonia (POS) (**a**) and Bowland (BOS) shale (**b**) including a mono layer of quartz proppants. Strong proppant agents indent into weak Posidonia shale matrix, but crush in strong Bowland shale, leading to fines generation. Samples were deformed at $p_c = 75$ MPa, T = 90 °C and $\sigma \approx 70$ MPa. Loading direction was perpendicular to bedding orientation.

This contrasting behavior clearly identifies the strong influence of shale composition as well as its mechanical properties on the indentation behavior of proppant agents into the shale matrix. Hence, knowledge of these parameters is required to make reliable estimations on the long-term productivity of a fractured well, which is helpful to increase their efficiency. Several studies on shale rocks were conducted to investigate the influence of confining pressure (Niandou et al. 1997; Petley 1999; Naumann et al. 2007; Kuila et al. 2011; Islam and Skalle 2013; Brantut et al. 2013),

temperature (Johnston 1987; Brantut et al. 2013; Masri et al. 2014) and stress conditions (Swan et al. 1989; Chong and Boresi 1990; Ibanez and Kronenberg 1993; Kwon and Kronenberg 1994; Brantut et al. 2013; Sone and Zoback 2013a; Rybacki et al. 2015, 2017) as well as petrophysical properties (Brantut et al. 2013; Rybacki et al. 2016; Cerasi et al. 2017; Morley et al. 2017; Teixeira et al. 2017) on the short-term and long-term properties of these rocks. However, these studies were mainly performed in such a way that the influence of only one of the mentioned parameters was investigated. In addition, the applied p_c, T and σ - conditions were relatively low, which is not representative of typical in situ conditions. Specifically, the performance of deformation tests at higher stresses can induce completely different mechanisms in the reservoir as can be seen from the performed experiments in **Fig. 4**. At lower stresses the strong quartz proppants in the Bowland shale would not be crushed leaving an open fracture without the generation of fines, which may not occur in the field.

Our motivation was to perform deformation experiments to be able to formulate a quantitative description of the constitutive behavior of typical gas shales. To this end we performed tests at constant strain rate and constant stress on different shale rocks. Since they are believed to be prospective unconventional European gas shales (Littke et al. 2011; Andrews 2013), samples from Posidonia shale (Germany) and Bowland shale (United Kingdom) were chosen. The tests were conducted at elevated confining pressures, temperatures and stresses to unravel the short-term (strength, Young's modulus) and long-term (creep) properties of the shales under in situ conditions. Knowing these parameters is key for a successful and economical production of hydrocarbons from these reservoir rocks. To account for the influence of these parameters we set up constitutive equations, which can be used to assess the shale properties at specific p_c, T and σ - conditions. Additionally, the obtained results may also be implemented into numerical models to improve the reliability of estimations made on the potential for an unconventional shale reservoir to economically produce gas.

Knowing these properties is the first step to estimate the time dependent fracture closure due to proppant embedment. Future experiments, which focus on the conductivity of fractured

shale samples including a proppant layer under in situ conditions will be performed to improve our knowledge on this topic.

Chapter 2: Strength and Young's modulus of Posidonia and Bowland shale at ambient and in situ p$_c$, T – conditions

1 Summary

The production of hydrocarbons from unconventional reservoirs, like tight shale plays, increased tremendously over the past decade. Hydraulic fracturing is a commonly applied method to increase the productivity of a well drilled in these reservoirs. Unfortunately, the production rate decreases over time presumably due to fracture closure. The fracture-closure rate induced by proppant crushing and embedment depends on mechanical properties of shales and proppants that are influenced by confining pressure (p$_c$), temperature (T), and shale composition.

We performed constant strain rate deformation tests at ambient and in situ conditions of a typical shale reservoir (p$_c$ ≤ 100 MPa, T ≤ 125 °C) using European shale samples exhibiting variable mineralogy, porosity and maturity. We focused on a comparison of Posidonia shale with Bowland shale, which is believed to be the most prospective shale formation in the United Kingdom. Compression tests were performed perpendicular to bedding orientation. Stress–strain curves show that Bowland shales are relatively strong and brittle compared to Posidonia shale which display a semibrittle deformation behavior. Brittleness estimated from elastic properties is in good agreement with the recorded stress–strain behavior but shows no clear relation to composition. Compressive strengths (σ_{UCS} = uniaxial compressive strength, σ_{TCS} = triaxial compressive strength) and static Young's moduli, E, reveal a strong confining pressure and mineralogy dependence, whereas temperature and strain rate only have a minor influence on σ_{TCS} and E. The coefficient of internal friction for both shales is ≈ 0.42 ± 0.03. With increasing amount of weak minerals (e.g., clay, mica) σ_{UCS}, σ_{TCS} and E strongly decrease. This may be related to a shift from deformation supported by a load–bearing framework of hard minerals to deformation of interconnected weak minerals at about 25 – 30 vol% of weak phases. At the applied conditions, the triaxial compressive strength and Young's moduli of most shales deformed normal to bedding are close to the Reuss bound.

To our knowledge, this is the first study, which presents results of experimental investigations carried out to characterize the mechanical behavior of Bowland shale. The observed results are helpful to estimate the potential of the Bowland reservoir with respect to the economical extraction of hydrocarbons.

List of symbols

ϕ	Porosity	τ	Shear strength
ρ	Density	S_0	Cohesion
p_c	Confining pressure	σ_n	Normal stress
T	Temperature	Q	Activation energy
T_a	Absolute temperature	R	Gas constant
σ_{UCS}	Uniaxial compressive strength	n, α, A	Constants
σ_{TCS}	Triaxial compressive strength		
E	Static Young's modulus		
$\dot{\varepsilon}$	Strain rate		
ε_{max}	Maximum axial strain before failure of specimen		
μ_i	Coefficient of internal friction		
M	Specific mechanical property (e.g., triaxial compressive strength, Young's modulus)		
f	Volumetric fraction		
J	Scaling parameter		
K	Bulk modulus		
μ	Shear modulus		
B_{min}	Brittleness determined from mineralogy		
B_E	Brittleness determined from Young's modulus		

2 Introduction

Providing energy from oil and gas recovered from unconventional hydrocarbon reservoirs, e.g., shale gas plays, is widely believed to act as bridge technology between conventional and renewable energy resources (Hausfather 2015; Zhang et al. 2016). Typically, these reservoirs exhibit low permeability, which makes an economical exploitation difficult (McGlade et al. 2013). To increase the productivity of a well drilled in these tight reservoir rocks, hydraulic fracturing (HF) is a suggested method to create artificial fractures which are expected to connect to natural fractures present in the reservoir (Li et al. 2015). In particular in North America with its shale formations exhibiting a large geographical extent such as the Haynesville, Marcellus or Bakken shale, HF was used in recent years as key technique for an economic exploitation of hydrocarbons (McGlade et al. 2013). Europe also shows potential for economical extraction of hydrocarbons from shale reservoirs e.g., from Posidonia (Germany) and Alum (Denmark) formations. In the United Kingdom the Bowland–Hodder (England) formation is believed to contain relatively large amounts of hydrocarbons (Andrews 2013).

Several criteria were developed to characterize regions within a formation representing the best potential for an economic hydrocarbon production, often defined as sweet spots, mainly based on geochemistry, petrology, mineralogy and geomechanical properties (Rickman et al. 2008; Sondergeld et al. 2010; Berard et al. 2012). To maintain fractures induced by hydraulic fracturing, proppants (ceramic, bauxite, quartz) are often added to the frac fluid. However, the production rate of a fractured well typically declines over time (Al-Rbeawi 2018; Wang 2016), due to depletion of the reservoir and possibly due to fracture closure processes (Cerasi et al. 2017; Wang 2016). Fracture closure is affected by confining pressure (Niandou et al. 1997; Petley 1999; Naumann et al. 2007; Kuila et al. 2011; Islam and Skalle 2013), temperature (Johnston 1987; Masri et al. 2014), non-isostatic stress conditions (Swan et al. 1989; Chong and Boresi 1990; Ibanez and Kronenberg 1993; Kwon and Kronenberg 1994a; Sone and Zoback 2013a; Rybacki et al. 2015, 2017) and petrophysical and mechanical properties such as mineralogy, porosity, permeability and brittleness of the reservoir rocks (Rybacki et al, 2016; Morley et al. 2017; Z. Li et al. 2017; Teixeira et al. 2017; Cerasi et al. 2017). Therefore, knowledge of the geomechanical behavior of shale rocks with

respect to the above mentioned parameters is important to better understand their fracture closure behavior (Morley et al. 2017; Ilgen et al. 2017; Kikumoto et al. 2017; Z. Li et al. 2017; Cerasi et al. 2017).

We performed deformation experiments at constant strain rates and ambient and elevated confining pressures and temperatures up to 100 MPa and 125 °C to investigate the mechanical properties of various, particularly European, shale rocks with different mineralogy, focusing on the comparison between Posidonia shale and Bowland shale. The latter is poorly investigated so far but expected to be a very prospective shale play (e.g., Smith et al. 2010; Imber et al. 2014; Hough et al. 2014). Here we establish empirical relations between mechanical properties (strength, Young's modulus) and confining pressure, temperature and strain rate, which are important in the petroleum industry (Draege et al. 2006; Farrokhrouz et al. 2014), e.g., for assessment of borehole stability and evaluation of stable mud weight windows for drilling or hydraulic fracturing (Warpinski et al. 2009; Britt and Schoeffler 2009; Soliman et al. 2012; Meier et al. 2013, 2015; Gholami et al. 2014). The results are also helpful to correlate with data measured during in situ operations such as wire line well logging (Horsrud 2001; Chang et al. 2006). Constant stress (creep) experiments performed on similar shales at ambient and elevated confining pressures and temperatures will be presented in a companion paper to improve our understanding of the fracture closure behavior of shale rocks.

3 Sample material

Various black shales mainly from different formations throughout Europe were investigated. Samples include Cambrian Alum (DK) shale (core sample depth z ≈ 17 m), Carboniferous Bowland (UK) shale and Lower Jurassic Posidonia (GER) shale. The latter formation is represented by 3 different localities 1) Haddessen (HAD, overmature gas shale), 2) Harderode (HAR, peak oil maturity), and Dotternhausen (DOT, immature oil shale). HAD and HAR shales were recovered at shallow depth (z ≈ 58 – 61 m) from old drill cores of research wells in N–Germany (e.g., Gasparik et al. 2014), whereas DOT shale was collected from freshly blasted blocks of a quarry in S–Germany

(e.g., Rybacki et al. 2015). Alum shale (ALS) is highly overmature and was recovered from fresh cores of the Skelbro–2 well (e.g., Ghanizadeh et al. 2014). Mature to overmature Bowland (BOS) shales are divided into Upper (BOS1 – 7, BOS11 – 14, BOS_OC) and Lower Bowland shales (BOS8 – 10) (Yang et al. 2015). Samples BOS1 – 10 (z ≈ 2076 – 2719 m) were recovered from drill cores from the Preese Hall 1 well (PH1) drilled in 2010 (e.g., Green et al. 2012) and samples BOS11 – 14 (z ≈ 32 – 80 m) were derived from the MHD13 well drilled in Marl Hill Moor (MHM). Because of limited availability of Upper Bowland core samples, we collected also Upper Bowland shale samples (BOS_OC) from an outcrop located within the county of Lancashire (NW England). For comparison, we examined an immature and an overmature North American shale (Haynesville, overmature and Marcellus, immature) recovered from unknown depth.

Mineral composition of all samples was determined by X – ray diffraction analysis (XRD) and reveals a mixture of quartz (Qtz), feldspar (Fsp), pyrite (Py), carbonates (Cb), clay (Cly), mica (Mca) and organic matter (TOC). Porosity (incl. micro pores) varies between 1 – 15 % (**Tab. 1**) and was measured on cylindrical samples (length = 20 mm, diameter = 10 mm) by He – pycnometry, after storing the samples for at least 48 h in an oven at 50 °C.

Chapter 2: Strength and Young's modulus of Posidonia and Bowland shale at ambient and in situ p^c, T - conditions

Table 1 Mineralogical composition, density and organic constant of investigated samples

Sample	Depth [m]	VRr [%]	ρ [$\frac{g}{cm^3}$]	ϕ [vol%]	TOC [vol%]	Cly [vol%]	Mca [vol%]	Cb [vol%]	Qtz [vol%]	Py [vol%]	Fsp [vol%]	CTMP [vol%]	Cb [vol%]	QFP [vol%]	Experiment
HAD	60.8	1.2	2.36	10	12	32	0	46	8	2	0	50	41	9	T
HAR	58.2	0.9	2.46	3	11	32	0	40	15	2	0	53	30	17	U, T
DOT	surface	0.6	2.14	11	17	20	0	47	14	2	0	43	43	14	T
ALS	17.2	3.6	2.73	12	16	55	0	0	26	3	0	73	0	27	T
MAS	unknown	0.3	2.66	2	/	/	/	/	/	/	/	/	/	/	T
HSV	unknown	3.8	2.41	11	/	/	/	/	/	/	/	/	/	/	T
BOS1	2076.2	0.8	2.68	3	2	0	3	70	22	1	2	7	69	24	U, T
BOS2	2078.1	/	2.65	3	3	3	6	18	66	2	2	14	17	69	U, T
BOS3	2079.2	/	2.66	1	3	0	2	62	31	1	1	8	60	32	U, T
BOS4	2080.3	/	2.67	2	2	0	4	61	31	1	1	6	61	33	T
BOS5	2087.1	/	2.70	3	2	0	3	56	37	1	1	7	55	38	U, T
BOS6	2342.5	/	2.61	2	4	0	7	7	78	1	3	11	7	82	U, T
BOS7	2344.7	/	2.65	2	1	0	3	23	68	1	4	7	23	70	U, T
BOS8	2718.4	3.8	2.70	2	2	0	2	59	36	1	0	7	58	35	T
BOS9	2595.7	/	2.65	1	6	3	0	61	30	0	0	9	61	30	T
BOS10	2490.7	/	2.63	3	3	4	6	27	58	1	1	15	26	59	T
BOS11	32.4	0.8	2.16	15	16	0	11	29	42	1	1	35	26	39	T
BOS13	69.3	/	2.67	7	0	3	0	65	32	0	0	10	61	29	T
BOS14	80.4	/	2.38	12	5	2	0	8	85	0	0	17	7	76	T
BOS_OC	surface	0.9	2.51	8	5	4	9	8	71	2	1	23	8	69	U, T

Sample abbreviation that were used during uniaxial (U) and triaxial (T) experimental procedure, HAD = Haddessen, HAR = Harderode, DOT = Dotternhausen → Posidonia formation; MAS = Marcellus; HSV = Haynesville; BOS1 – 7 → Upper Bowland formation (PH1); BOS8 – 10 → Lower Bowland formation (PH1); BOS11 – 14 → Upper Bowland formation (MHM), BOS_OC → Upper Bowland formation (OC = Outcrop). VRr (vitrinite reflectance) is maturity. CTMP (= Cly + TOC + Mica + ϕ), Cb and QFP (= Qtz + Fsp + Py) display weak, intermediate and strong phases in vol %

Vitrinite reflectance, calculated from T_{max} (Jarvie et al. 2005), accounting for thermal maturity of investigated samples ranges from 0.6 to 3.8 VRr %. Bulk density of samples was calculated from the ratio of weight and volume of prepared cylindrical specimens, yielding values between 2.14 and 2.73 $\frac{g}{cm^3}$. Petrophysical data of all investigates samples are listed in **Tab. 1.** Note that composition data are presented here in vol % instead of wt %, since only the volumetric fraction and spatial distribution is of interest for mechanical behavior. To convert wt% to vol% the following density, ρ, values were assumed: 2.65 $\frac{g}{cm^3}$ for Qtz, 2.6 $\frac{g}{cm^3}$ for Fsp, 5.01 $\frac{g}{cm^3}$ for Py, 2.71 $\frac{g}{cm^3}$ for Cb, 2.5 $\frac{g}{cm^3}$ for Cly, 2.82 $\frac{g}{cm^3}$ for Mca and 1.3 $\frac{g}{cm^3}$ for TOC, respectively (Rybacki et al. 2015). Note that in **Tab. 1** columns 6 – 12 refer to vol% of individual phases calculated from measured wt%, whereas volume fractions given in columns 13 – 15 are renormalized taking into account the pore volume. CTMP displays the cumulative amounts of clay, TOC, mica and porosity and QFP represents the sum of quartz, feldspar and pyrite constituents. With respect to the mechanical properties, CTMP and QFP are considered as weak and strong constituents, respectively. Cb constituents are regarded as intermediate strong. **Fig. 1a** reveals that both Posidonia and Alum shale are clay-rich whereas Bowland shales are either quartz-or carbonate-rich, except for one Upper Bowland sample from the Marl Hill Moor well. The Upper Bowland outcrop sample contains higher fractions of clay than core derived samples. Unfortunately, no XRD-mineral data of investigated Haynesville and Marcellus shale exists. (**Fig. 1a**). Cylindrical samples (10 mm diameter x 20 mm length) with parallel end surfaces were prepared perpendicular to bedding for triaxial deformation experiments. In addition, for uniaxial tests cuboids with 2 x 2 x 4 mm in size were cut perpendicular to bedding. The sample size was adapted to the uniaxial deformation apparatus. Scanning electron microscopy reveals a very fine-grained matrix (d ≤ 20 µm) of Posidonia (HAR, **Fig. 2a**) and Upper Bowland (BOS_OC, **Fig. 2d**) shale with preferred alignment of organic matter and phyllosilicates defining the bedding orientation. All specimens were dried at 50 °C for at least 48 h before the deformation experiments were performed.

a

b

c
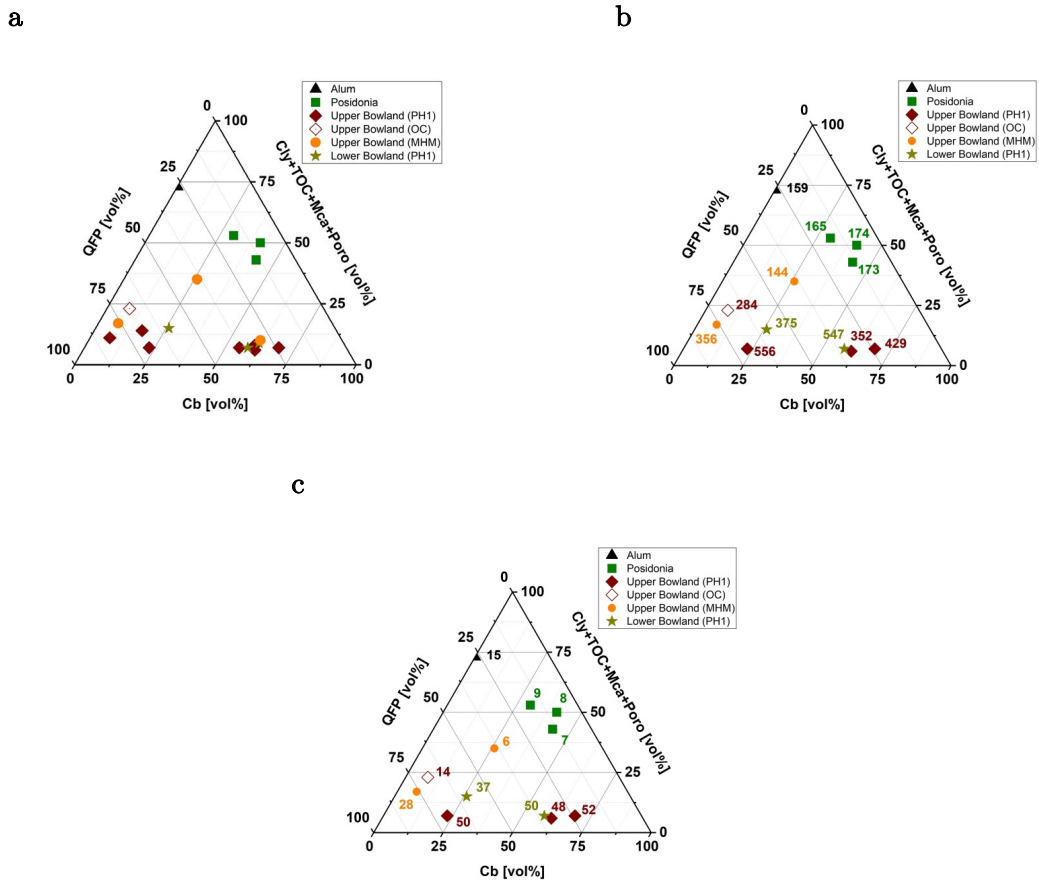
Figure 1 (**a**) Ternary plots displaying mineral composition of investigated samples. Composition is separated into mechanically strong (QFP = Qtz + Fsp + Py), intermediate strong (Cb) and weak (Cly + TOC + Mca + Poro) fractions. Qtz = quartz, Fsp = feldspar, Py = pyrite, Cb = carbonate, Cly = clay, TOC = total organic carbon, Mca = mica, Poro = porosity. Mineral data are given in vol%, normalized to 100 vol% taking also the sample porosity into account. Alum and Posidonia shales are clay-rich, whereas Bowland shales are either carbonate-or quartz-rich. Outcrop samples of Bowland shale reveal higher amounts of weak material than core derived samples. Superimposed values are indicating triaxial compressive strength, σ_{TCS}, in [MPa] (**b**) and static Young's modulus, E, in [GPa] (**c**). PH1 = Preese Hall 1, OC = outcrop, MHM = Marl Hill Moor
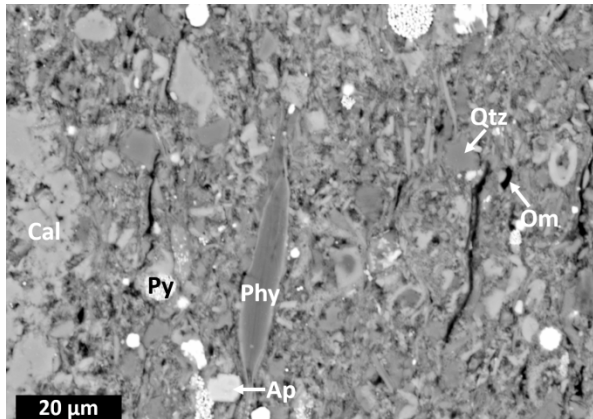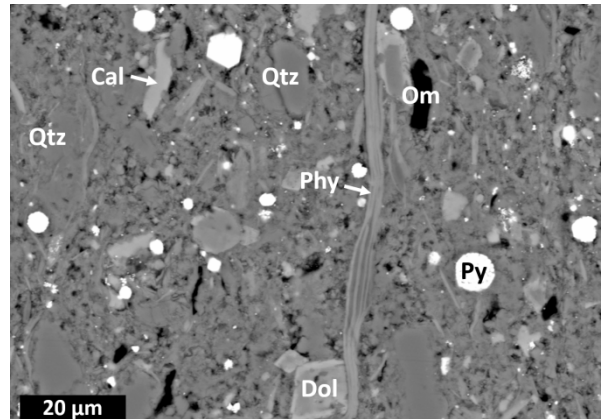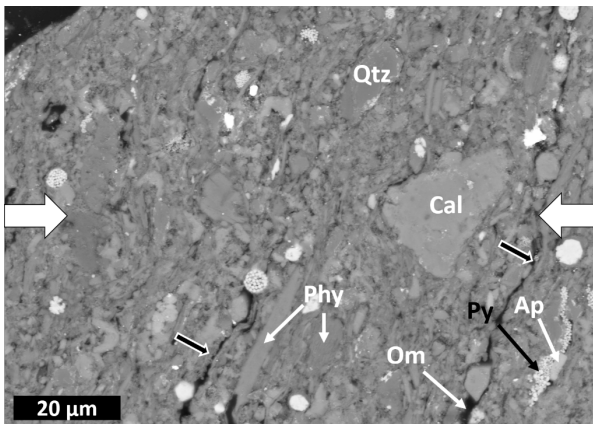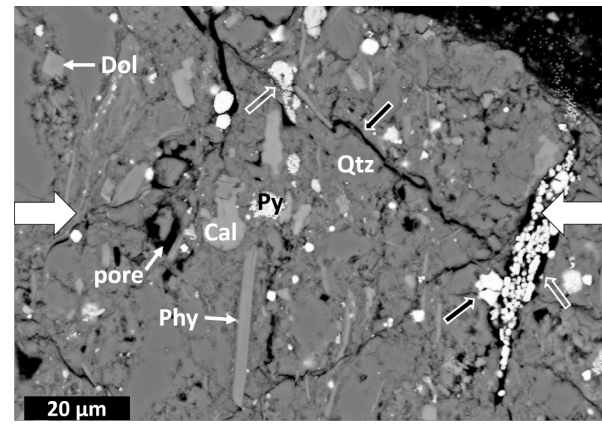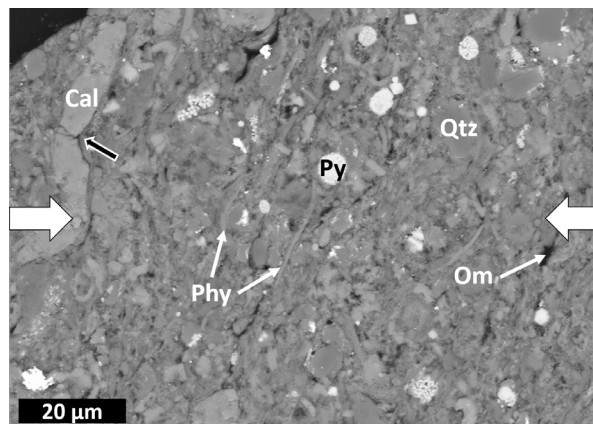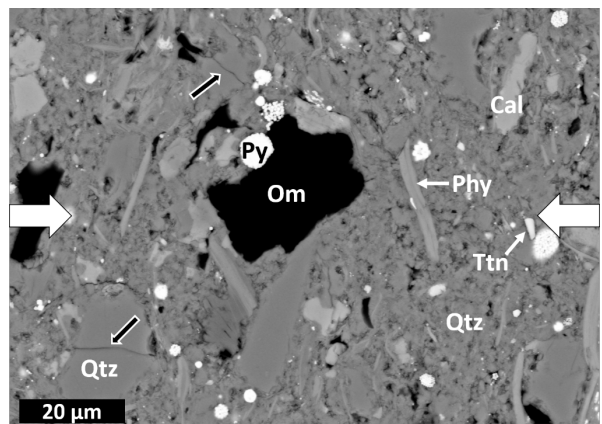
Figure 2 SEM-backscattered (BSE) images (**a** − **c**) of low porosity ($\approx$ 3 %) Posidonia shale (HAR) and (**d** − **f**) porous ($\approx$ 8 %) Bowland shales (OC). (**a**) and (**d**) show undeformed samples. The remaining images were taken from samples deformed at p_c = 50 MPa, T = 100 °C and $\dot{\varepsilon} = 5 * 10^{-4}$ s^{-1}. Bold white arrows indicate the loading direction, which was always perpendicular to bedding. Main mineral constituents of both shales are phyllosicates (Phy), calcite (Cal), dolomite (Dol), quartz (Qtz) and pyrite (Py) in addition to organic matter (Om). Accessory minerals are apatite (Ap) and titanite (Ttn), respectively. Pores and organic matter appear nearly black, quartz is medium grey, phyllosicates and carbonates (Cal + Dol) are light grey and pyrite is almost white. Long black lines are unloading cracks perpendicular to the loading direction. (**b, c**) Deformation microstructures in Posidonia shale sample close to main shear fracture (upper left corner) are crushed and smeared pyrite aggregates, intercrystalline fractures subparallel to the main fracture (**b**, bold black arrows) and broken calcite grains (**c**, bold black arrow). With increasing distance from the main fracture no deformation microstructures were observed in Posidonia shale samples. (**e**) Deformed Bowland shales show formation of inter-as well as intracrystalline fractures (bold black arrows) close to the main fracture (upper right corner). In addition, framboidal pyrite is squeezed and smeared along and perpendicular to fractures, respectively (open white arrow). (**f**) At larger distance from the main fracture in Bowland shale less deformation microstructures are visible, such as intracrystalline fractures within quartz grains (**f**, bold black arrow).

4 Experimental Technique

Mechanical Data: Triaxial deformation experiments were performed at elevated confining pressures (p_c = 50, 75 and 100 MPa), temperatures (T = 75, 100 and 125 °C) and constant strain rates ($\dot{\varepsilon} = 5 * 10^{-6}$, $5 * 10^{-5}$ and $5 * 10^{-4}$ s^{-1}) using a Paterson-type deformation apparatus (Paterson 1970). Argon gas was used as confining pressure medium. Samples were covered by thin (wall thickness $\approx$ 0.35 mm) copper jackets to prevent gas intrusion into the specimen. Axial load was recorded by an internal load cell, installed within the pressure vessel. Assuming constant volume deformation, axial stresses calculated from measured forces were corrected for copper jacket strength, determined from previous calibration runs. Axial strain was calculated from recorded displacement and corrected for system compliance. Accuracies of resulting axial peak stresses and strains are $\pm$ 4 and $\pm$ 6 %, respectively.

Uniaxial compression tests were performed at ambient confining pressure (p_c = 0.1 MPa) and temperature (T = 20 °C) using a uniaxial creep rig with a modified electro-mechanical actuator (Freund et al. 2004; Götze et al. 2010). Shale samples were uniaxially deformed at strain rates of $\dot{\varepsilon} = 2.5 - 5 * 10^{-4}$ s^{-1}. Axial strain was determined from measured displacement and corrected for the stiffness of the apparatus, resulting in errors of calculated axial strains $<$ 5 %.

The Young's modulus, E, is given here as the tangent modulus measured at $\approx$ 50 % of the peak stress in recorded stress-strain curves. The tangent modulus was used since the secant modulus would ignore effects of pore closure at the beginning of performed experiments, mainly accounting for tests performed at ambient conditions (**Fig. 3a**). Using instead the secant modulus determined from the slope of the stress-strain curves from the origin to the strain at $\approx$ 50 % of the peak stress would result on average in $\approx$ 20 % higher Young's moduli of triaxially deformed samples. Due to the relatively high system compliance of both apparatuses, accuracy of E determined at uniaxial and triaxial conditions is $\pm$ 13 % and $\pm$ 20 %, respectively.

The post peak stress-strain deformation behavior of many of the samples could not be measured due to violent specimen failure. The low stiffness of both apparatuses resulted in a large amount of elastic energy stored in the loading frame that is abruptly released at sample failure. Typically, failure occurred at maximum axial strains of $\approx$ 1 – 2 % for uniaxial and $\approx$ 1.5 – 20 % for triaxial deformation, depending on applied p_c, T, stress - conditions and mineral composition. Most experiments were terminated after failure. Only few specimens displayed deformation to a barrel shaped sample (**Figs. 3a, 4a, 4b**).

Detailed **microstructural observations** were performed on mechanically polished, carbon-coated thin sections using a scanning electron microscope (SEM, Zeiss Ultra 55 Plus), operating at 20 kV in backscatter electron (BSE) mode. Energy dispersive X-ray (EDX) measurements and semi-quantitative geochemical analysis were performed on the samples.

5 Results

In total, we conducted 8 uniaxial compression and 34 triaxial compressions tests (**Tab. 2 - 4**). First, we present results of uniaxial experiments obtained at ambient confining pressure and temperature and subsequently data of triaxial tests performed at elevated p_c, T - conditions. For HAR and BOS_OC samples, additional tests were performed varying either $\dot{\varepsilon}$, p_c or T.

5.1 Mechanical properties – uniaxial

Uniaxial compression tests were mainly focused on Upper Bowland shales since their mechanical properties were hardly investigated so far. All tests were performed with loading direction perpendicular to bedding. The stress-strain curves reveal predominantly elastic and minor inelastic deformation prior to reaching peak stresses of up to about 320 MPa. Beyond peak stress, most samples failed abruptly (**Fig. 3a**). Uniaxial compressive strength, σ_{UCS}, of the shale samples range from 75 to 318 MPa, with lower and upper limits represented by Posidonia and Bowland (core) shales, respectively. Commonly, deformed samples failed by forming a single shear fracture or by axial splitting. Bowland shale samples prepared from drill cores are noticeably stronger than samples collected from surface outcrop and both are distinctively stronger than Posidonia shale. This is attributed to the difference in mineralogical composition and porosity between Posidonia and Bowland shales (**Fig. 1**). Axial strain at peak stress is lower for Bowland samples from cores compared to outcrop samples. The static Young's modulus, E, derived from the tangent modulus varies between 6 and 34 GPa (**Tab.2**). As shown in **Fig. 3b,** the uniaxial compressive strength increased almost linearly with increasing static Young's modulus. The effect of mineralogy on the mechanical properties obtained from stress-strain behavior will be explained in more detail in section 5.1 below.

Table 2 Mechanical data of samples obtained at ambient conditions (p$_c$ = 0.1 MPa, T = 20 °C, $\dot{\varepsilon}$ = 2.5 – 5*10^{-4}s^{-1})

sample	σ_{UCS} [MPa]	E [GPa]	ε_{max} [%]
HAR	75	6	2
BOS1	256	33	1
BOS2	227	26	1
BOS3	255	30	1
BOS5	318	33	1
BOS6	280	24	1
BOS7	309	34	1
BOS_OC	156	11	2

σ_{UCS} = uniaxial compressive strength, E = static Young's modulus, ε_{max}.= maximum axial strain before failure. For sample abbreviations see caption of Table 1.
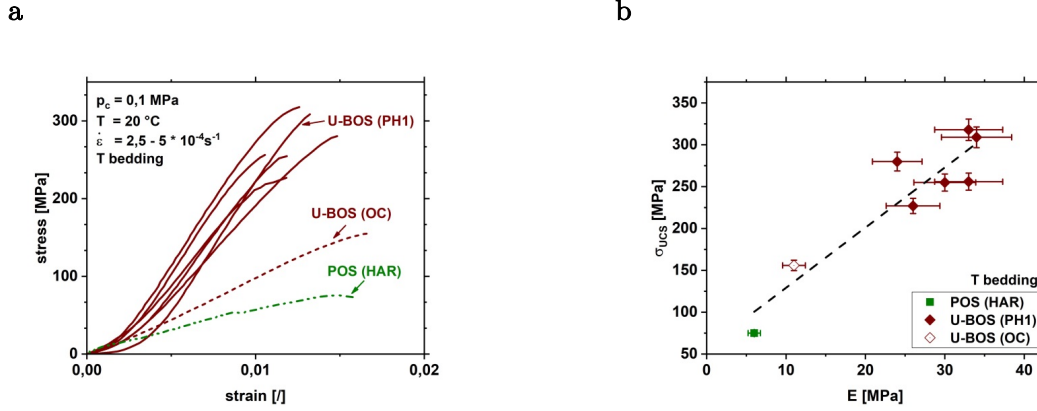
Figure 3 Stress-strain curves of samples deformed at ambient confining pressure and temperature (**a**) and empirical cross-correlation between uniaxial compressive strength, σ_{UCS}, and static Young's modulus, E, (**b**). Loading direction is perpendicular to bedding. U – BOS = Upper Bowland shale, POS = Posidonia shale, HAR = Harderode, OC = outcrop, PH1 = Preese Hall 1

5.2 Mechanical properties – triaxial

Triaxial compression tests were performed at constant strain rates of $\dot{\varepsilon}$ = 5 * 10^{-6}, 5 * 10^{-5} and 5 * 10^{-4} s^{-1}, confining pressures of p_c = 50, 75 and 100 MPa and temperatures of T = 75, 100 and 125 °C. One set of experiments performed on European and American shale samples aimed at unravelling the effect of mineral composition and porosity on the mechanical behavior at fixed $\dot{\varepsilon}$, p_c, T - conditions. A second series of tests was performed on Bowland outcrop samples and Posidonia shale to study the influence of varying deformation conditions on the mechanical behavior. All tests were performed with loading direction perpendicular to bedding.

5.2.1 Effect of mineral composition and porosity on mechanical properties

To investigate the influence of petrophysical properties on the mechanical behavior of the samples, we performed constant strain rate experiments at 50 MPa confining pressure, 100 °C temperature and strain rate of 5 * 10^{-4} s^{-1}. The tests conditions were chosen to represent in situ conditions at 2 – 3 km depth.

In uniaxial and triaxial tests, the relative strengths of Bowland and Posidonia shales are similar (**Fig. 4a, b, cf., Fig. 3a**). The triaxial compressive strength, σ_{TCS}, and static Young's modulus, E, of triaxially deformed samples are about 75 % and 40 % higher on average compared to measurements at ambient conditions (**Tab. 3**). Maximum axial strains reached before failure occurred were also larger by about $\approx$ 1 % at triaxial conditions (**Fig. 4a, Tab. 2,3**).

a

b

c
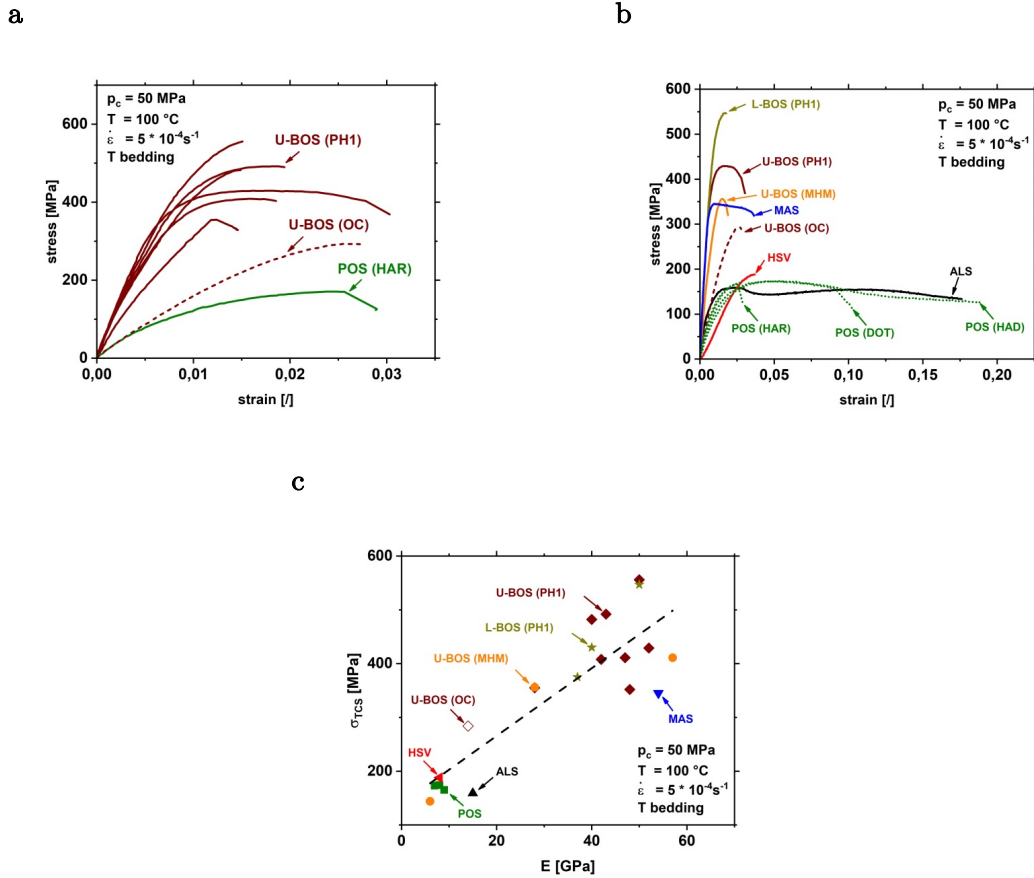
Figure 4 Representative stress-strain curves of deformed shales (**a, b**) under triaxial conditions and empirical relation between triaxial compressive strength, σ_{TCS}, and static Young's modulus, E, (**c**). Deformation conditions are indicated. U – BOS = Upper Bowland shale, L – BOS = Lower Bowland shale, HSV = Haynesville shale, MAS = Marcellus shale, ALS = Alum shale, POS = Posidonia shale, HAR = Harderode, DOT = Dotternhausen, HAD = Haddessen, OC = outcrop, PH1 = Preese Hall 1, MHM = Marl Hill Moor

Table 3 Mechanical data of samples obtained at elevated p_c, T - conditions (p_c = 50 MPa, T = 100 °C, $\dot{\varepsilon}$ = 5*10^{-4} s^{-1})

sample	σ_{TCS}[MPa]	E [GPa]	B$_{min}$	B$_{E}$	ε_{max} [%]
HAD	174	8	0.18	0.21	19
HAR	165	9	0.28	0.22	3
DOT	173	7	0.26	0.20	10
ALS	159	15	0.39	0.29	18
MAS	345	54	/	0.58	4
HSV	188	8	/	0.21	4
BOS1	429	52	0.38	0.57	3
BOS2	482	40	0.74	0.49	1
BOS3	408	42	0.47	0.51	2
BOS4	352	48	0.47	0.54	2
BOS5	492	43	0.51	0.51	2
BOS6	355	28	0.82	0.41	1
BOS7	556	50	0.80	0.56	2
BOS8	547	50	0.47	0.56	2
BOS9	430	40	0.31	0.49	1
BOS10	375	37	0.68	0.47	1
BOS11	144	6	0.45	0.18	9
BOS13	411	57	0.32	0.60	1
BOS14	356	28	0.87	0.41	2
BOS_OC	284	14	0.74	0.28	3

σ_{TCS} = triaxial compressive strength, E = static Young's modulus, B = Brittleness determined from mineralogy (min) and static Young's modulus (E). For sample abbreviations see caption of Table 1.

In general, deformed shales display brittle to semibrittle mechanical behavior. Small inelastic axial strain and hardening followed by abrupt failure indicate brittle deformation. In contrast, semibrittle deformation exhibits pronounced non-linear hardening before peak stress and post-peak stable weakening (Evans et al. 1990; Evans and Kohlstedt 1995). Clay-rich Posidonia (HAD, DOT) and Alum shales with high porosity displayed semibrittle deformation at low triaxial compressive strength ($\sigma_{TCS} \approx$ 160 – 175 MPa) (**Fig. 4b**). In contrast, also clay-rich but low-porosity Posidonia (HAR) (σ_{TCS} = 165 MPa) and Haynesville (σ_{TCS} = 188 MPa) shale specimens displayed brittle deformation with predominantly elastic deformation and minor hardening before failure occurred. Marcellus and Bowland shale samples deformed brittle, irrespective of porosity and contents of

strong (QFP) and intermediate strong (Cb) minerals. Marcellus and Bowland shales were much stronger ($\sigma_{TCS} \approx 280 - 550$ MPa) than the other investigated shale rocks (**Fig. 4b, Tab. 3**). In general, static Young's moduli were larger at elevated pressures and for samples displaying high triaxial compressive strength (**Fig. 4c**). At failure, a single shear fracture formed in the triaxially deformed shale samples except for sample BOS11. Ductile deformation of specimen BOS11 resulted in a barrel-shaped specimen after deformation. This is likely due to a relatively high porosity and TOC content of sample BOS11. Specimen HAD (Posidonia) was still intact when we stopped the experiment at 19 % axial strain (**Tab. 1**).

5.2.2 Effect of confining pressure on strength

To characterize the influence of confining pressure on the mechanical properties of Posidonia (HAR) and Upper Bowland outcrop shales (BOS_OC), we performed deformation tests at constant strain rate ($\dot{\varepsilon} = 5 * 10^{-4}$ s^{-1}), temperature (T = 100 °C) and confining pressures of $p_c =$ 50, 75 and 100 MPa (**Tab. 4**). Upper Bowland shale samples for these tests were exclusively prepared from outcrop material as no more core material was available. At elevated confining pressures and increasing maximum axial strain, low-porosity, clay-rich Posidonia shales revealed a change from post-peak strain weakening towards steady-state deformation (**Fig. 5a**). This transition indicates a switch from brittle to semibrittle deformation with increasing confining pressure as also described by Rybacki et al. (2015) for Posidonia (DOT) shales.

Table 4 Mechanical data of samples

sample	p$_c$ [MPa]	T [°C]	$\dot{\varepsilon}$ [s^{-1}]	σ_{TCS} [MPa]	E [GPa]
HAR	0.1	20	$5 * 10^{-4}$	75	6
	50	100	$5 * 10^{-4}$	165	9
	75	100	$5 * 10^{-4}$	214	10
	100	100	$5 * 10^{-4}$	222	10
HAR	50	75	$5 * 10^{-4}$	202	11
	50	125	$5 * 10^{-4}$	178	10
HAR	50	100	$5 * 10^{-5}$	189	10
	50	100	$5 * 10^{-6}$	175	9
BOS_OC	0.1	20	$5 * 10^{-4}$	156	11
	50	100	$5 * 10^{-4}$	284	14
	75	100	$5 * 10^{-4}$	335	15
	100	100	$5 * 10^{-4}$	352	15
BOS_OC	50	75	$5 * 10^{-4}$	282	14
	50	125	$5 * 10^{-4}$	271	13
BOS_OC	50	100	$5 * 10^{-5}$	289	13
	50	100	$5 * 10^{-6}$	285	14

p$_c$ = confining pressure, T = temperature, $\dot{\varepsilon}$ = strain rate, σ_{TCS} = triaxial compressive strength, E = static Young's modulus. For sample abbreviations see caption of Table 1.
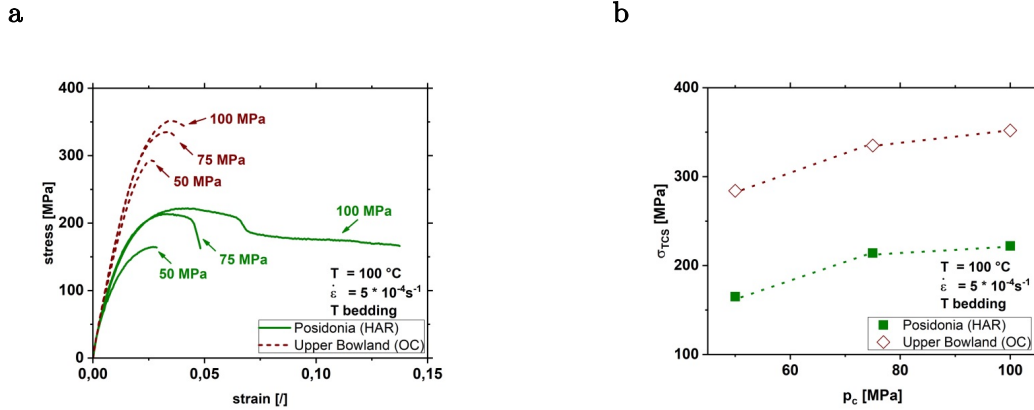
Figure 5 Influence of confining pressure p$_c$ on stress-strain behavior (**a**) and triaxial compressive strength, σ_{TCS}, (**b**) of Posidonia (HAR) and Upper Bowland (OC) shale. σ_{TCS} increases with confining pressure for both shales. Deformation conditions are indicated. HAR = Harderode, OC = outcrop

The deformed quartz-rich Bowland shale samples (BOS_OC) failed abruptly along a localized single shear fracture, independent of the applied confining pressure (**Fig. 5a**). Axial strain at peak stress increased only slightly with confining pressure but deformation remained brittle. The triaxial compressive strength of Posidonia and Bowland shales increased with increasing confining pressure (**Fig. 5b, Tab. 4**), also observed by Rybacki et al. (2015) and Ibanez and Kronenberg (1993) for Posidonia (DOT) and Wilcox shales, respectively (for description of microstructures see section 4.3 below). Assuming a lithostatic effective pressure gradient of 25 MPa/km, the observed confining pressure dependence would result in an increase of triaxial compressive strength of Posidonia and Bowland shales of ≈ 23 and ≈ 40 MPa/km, respectively. The triaxial compressive strength of BOS_OC ($\phi \approx 8$ %) shale was more sensitive to confining pressure changes compared to Posidonia – HAR ($\phi \approx 3$ %) shale (**Tab.1**). Maximum axial strains before failure of Posidonia shale samples were more affected by confining pressure compared to Bowland shale. Presumably this is due to a much higher clay content of (HAR) Posidonia shale (32 vol%) than present in Bowland outcrop samples (4 vol%). The static Young's moduli of Posidonia and Bowland shales remained nearly constant showing no significant change with increasing confining pressure (**Tab. 4**). This was also observed by Rybacki et al. (2015) for other Posidonia shales and for US shale rocks (Sone and Zoback 2013a).

5.2.3 Effect of temperature on strength

For the same shale types (Posidonia (HAR) and BOS_OC), deformation experiments were also performed at different temperatures (T = 75, 100, 125 °C) while keeping the confining pressure (p_c = 50 MPa) and strain rate ($\dot{\varepsilon}$ = 5 * $10^{-4}s^{-1}$) constant (**Tab. 4, Fig. 6**). In general, the influence of temperature on strength was small between 75 and 125 °C. (**Fig. 6a**). The stress-strain curves reveal a small decrease of σ_{TCS} and a slightly increasing axial strain at peak stress with increasing temperature, which is more pronounced for Posidonia than for Bowland shale (**Fig. 6b, Tab. 4**). This may be related to a relatively high amount of clays in Posidonia shale, which dehydrate at higher temperatures (Mikhail and Guindy 1971) leading to a triaxial compressive strength decrease due to stress corrosion (subcritical crack growth) (Brantut et al. 2014). Samples subjected to elevated temperatures showed formation of an incipient single shear fracture. No significant influence of temperature on static Young's modulus could be observed (**cf., Tab. 4**). Assuming a geothermal gradient of 25 °C/km, the observed temperature sensitivity would result in a decrease of triaxial compressive strength of Posidonia and Bowland shales of ≈ 12 and ≈ 6 MPa/km depth, respectively. This is considerably lower than the confining pressure-induced triaxial compressive strength increase per km depth, in particular for Bowland shale. Consequently, the confining pressure induced increase of strength, $\sigma_{TCS,}$ – will not be compensated by the observed temperature induced σ_{TCS} – reduction, assuming a linear correlation between σ_{TCS} and confining pressure and temperature.
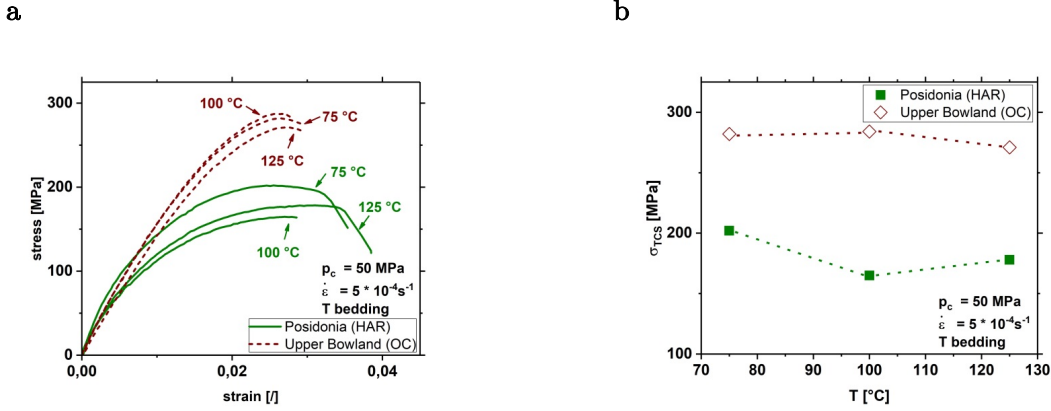
Figure 6 Influence of temperature, T, on stress-strain behavior (**a**) and triaxial compressive strength, σ_{TCS}, (**b**) of Posidonia (HAR) and Upper Bowland (outcrop) shale. σ_{TCS} is reduced slightly with increasing temperature. HAR = Harderode, OC = outcrop

5.2.4 Effect of strain rate on strength

At constant confining pressure (p$_c$ = 50 MPa) and constant temperature (T = 100 °C) Posidonia and Bowland shales were deformed at varying strain rates of $\dot{\varepsilon}$ of $5 * 10^{-6}$, $5 * 10^{-5}$ and $5* 10^{-4}$ s^{-1}, respectively (**Tab. 4**). We observed no significant effect of strain rate on the mechanical behavior of the investigated shale samples (**Fig. 7a, Fig. 7b, Tab. 4**). For Posidonia shale samples, axial strains at peak stresses slightly increased with decreasing strain rates, likely related to the high fraction of weak phases (Chong et al. 1976, 1980; Rybacki et al. 2015). Also, the static Young's modulus remained almost constant at varying deformation rates (**cf., Tab. 4**).
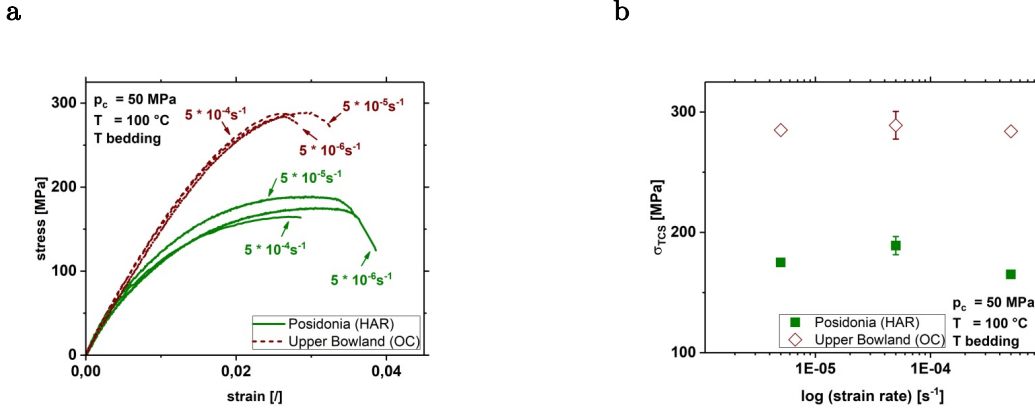
Figure 7 Effect of strain rate, $\dot{\varepsilon}$, on stress-strain behavior of Posidonia and Upper Bowland (outcrop) shale (**a**). Triaxial compressive strength, σ_{TCS}, remains nearly constant within errors at increasing strain rate (**b**). HAR = Harderode, OC = outcrop

5.3 Microstructures

All samples, except for one, failed spontaneously along a single shear fracture. The shear fractures are inclined at an angle of $\varphi \approx 35 \pm 2$ ° with respect to the sample axis. This indicates an apparent coefficient of internal friction of $\mu_i \approx 0.7 \pm 0.05$. Note that sample shape, end effects, length-diameter ratio of the sample and sample jacketing may affect the measurements of the coefficient of internal friction. Only sample BOS11 did not fracture but remained intact and displayed barreling. This sample contained significantly higher porosity, a large fraction of sheet silicates and organic matter.

Microstructures of HAR and BOS_OC samples deformed at pressures of p_c = 50 MPa, temperature T = 100 °C and strain rates of $\dot{\varepsilon}$ = 5 * 10 $^{-4}$ s^{-1} were investigated using scanning electron microscopy (SEM).

In general, microstructural inspection of deformed samples only showed deformation structures close to the macroscopic single shear fracture. We observed mainly inter- and intracrystalline microcracks, indentation of strong into weaker mineral phases and stretching of framboidal pyrite. In deformed Posidonia samples the main fracture is surrounded by a damage zone with subparallel intercrystalline microcracks (bold black arrows in **Fig. 2b**), sheared pyrite

minerals and in few cases, intracrystalline fracturing of calcite grains (**Fig. 2c**, bold black arrow). At slightly larger distance from the macro crack, no deformation structures could be identified in the micrographs. Bowland shales reveal formation of inter- and intragranular microcracks close to the main fracture (bold black arrows in **Fig. 2e**). Pyrite is crushed and smeared along these fractures (open white arrows). With increasing distance from the main fracture, only intracrystalline fractures are found in few quartz grains (bold black arrows in **Fig. 2f**).

6 Discussion

The shale samples investigated in this study showed mainly brittle to semibrittle deformation behavior at confining pressures and temperatures ranging from 0.1 to 100 MPa and 20 to 125 °C, respectively (**Figs. 3a, 4b, 5a, 6a, 7a**). Brittle deformation is defined by minor inelastic axial strain and hardening and abrupt failure along a localized shear fracture. Semibrittle deformation shows pronounced non-linear hardening before peak stress is reached, which is followed by weakening. Microstructures of deformed Posidonia (HAR) and Bowland (BOS_OC) shales indicate mostly brittle deformation only close to the macro fracture. Undulose extinction, grain boundary sliding or rotation of grains could not be identified.

Uniaxial and triaxial compressive strength, maximum axial strain at peak stress and static Young's modulus are affected by mineralogical composition, organic matter content, porosity and on the applied experimental conditions (confining pressure, temperature and strain rate) as previously described for other shales (Ibanez and Kronenberg 1993). In the following we will first discuss the role of material parameters starting with sample composition and then address the effect of loading conditions.

6.1 Sample composition

Here we attempt to identify possible correlations between sample composition and mechanical properties such as σ_{UCS}/ σ_{TCS}, static Young's modulus, E, and maximum axial strain before failure, ε_{max}, measured perpendicular to bedding. Sample composition varied significantly between shale

types but main constituents are porosity, ϕ, fractions of strong (QFP), intermediate strong (carbonate) and weak (Clay + TOC + Mica) mineral phases.

The influence of strong components (QFP) (**Fig. 8a**) and carbonates (**Fig. 8b**) on the uniaxial compressive strength, σ_{UCS}, of Posidonia and Upper Bowland shales is minor when measured at ambient conditions ($p_c = 0.1$ MPa, T = 20 °C). This is in good agreement with results of Tan et al. (2014) for shales recovered from the Upper Yangtze Platform (China). For Posidonia shales, Rybacki et al. (2015) found a similar correlation between uniaxial compressive strength measured normal to bedding and the volumetric content of carbonates and QFP. However, Upper Bowland samples were found to be weaker with increasing amounts of weak materials (**Fig. 8c**). Tan et al. (2014) found a similar relationship for Lower Silurian shale. Sample porosity had no significant influence on the uniaxial compressive strength within error bars (**Tab. 2**), in contrast to results published by Rybacki et al. (2015) and Tan et al. (2014). We found a strong correlation between uniaxial compressive strength, σ_{UCS}, and Young's moduli, E, (**Fig. 3b**). The static Young's modulus does not correlate with porosity or the fraction of strong and intermediate strong components (**Tab. 3**) but clearly decreased with increasing amounts of weak phases (**Fig. 8d**).
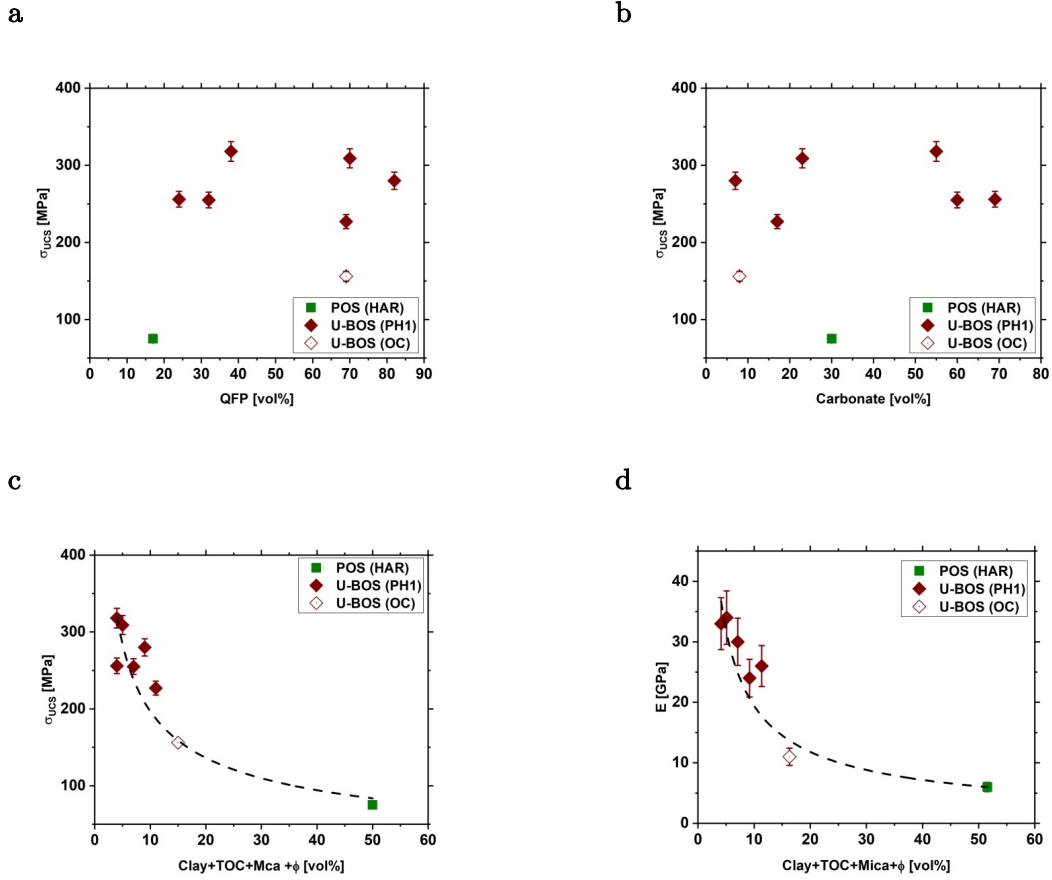
Figure 8 Influence of mineralogy in terms of volumetric fraction of QFP = quartz + feldspar + pyrite (**a**), carbonate (**b**), clay + TOC + mica (**c**) on uniaxial compressive strength, σ_{UCS}, and static Young's moduli, E, (**d**) of investigated shales. Data were obtained at ambient experimental conditions. The relation between fraction of weak phases and uniaxial compressive strength and Young's modulus is indicated by a dashed line in (**c**) and (**d**), respectively. The corresponding equations are: $\sigma_{UCS}[MPa] = 669[MPa] * (Clay + TOC + Mca + \phi)^{-0,53}$ (R^2 = 0,92) and $E[GPa] = 101[GPa] * (Clay + TOC + Mca + \phi)^{-0,72}$ (R^2 = 0,92). HAR = Harderode, PH1 = Preese Hall 1, OC = outcrop

Interestingly, the maximum axial strain before failure at ambient conditions appeared to increase slightly with increasing amounts of strong components (**Fig. 9a**) and to decrease with increasing carbonate fraction (**Fig. 9b**). Porosity and amounts of weak components had no effect on maximum axial strain before failure (**Tab. 2**).
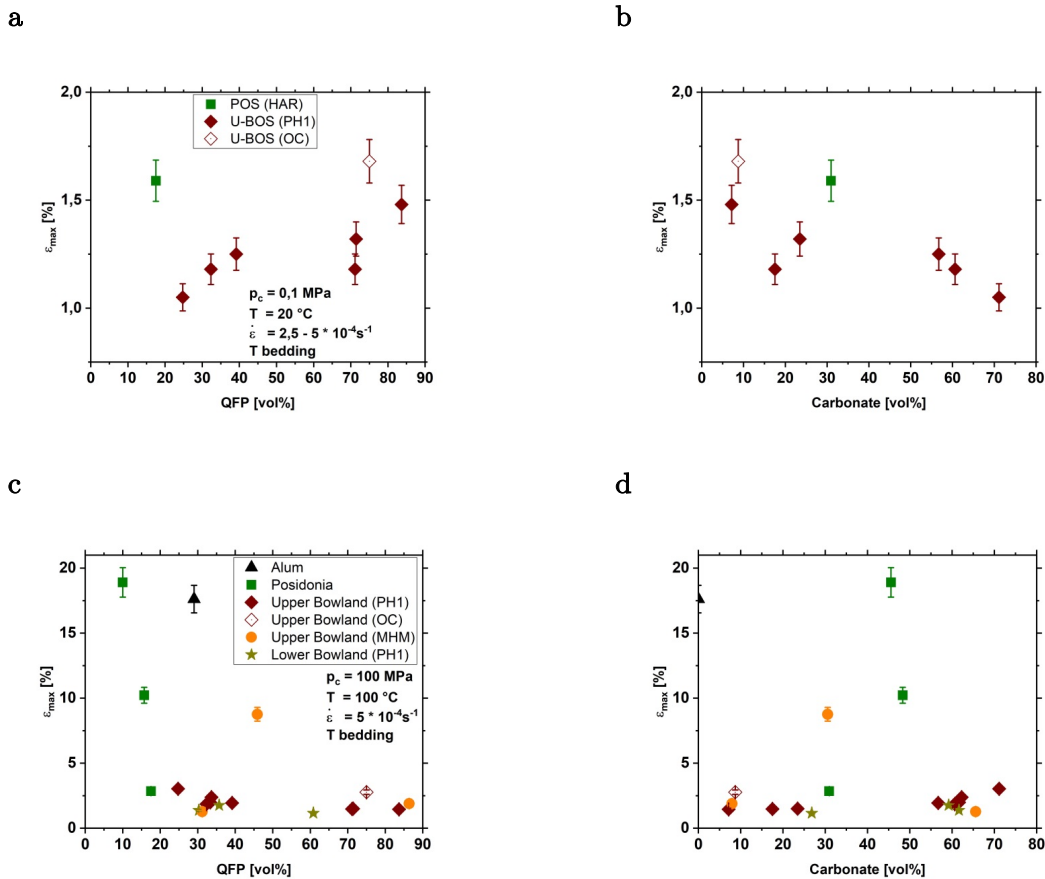
Figure 9 Effect of volumetric fraction of QFP = quartz + feldspar + pyrite (**a, c**) and carbonate (**b, d**) on max. axial strain ε_{max} reached before failure of shale shales. Experiments were performed at ambient conditions (**a, b**) and elevated (**c, d**) confining pressures and temperatures. HAR = Harderode, PH1 = Preese Hall 1, OC = outcrop, MHM = Marl Hill Moor

Similar to σ_{UCS}, the triaxial compressive strength, at 50 MPa confining pressure and 100 °C temperature, was independent of the content of strong (**Fig. 10a**) and intermediate strong (**Fig. 10b**) minerals. In contrast, Rybacki et al. (2015) found increasing triaxial compressive strength with increasing fractions of these components. This is likely due to different p$_c$, T - conditions of the tests, influencing the strength of individual sample constituents and affecting the correlations between mechanical properties and sample mineralogy. In addition, any differences in microstructure or water content (drying of the samples) are expected to influence the deformation behavior. Water-rich shale rocks are believed to exhibit lower triaxial compressive strength and static Young's modulus than dried samples, for example due to swelling of smectite clay minerals

occurring within shales (cf., Vales et al. 2004) and due to a reduction of the effective pressure. Examples are given by Rybacki et al. (2015) for Alum shale and by Ibanez and Kronenberg (1993) for Wilcox shale. Therefore, the drying procedure applied to our samples may not represent in situ conditions and our obtained strength and Young's modulus values overestimate the mechanical properties under natural conditions. However, drying of samples allows a better comparison of shale rocks recovered from different formations or localities.
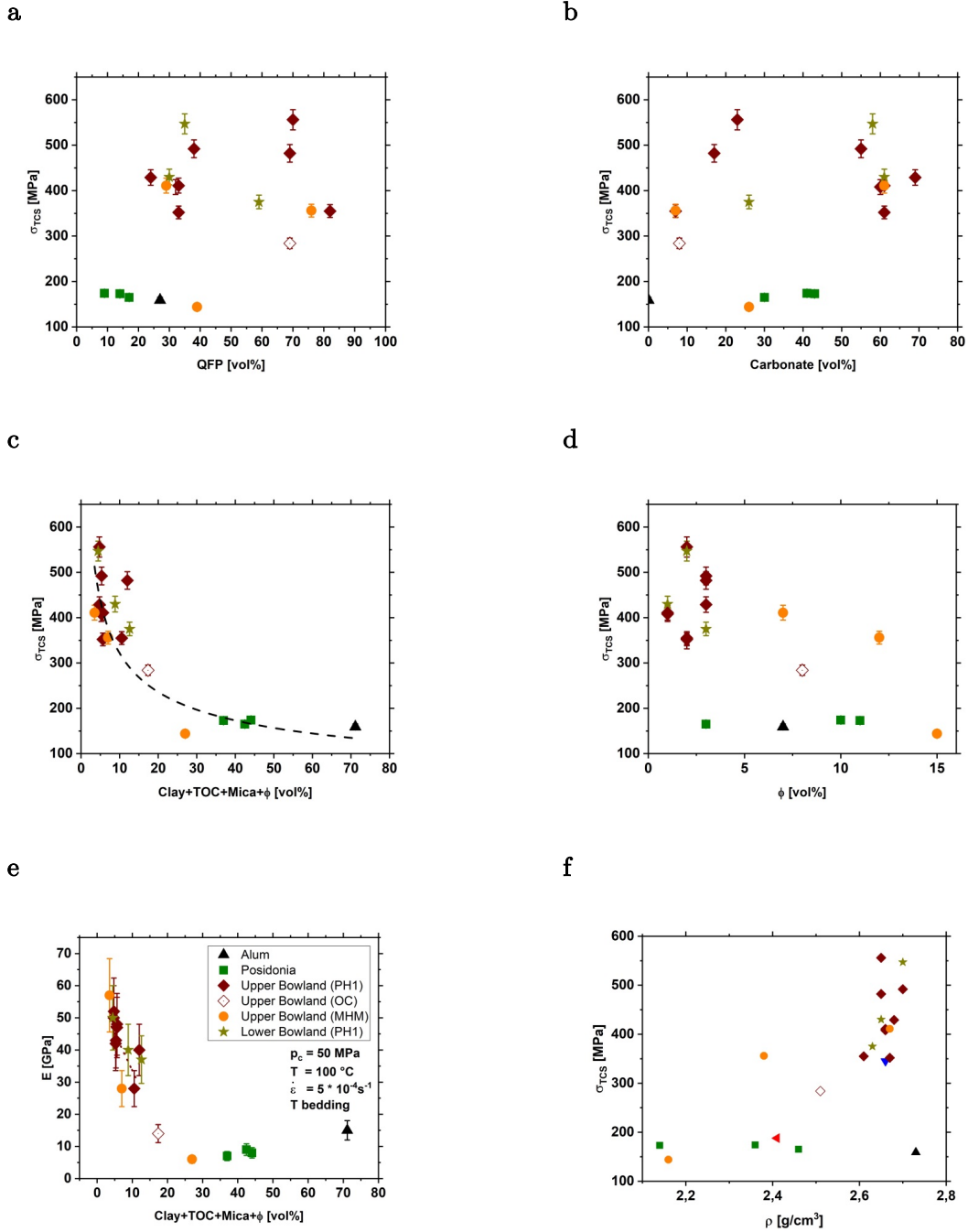
Figure 10 Influence of volumetric fraction of QFP = quartz + feldspar + pyrite (**a**), carbonate (**b**), clay + TOC + mica (**c**), porosity (**d**) and density (**e**) on triaxial compressive strength, σ_{TCS}, and static Young's modulus, E, (**f**) of investigates shales. Data were obtained at elevated confining pressure and temperature given in (**e**). The correlation indicated in (**c**) by the dashed line can be approximated by the following equation: $\sigma_{TCS}[MPa] = 899[MPa] * (Clay + TOC + Mica + \phi)^{-0,45}$ ($r^2 = 0,88$). OC = outcrop, PH1 = Preese Hall 1, MHM = Marl Hill Moor

35

In this study, the triaxial compressive strength was reduced with fraction of weak phases increasing up to about 30 %, above which σ_{TCS} is almost constant (**Fig. 10c**). A threshold of about 30 vol% fraction of (corresponding to $\approx$ 25 wt%) weak phases possibly separates triaxial compressive strength of samples with load-bearing framework of hard minerals from triaxial compressive strength of aggregates with interconnected layers of weak minerals. A similar threshold value between stronger and softer materials of $\approx$ 30 wt% clays was suggested by Bourg (2015) for deformation of various shales. Similarly, Crawford et al. (2008) observed a threshold of $20-30$ wt% clay for synthetic quartz-clay mixtures experimentally sheared at various confining pressures. They also noted a transition from a strong quartz grain-framework to weak clay-matrix support if the clay fraction exceeds porosity and the quartz framework is replaced by a high clay particle fraction. Neglecting the clay- and TOC-rich Posidonia and Alum shale, there is also a clear reduction of σ_{TCS} with increasing porosity (**Fig. 10d**), in agreement with Rybacki et al. (2015). The Young's modulus E shows no clear correlation with the fraction of QFP and carbonate Cb (**Tab. 3**), but decreases with increasing weak mineral fraction and porosity (**Fig. 10e**) (**Tab. 3**). Sone and Zoback (2013a) found a similar empirical relation of decreasing Young's moduli with increasing amounts of weak minerals for Barnett, Haynesville and Eagle Ford shales. In agreement with this study, Rybacki et al. (2015) found that static Young's modulus is anti-correlated with porosity for several Posidonia shales. In contrast, these authors found no correlation between E and weak mineral phases but with the amount of QFP, again related to different test conditions and sample material. Triaxial compressive strength and static Young's modulus correlate with sample bulk density, which is mainly affected by TOC and porosity due to their relatively low density compared to the remaining sample constituents (Eseme et al. 2007) (**Fig. 10f**). Below a source rock density of $\rho \approx$ 2.5 $\frac{g}{cm^3}$, triaxial compressive strength is almost independent of bulk density (**Fig. 10**f). Since the density of source rocks can easily be determined in situ by wire line gamma logs, a trend as shown in **Fig. 10f** may be used to estimate σ_{TCS} directly.

The effect of composition on the maximum axial strain before failure is more complex and often visible only for sample subsets of different shale formations. As would be intuitively expected, samples with a high fraction of strong minerals are more brittle and the maximum axial strain

before failure is reduced (**Fig. 9c**). This was found for Upper Bowland (PH1) and Posidonia shales. However, for strongly varying composition within a single formation, the trend is obscured (**Tab 3**). If variation in mineralogy is small, bulk composition is important for the mechanical behavior of the shales (Rybacki et al., 2015). At elevated confining pressures and temperatures, the maximum axial strain before failure of Upper Bowland shales increased slightly with increasing Cb content (**Fig. 9d**), whereas ε_{max} decreased at increasing QFP fractions (**Fig. 9c**). This contrasting behavior provides a good example for a possible change of dominant deformation behavior at elevated confining pressure and temperature compared to ambient conditions. In general, ε_{max} increased with higher amount of clay + kerogen, but if restricted to individual formations with relatively small variation of weak phases (e.g., Bowland PH1 or Posidonia), we found no correlation. This also holds for the effect of porosity on maximum axial strain before failure measured at ambient and elevated deformation conditions (**Tabs. 2, 3**).

The influence of shale composition on σ_{TCS} and E is summarized in **Fig. 1b and c.** The ternary diagrams show the volumetric fraction of mechanically weak (Cly + TOC + Mca + Poro), intermediate strong (Cb) and strong (QFP) phases of the shales. The triaxial compressive strength (superimposed values in **Fig. 1b**) and static Young's modulus (superimposed values in **Fig. 1c**) do not dependent as much on carbonate and QFP content, but clearly decrease for high amounts of weak phases (**Fig. 1b, c**). Upper Bowland outcrop samples are distinctively weaker than core samples (**Fig. 1b**, **Fig. 4a**), due to a higher fraction of weak phases (**cf. Tab. 1, Fig. 1**). This confirms that samples retrieved from surface outcrops will not fully represent in situ mechanical properties of shales, as weathering processes may affect mechanical properties. For example, comparing Bowland shale outcrop material with core derived samples (PH1), shows increased porosity for the outcrop samples. Posidonia shales, containing mainly soft mineral components, are distinctively weaker than outcrop- and core-derived Bowland shales. The static Young's modulus shows the same behavior with respect to sample mineralogy (**Fig. 1c**). In summary, any change in fractions of strong (e.g. quartz) or intermediate strong (carbonates) mineral phases did hardly affect the uni– and triaxial compressive strengths and static Young's moduli of the investigated shales but affected the maximum axial strain before failure of deformed samples. Most

strikingly, the uni– and triaxial compressive strengths and Young's moduli anticorrelate with the fraction of weak components (e.g. clays) (**Figs. 10c, f**).

6.1.1 Comparing sample triaxial compressive strength and Young's modulus to predictions from effective medium theories

Effective medium theories allow characterizing mechanical properties of rocks with respect to mineral composition, as for example Young's modulus (Mavko et al. 2009). Typically, the approach relies on volumetric fractions of sample constituents and cannot capture chemical, cementation or structural effects (Rybacki et al. 2015). In applying this approach, we simplified the mineral composition of investigated shales defining two endmembers: relatively weak (TOC, Cly, ϕ) and relatively strong (Qtz, Cb, Mca, Fsp, Py) mineral constituents (Sone and Zoback 2013a).

Ji (2004) suggested a phenomenological approach to predict the mechanical properties (Young's modulus, triaxial compressive strength) of multiphase materials in terms of volume fractions and component properties. We applied his generalized mixture rule (GMR) to interpret our data. The GMR is defined as:

$$M_c(J) = \left[\sum_{i=1}^{N} \left(f_i * M_i^J \right) \right]^{\frac{1}{J}} \tag{1}$$

where $M =$ is a specific mechanical property (in our case σ_{TCS}, E), f is the volumetric fraction of the component, subscripts i and c represent the i*th* phase of a composite (c) consisting of N phases, and J is a scaling parameter ranging between -1 and +1. Here, the arithmetic (J = +1) and harmonic (J = -1) average represent an upper (Voigt) or lower bound (Reuss), respectively. The Voigt-Reuss-Hill average is described as the mean value of Voigt and Reuss bound.

For the upper triaxial compressive strength-endmember, we used literature data of Novaculite giving $\sigma_{TCS-Nov} = 699$ MPa at the same p_c, T - conditions as applied here (Rybacki et

al. 2015). The lower triaxial compressive strength-limit is represented here by σ_{TCS} of Boom clay extrapolated to 50 MPa confining pressure (Bouazza et al., 1996), where $\sigma_{TCS\text{-}Cly} = 35.5$ MPa.

For the endmember elastic properties, we calculated the weighted average of weak and strong sample constituents, assuming the following elastic moduli and weighting factors, w, (determined from mean composition): $E_{TOC} = 6.3$ GPa, $E_{Clay} = 3.2$ GPa, $E_\phi = 0$ GPa, $w_{TOC} = 0.29$, $w_{Clay} = 0.42$, $w_\phi = 0.29$ for the weak components and $E_{Mica} = 99.6$ GPa, $E_{Cb} = 82.9$ GPa, $E_{Qtz} = 93.2$ GPa, $E_{Py} = 309.5$ GPa, $E_{Fsp} = 40.5$ GPa, $w_{Mica} = 0.06$, $w_{Cb} = 0.43$, $w_{Qtz} = 0.49$, $w_{Py} = 0.01$ and $w_{Fsp} = 0.01$ for the strong components (Mavko et al., 2009), resulting in $E_{weak} = 3$ GPa and $E_{strong} = 91$ GPa, where the subscripts weak and strong represent the endmember values for the lower and upper bound, respectively. To characterize the elastic properties (E) of investigated shales, we also calculated the Hashin-Shtrikman bounds (Mavko et al. 2009):

$$E_{HS\pm} = \frac{9*K_{HS\pm}*\mu_{HS\pm}}{3*K_{HS\pm}+\mu_{HS\pm}} \tag{2}$$

with:

$$K_{HS\pm} = K_1 + \frac{f_2}{(K_2-K_1)^{-1}+f_1*\left(K_1+\frac{4}{3}*\mu_1\right)^{-1}} \tag{3}$$

$$\mu_{HS\pm} = \mu_1 + \frac{f_2}{(\mu_2-\mu_1)^{-1}+\frac{2*f_1*(K_1+2*\mu_1)}{5*\mu_1*\left(K_1+\frac{4}{3}*\mu_1\right)}} \tag{4}$$

where subscript *HS* is Hashin-Shtrikman, $\pm$ is either upper (+) or lower (-) bound, *K* is bulk modulus and μ is shear modulus of simplified sample constituents. Upper bound is given when strong material is K_1, μ_1 and lower bound when weak material is K_1, μ_1. Here, we assume $K_{weak} = 1.5$ GPa, $K_{strong} = 37$ GPa, $\mu_{weak} = 1.4$ GPa, $\mu_{strong} = 44$ GPa, where strong endmember phase is represented by quartz and weak endmember by clay (Mavko et al. 2009). Finally, we used an approach predicting the elastic constants of multiphase materials as introduced by Paul (1960):

$$E_{Paul} = \frac{E_{weak}*\left(E_{weak}+(E_{strong}-E_{weak})*f_{strong}^{\frac{2}{3}}\right)}{E_{weak}+(E_{strong}-E_{weak})*f_{strong}^{\frac{2}{3}}*\left(1-f_{strong}^{\frac{2}{3}}\right)} \tag{5}$$

In general, the triaxial compressive strengths of all investigated shales are within the bounds, mostly plotting closer to the Reuss bound (**Fig. 11**). σ_{TCS} of almost all Bowland shales follow the lower (Reuss) bound, whereas Alum shales plot close to the upper (Voigt) bound. (**Fig. 11a**). σ_{TCS} of Posidonia shales plot between the Voigt-Reuss-Hill and lower (Reuss) bound.
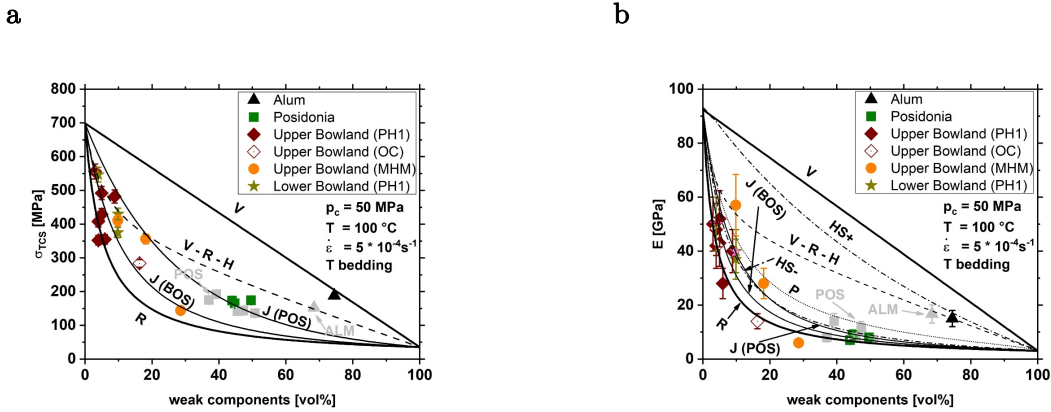
Figure 11 Triaxial compressive strength, σ_{TCS}, (**a**) and static Young's modulus, E, (**b**) obtained at elevated confining pressures and temperatures plotted against volumetric fractions of weak components. Experimental data is compared to different effective medium theories. Grey symbols display mechanical data of black shales measured by Rybacki et al. (2015) at similar deformation conditions. Voigt (V) and Reuss (R) indicate upper and lower bounds, respectively. Voigt-Reuss-Hill (V-R-H) is average value of Voigt and Reuss bounds. Ji (J) represents best fit bound proposed by Ji (2004) for Posidonia (J (POS)) and Bowland shales (J (BOS)). Paul (P) displays approach introduced by Paul (1960) and Hashin-Shtrikman (HS) upper (+) and lower (-) bounds as described by e.g. Mavko et al. (2009). Deformation conditions are indicated. ALM = Alum, POS = Posidonia, PH1 = Preese Hall 1, OC = Outcrop, MHM = Marl Hill Moor

The best fit value of the GMR scaling parameter J for σ_{TCS} of all Posidonia shales including literature data yields $J_{Posidonia}$ = -0.13 (**Fig. 11a**). (Ji 2004) suggested a value of J $\approx$ - 0.25 for rock samples with a weak-phase supported structure (f_{strong} < 0.5), which is close to our value. A value

of J $\approx$ + 0.25, as supposed by Ji (2004) for aggregates with a strong-phase supported structure (f_{strong} > 0.7), would not fit our data ($J_{Bowland}$ = -0.38). An average value of J = 0.23 was determined by Rybacki et al. (2015) for black shales (f_{strong} < 0.3) measured at ambient and elevated p_c, T - conditions. J = 0.23 is far above the value that we calculated and that also is suggested by Ji (2004), presumably due to differences in fabric and humidity between shales investigated in previous studies and our samples.

The static Young's moduli plot between the Reuss-bound and the upper Hashin-Shtrikman scheme (HS+) (**Fig. 11b**). Alum shales fit very well to the Voigt-Reuss-Hill average and Bowland shales plot in general close to the lower (Reuss) bound. The static Young's modulus of Posidonia shales ranges between the average for elastic properties of multiphase materials (Paul 1960) and the lower (Reuss) bound. The elastic properties of Posidonia shales also fit to the lower Hashin-Shtrikman bound (HS-) (**Fig. 11b**). This suggests that Bowland shales may have a stronger degree of anisotropy compared to Posidonia shales although mechanical testing using bedding-parallel samples is necessary to confirm. Fitting the Posidonia and Bowland dataset to the GMR approach yielded best fit values for the scaling parameter $J_{Posidonia}$ of -0.62 and $J_{Bowland}$ = -0.82, respectively, which are close to the lower (Reuss) bound (J = -1).

Shales are often known to be very anisotropic and thus a separate trend closer to the Voigt average is expected if measured parallel to bedding.

6.1.2 Brittleness of shale rocks

Common practice (used in the Exploration & Production industry) in estimating the potential of a successful hydraulic borehole stimulation is to determine the brittleness, B, of the reservoir rock (Holt et al. 2011). The brittleness of a rock is an empirical rock parameter often normalized to range between 0 (ductile) and 1 (brittle). Typically, ductile rocks are expected to show fast fracture closure, whereas brittle rocks are believed to be easily fractured. Various empirical brittleness indices exist (e.g. Rybacki et al. 2016). Here, we first calculated the brittleness of the shales based on their mineral composition (Rybacki et al. 2016):

$$B_{min} = \frac{w_{QFP}*f_{QFP}}{w_{QFP}*f_{QFP}+w_{Cb}*f_{Cb}+w_{ClyTOCMca}*f_{ClyToc}+w_{\phi}*\phi} \tag{6}$$

where B_{min} = brittleness determined from mineralogy, w_{QFP}, w_{Cb}, w_{ClyTOC} and w_{ϕ} are weighting factors ranging from 0 to 1 and f_{xx} is the fraction of mineral xx given in vol%. We set w_{QFP} = w_{ClyTOC} = w_{ϕ} = 1 and w_{Cb} = 0.5 as suggested by Rybacki et al. (2016) for shale rocks.

Secondly, we calculated the brittleness index based on the Young's modulus. Rybacki et al. 82016) suggested the following empirical relation between brittleness and E:

$$B_E = (0.07 \pm 0.01) * \left(\frac{E}{E_0}\right)^{0.53 \pm 0.07} \tag{7}$$

where B_E = brittleness determined from E based on a comparison of E with stress-strain behavior at low p_c, T - conditions and E_0 is a normalization factor with $[E_0]$ = 1GPa. The resulting B_{min} and B_E values are shown in **Figs. 12 a, b**., including Posidonia shales observed by Rybacki et al. (2016). Bowland shales generally give substantial higher brittleness values compared to Posidonia and Alum shales (**Figs. 12a, b**). B_{min} is decreasing with increasing amounts of weak sample constituents, and with increasing fractions of carbonates (**Fig. 12a**). By definition, increasing amounts of strong components result in higher brittleness indices. Also, B_E is decreasing with increasing amounts of weak components but does not significantly dependent on carbonates or strong components (QFP), in line with the trend found for E shown in **Fig. 1b** (**Fig. 12b**). B_E values are lower on average than B_{min} values.
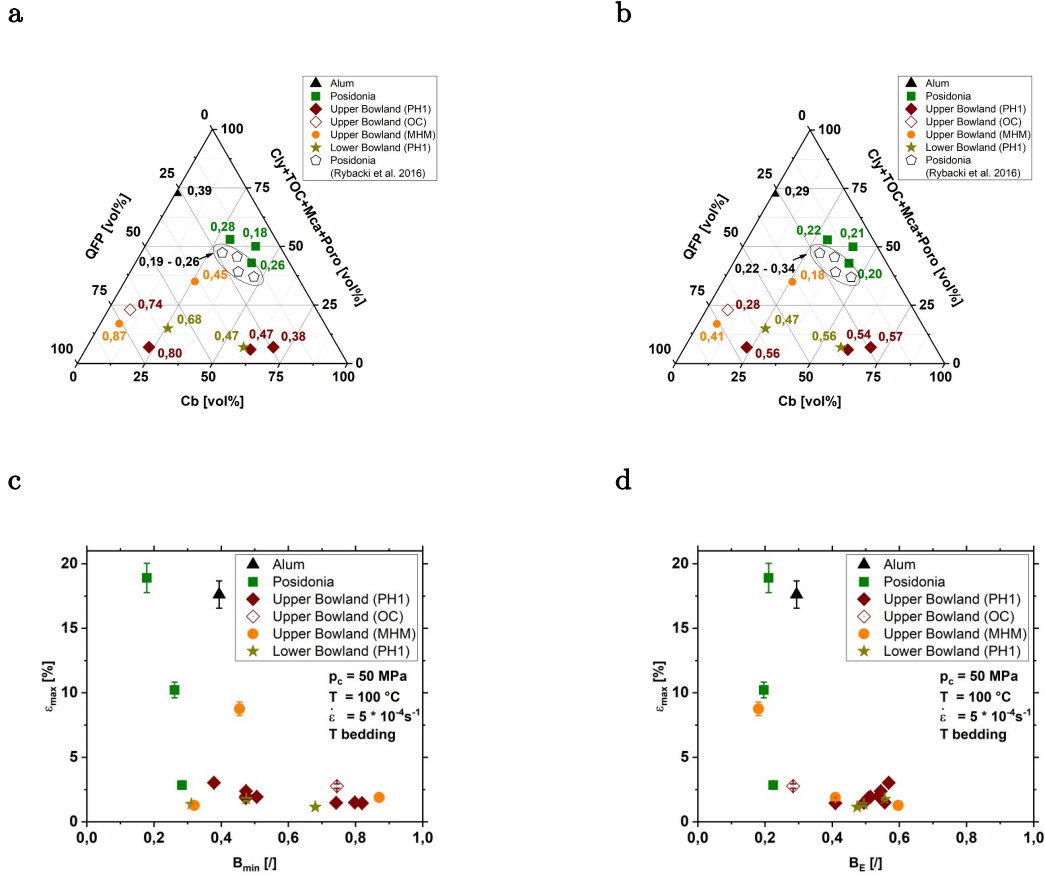
Figure 12 Ternary plots displaying mineral composition of investigated samples. Composition is separated into mechanically strong (Qtz + Fsp + Py), intermediate strong (Cb) and weak (Cly + TOC + Mca) fractions. Qtz = quartz, Fsp = feldspar, Py = pyrite, Cb = carbonate, Cly = clay, TOC = total organic carbon, Mca = mica. Mineral data are given in vol%, normalized to 100 vol% taking also the sample porosity into account. Superimposed values indicate Brittleness determined from composition B_{min} (**a**) and static Young's modulus B_E (**b**) (Rybacki, Meier, and Dresen 2016). Maximum axial strain ε_{max} (in %) before failure vs. brittleness determined from composition B_{min} (**c**) and static Young's modulus B_E (**d**). OC = outcrop, PH1 Preese Hall 1, MHM = Marl Hill Moor. PH1 = Preese Hall 1, OC = outcrop, MHM = Marl Hill Moor

Samples displaying increasing brittleness values also show decreasing maximum axial strain ε_{max} before failure, when deformed at elevated confining pressures and temperatures (**Figs. 12c, d**). A brittleness-threshold at about $B_E \approx 0.4 \pm 0.1$ separates sample deformation in dominantly ductile ($B_E < 0.4 \pm 0.1$) or dominantly brittle regimes ($B_E > 0.4 \pm 0.1$) as shown by the stress-strain plots (**Fig. 4a**).

6.2 Effect of confining pressure

Several empirical failure criteria exist to describe the confining pressure-dependent triaxial compressive strength of a rock. These are, for example, Mohr-Coulomb, Drucker-Prager, Hoek-Brown, Griffith, Murrell or Fairhurst criteria (Sheorey 1997). To characterize the influence of confining pressure on the triaxial compressive strength of Posidonia and Bowland shales we used the linear Mohr-Coulomb failure criterion given by

$$\tau = S_0 + \sigma_n \mu_i \ \text{ or } \quad \sigma_1 = \sigma_{UCS} + np_c \tag{8}$$

with τ = shear stress, S_0 = cohesion, σ_n normal stress, μ_i = coefficient of internal friction, p_c = confining pressure, $\sigma_1 = \sigma_{TCS} + p_c$ and n = constant. The coefficient of internal friction may be determined from the best fit slope n in a σ_1-p_c diagram (**Fig. 13**) with μ_i = (n-1)/(2$\sqrt{n}$), (Zoback 2007). **Fig. 13** shows the data measured at elevated p_c, T - conditions on Posidonia (HAR) and Bowland (outcrop) shales (c.f., **Tab. 4, Fig. 5b**) yielding μ_i values of 0.42 ± 0.03. This friction coefficient is significantly lower than predicted from the measured angle between the fracture surface and the σ_1 loading direction. This may to some extent be related to boundary effects such as end cap friction. Extrapolation to ambient confining pressure results in higher values of σ_{UCS} than were determined in uniaxial compression tests. Note that measured σ_{UCS} define an upper limit since they were determined at ambient temperature whereas triaxial experiments were performed at T = 100 °C. It is conceivable that enhanced sample compaction at increasing confining pressure may result in a substantial strength increase that is not captured by a linear fit (Rybacki et al. 2017). The estimated coefficients of internal friction μ_i of shale rocks from this study are similar to published data on Wilcox shale ($\mu_i \approx$ 0.3 – 0.5) (Ibanez and Kronenberg 1993), Opalinus clay ($\mu_I \approx$ 0.25) (Jordan and Nüesch 1989), Posidonia shales ($\mu_i \approx$ 0.16 – 0.32), Alum shales (μ_i = 0.36 – 0.55) (Rybacki et al. 2015) and Eagle Ford and Haynesville shales (μ_i = 0.3 – 0.5) (Sone and Zoback 2013b) (**Fig. 13**). Interestingly, published data on Barnett shale reveal relatively high values of $\mu_i \approx$ 0.7 – 1.1 (Sone and Zoback 2013b; Rybacki et al. 2015). (Sone and Zoback 2013b)

also found a slight decrease of μ_i for increased amounts of weak components (clay + TOC). Including data from Rybacki et al. (2015) on shales obtained at similar experimental conditions, we found no clear correlation between μ_i and porosity or the amount of weak material (**Tab. 5**).
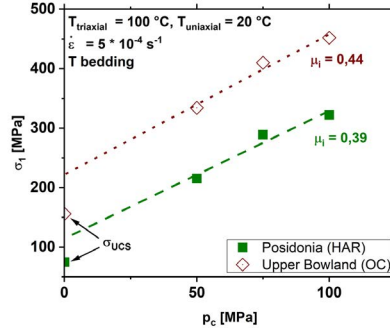
Figure 13 Influence of confining pressure p_c on $\sigma_1 = \sigma_{TCS} + p_c$. Estimated values of internal coefficient of friction μ_i are indicated. σ_{UCS} = measured uniaxial compressive strength. HAR = Harderode, OC = outcrop

Table 5 Coefficient of internal friction from this study and Rybacki et al. (2015)

sample	QFP [vol%]	Cb [vol%]	Cly + TOC [vol%]	Porosity [%]	μ_i	Reference
Bowland (BOS_OC)	75	9	16	8	0.44	this study
Posidonia (HAR)	18	31	51	3	0.39	this study
Posidonia (DOT)	16	47	37	11	0.18	(Rybacki et al. 2015)
Alum (ALM1)	31	1	68	1	0.36	(Rybacki et al. 2015)

QFP = Qtz + Fsp + Py, Cb = carbonates, Cly + TOC = Clay + TOC, μ_I = coefficient of internal friction. For sample abbreviations see caption of table 1.

6.3 Strain rate and temperature effects

A change in strain rate by two orders of magnitude has no significant effect on triaxial compressive strength of Posidonia and Bowland shales at p_c of 50 MPa and T of 75 – 125 °C (**Fig. 14**). Lajtai et al. (1991) report similar observations for other rocks, such as limestone (brittle) and salt (ductile). A common approach to express the strain rate sensitivity of rocks deforming by dislocation glide is an exponential law of the form:

$$\dot{\varepsilon} \propto e^{\alpha * \sigma_{TCS}} \tag{9}$$

which was applied by e.g., Chong et al. (1980) and Kwon and Kronenberg (1994a) for shales from different formations or localities. α is an empirical constant, which is negative for the whole data set of investigated Posidonia and Bowland shales (α_{POS} = -0.46, α_{BOS} = -4.61), determined from regression lines in semi-logarithmic space (**Fig. 14a**). Restricting the fit to the two measurements obtained at low strain rate ($\dot{\varepsilon}$ = 5 * 10^{-6} and 5 * 10^{-5} s^{-1}) yields α-values for Posidonia and Bowland shales of ≈ 0.16 and ≈ 0.57, respectively. This is similar to values reported by Ibanez and Kronenberg (1993) (α ≈ 0.36), Kwon and Kronenberg (1994a) (α ≈ 0.27) and Rybacki et al. (2015) (α ≈ 0.33) for other shales.

a   b
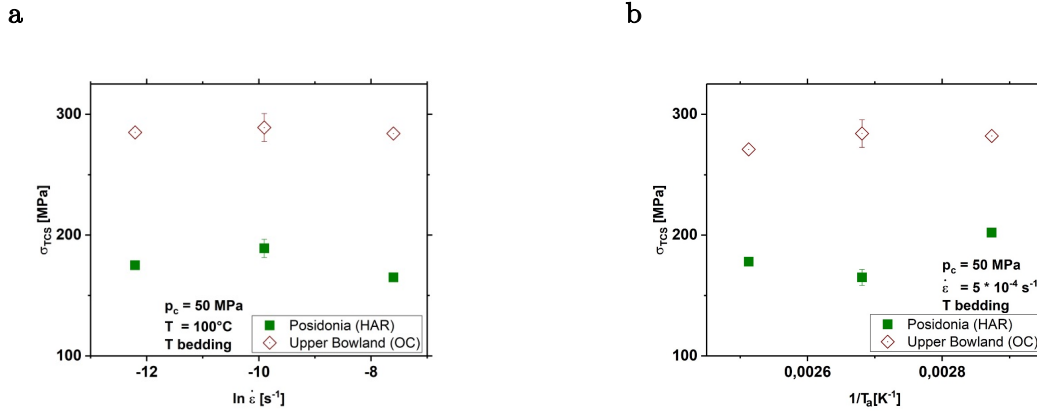
Figure 14 Effect of strain rate, $\dot{\varepsilon}$, on triaxial compressive strength, σ_{TCS}, (**a**) and variation of σ_{TCS} with inverse absolute temperature, T_a, (**b**). HAR = Harderode, OC = outcrop

With increasing temperature, the triaxial compressive strength of investigated shales decreased slightly (**Fig. 6b**), as also described by Ibanez and Kronenberg (1993) and Masri et al. (2014) for Wilcox and Tounemire shale, respectively. Assuming that dislocation glide in clay minerals is mainly responsible for strain rate and temperature sensitivity, we use the following constitutive relation (Ibanez and Kronenberg 1993):

$$\dot{\varepsilon} = A * e^{\alpha * \sigma_{TCS}} * e^{-\left(\frac{Q}{R*T_a}\right)}$$

(10)

where A is a material constant, Q is the activation energy, R is the gas constant and T_a is absolute temperature. Note that **Eq. (10)** may be used only as first order approximation, since the flow law is valid only at steady state creep conditions (Rybacki et al. 2015). Using $\alpha_{POS} = 0.16$ and $\alpha_{BOS} = 0.57$ and fitting **Eq. (10)** to the corresponding Arrhenius plot (**Fig. 14b**) yields apparent activations energies of $Q_{POS} \approx 98 \frac{kJ}{mol}$ and $Q_{BOS} \approx 140 \frac{kJ}{mol}$. Ibanez and Kronenberg (1993) and Rybacki et al. (2015) measured comparable activation energies of Wilcox shale ($Q = 87 \pm 40 \frac{kJ}{mol}$) and Posidonia shale ($Q = 167 \frac{kJ}{mol}$), respectively, deformed perpendicular to bedding.

7 Conclusions

Deformation experiments performed on black shales originating from different formations and with varying mineralogy and maturity reveal dominantly brittle to semibrittle deformation behavior at the imposed p_c, T - conditions. For Upper Bowland shale, samples retrieved from surface outcrops are somewhat weaker and less brittle than samples prepared from core material. The triaxial compressive strength and static Young's moduli are strongly influenced by sample mineralogy and confining pressure conditions, whereas the effects of sample porosity, temperature and strain rate are minor.

σ_{TCS} and E of investigated shales clearly decrease with increasing amounts of weak components (Clay+TOC+Mica). However, the effect is small above a threshold of $\approx 25 - 30$ vol% weak mineral constituents in the samples. In general, this trend follows predictions of effective medium approaches, with experimental data mostly plotting close to the lower bound. Brittleness, in particular if calculated from Young's modulus, shows the same general trend of an existing threshold at $B_E \approx 0.4$.

The obtained results lead us to suggest a substantially lower fracture closure rate of brittle Bowland shales compared to semibrittle Posidonia shales. However, the relatively low hydrocarbon content and low porosity of inspected Upper Bowland core samples, in conjunction with their low maturity, may also limit the prospectivity of these shales compared to Posidonia shale. Considering instead the overmature Lower Bowland shale as target formation for gas extraction may be more successful, since it ranges within the gas window contrasting to the peak oil-mature Upper Bowland shale. In a companion paper we will compare short-term mechanical properties of Posidonia and Bowland shales as described here with long-term creep behavior of shales.

Acknowledgements

Chapter 3: Creep of Posidonia shale at elevated pressure and temperature

1 Summary

The economic production of gas and oil from shales requires repeated hydraulic fracturing operations to stimulate these tight reservoir rocks. Besides simple depletion, the often observed decay of production rate with time may arise from creep-induced fracture closure. We examined experimentally the creep behavior of an immature carbonate-rich Posidonia shale, subjected to constant stress conditions at temperatures between 50 and 200 °C and confining pressures of 50 to 200 MPa, simulating elevated in situ depth conditions. Samples showed transient creep in the semibrittle regime with high deformation rates at high differential stress, high temperature, and low confinement. Strain was mainly accommodated by deformation of the weak organic matter and phyllosilicates and by pore space reduction. The primary decelerating creep phase observed at relatively low stress can be described by an empirical power law relation between strain and time, where the fitted parameters vary with temperature, pressure and stress. Our results suggest that healing of hydraulic fractures at low stresses by creep-induced proppant embedment is unlikely within a creep period of several years. At higher differential stress, as may be expected in situ at contact areas due to stress concentrations, the shale showed secondary creep, followed by tertiary creep until failure. In this regime, microcrack propagation and coalescence may be assisted by stress corrosion. Secondary creep rates were also described by a power law, predicting faster fracture closure rates than for primary creep, likely contributing to production rate decline. Comparison of our data with published primary creep data on other shales suggest that the long-term creep behavior of shales can be correlated to their brittleness estimated from composition. Low creep strain is supported by a high fraction of strong minerals that can build up a load-bearing framework.

<u>List of symbols</u>

A, B, $c_{1,2}$, m, t_0, s, k	Creep constants
B_r	Brittleness
d	Indenter diameter
F	Volume fraction
h, $\dot{h}$,	Indentation depth, rate
n	Stress exponent
P	Confining pressure
Q	Activation energy
T	Temperature
t	Time
V	Activation volume
ε, $\dot{\varepsilon}$	Axial strain, strain rate
ϕ	Porosity
σ	Differential stress
σ_{net}	Indenter stress

2 Introduction

Over the past 20 years, exploitation of (unconventional) gas from tight shale reservoirs increased strongly and is expected to contribute considerably to future energy supply in the next decades, although estimates of the recoverable amounts of gas are quite variable (Howarth et al. 2011; McGlade et al. 2013). The uncertainty of future production assessment is linked to the difference between the estimated amount of gas in place and the fraction of technically recoverable shale gas resources. Beside socio-environmental issues, fast production decline rates of unconventional gas reservoirs render reliable forecasting very difficult (Hughes 2013; Wang 2016). Empirically fitted production curves show a hyperbolic or exponential decline in the first few (four to five) years after stimulation by hydraulic fracturing (Baihly et al. 2010; Wang 2016). The causes of such a

fast decline are a matter of debate and may be related to transient flow of free and adsorbed gas to natural and artificially-induced fractures until (pressure dependent) depletion in conjunction with time-dependent fracture closure (Patzek et al. 2014; Wang 2016).

A reduction of fracture conductivity with time depends on several factors, including the in situ closure stress (normally in the range of several tens of MPa acting perpendicular to the fracture surface), fluid chemistry (e.g., brine concentration), fines migration and proppant properties (type, diagenesis, crushing, size and distribution). Experimental and modelling results usually show enhanced fracture closure rates at high closure stress and temperature, low Young's modulus and high amount of soft minerals, low fraction of proppants with small size, low fracture roughness and minor shear displacement (minor self-propping). The presence of water also accelerates the rate of fracture permeability reduction, in particular for clay-rich shales (Akrad et al. 2011; Alramahi and Sundberg 2012; Guo and Liu 2012; Kassis and Sondergeld 2010; LaFollette and Carman 2010; Liu and Sharma 2005; Morales et al. 2011; Pedlow and Sharma 2014; Reinicke et al. 2010; Stegent et al. 2010; Volk et al. 1981; Zhang et al. 2013; Zhang et al. 2015; Zhang et al. 2016b). The brittleness of shales, which correlates to some extent with their composition and elastic properties (Rybacki et al. 2016; Zhang et al. 2016a), may be also relevant for the long-term fracture healing rate. Fast healing is expected for more ductile shales by rapid proppant embedment or enhanced creep of contact areas in unpropped fractures. In addition, brittleness may control the amount of natural open or sealed fractures, which are generated mainly during subsidence by the pressure increase due to creation of gas or oil from kerogen (Norris et al. 2016).

Quantitative estimates of fracture healing rates require knowledge of the geomechanical behavior of shales. Under reservoir conditions (P < 100 MPa, T < 200 °C), shales often show brittle to semibrittle deformation, where the combination of mechanisms (brittle microfracturing, pore collapse, granular flow and crystal-plastic defect activity) yields a mechanical behavior and strength depending on rock composition and in situ effective pressure, temperature and strain rate conditions (Ibanez and Kronenberg 1993; Rybacki et al. 2015). However, only a few studies of the long-term creep deformation of shales exist so far. Few data exist dealing with the creep behavior of Opalinus clay (Naumann et al. 2007), Boom clay (Yu et al. 2015), Callovia-Oxfordian Bure

Clay (Gasc-Barbier et al. 2004), and other argillaceous rocks (Zhang and Rothfuchs 2004; Fabre and Pellet 2006). Creep experiments on shales focus on compaction and consolidation (Cogan 1976; de Waal and Smits 1988; Dudley et al. 1998), the effect of adsorption and swelling on creep (Heller and Zoback 2011; Hol and Zoback 2013) and on viscoelastic or viscoplastic creep of shales in response to nanoindentation (Mighani et al. 2015) and applied differential stresses at elevated confining pressures (Almasoodi et al. 2014; Chang and Zoback 2009, 2010; Chong et al. 1978; Li and Ghassemi 2012; Rassouli and Zoback 2015; Sone and Zoback 2010, 2011, 2013, 2014; Yang and Zoback 2016). The latter experiments indicate that creep is enhanced at high differential stress, high clay content, in the presence of water and if loaded normal to bedding orientation. For the examined North American shales, the influence of confining pressure appears to be either absent or reducing creep rates only slightly up to a few tens MPa confinement.

Here, we report on deformation experiments on immature Posidonia (oil) shale at high confining pressures (P) and temperatures (T) in order to evaluate the creep properties of this relatively weak shale as a function of stress and applied P, T - conditions. The results are used to estimate the proppant embedment potential and fracture closure from measured long-term creep behavior.

3 Sample Material and Experimental Methods

Cylindrical samples of 20 mm length x 10 mm diameter were prepared from black shale blocks collected in a quarry with active mining near the village Dotternhausen (Southern Germany). This immature Posidonia shale (vitrinite reflectance ≈ 0.6 %) of Mesozoic (lower Jurassic) age is very fine-grained (< 10 µm) with a porosity of about 11 %, measured by mercury injection porosimetry (**Fig. 5 a**). The pore throat diameter distribution shows a maximum between 20 and 40 nm. The laminated matrix of this carbonate mudstone consists of ≈ 42 vol% carbonates, 18 vol% clays (illite, illite-smectite mixed layers and minor kaolinite and chlorite), 14 vol% quartz, feldspar and pyrite and 15 vol% organic matter with high bitumen content (Rybacki et al. 2015). All samples were drilled perpendicular to bedding, defined by enrichment in organic matter with subparallel

oriented pyrite flakes and calcareous bands. The as-is water content of samples is $1 - 2$ wt%. They were stored in an oven at 50 °C until testing.

Triaxial creep experiments were performed in a Paterson-type deformation apparatus (Paterson 1970) at constant load, using argon gas as confining pressure medium. Samples were jacketed by 0.5 mm thin copper sleeves to prevent intrusion of the gas, pressurized and heated to the desired level, and deformed in a single run to maximum axial strains between 3 % and 26 %, depending on applied P, T - conditions (**Tab. 1**). Recorded axial displacements were corrected for the system compliance, resulting in calculated axial strains with an uncertainty < 4 %. Measured axial forces were corrected for the strength of copper sleeves, previously determined in calibration runs on copper samples at similar conditions, and converted to axial stress assuming constant volume deformation. Because of the low stiffness of the Paterson apparatus the initial elastic stress is less accurate with an estimated error < 20 %. The reported error of post yield stress is typically < 6 % at $T < 200$ °C and <10 % at T $= 200$ °C, resulting from uncertainty of the copper strength, which depends on P, T - conditions and strain rate, and slightly decreasing sample stress with increasing strain at fixed applied load. The copper strength was in the range of 204 to 380 MPa, accounting for 21±4 % of the measured total force.

Table 1 Experimental conditions

sample	p_c [MPa]	T [°C]	σ [MPa]	t_{max} [s]	ε_{max}	m	A [s^{-m}]	$\dot{\varepsilon}_{min}$ [s^{-1}]	rem
DOT01	50	100	166	4100	0.1			$6.5 \cdot 10^{-6}$	failure
DOT02	50	100	150	168000	0.06	0.0659	0.02553		
DOT03	50	100	157	2400	0.1			$1.1 \cdot 10^{-5}$	failure
DOT04	50	100	148	595000	0.07	0.06474	0.02738		
DOT05	50	50	157	97000	0.09			$2.4 \cdot 10^{-7}$	failure
DOT06	50	150	127	430	0.12			$8.8 \cdot 10^{-5}$	failure
DOT07	50	75	160	500	0.09			$5.8 \cdot 10^{-5}$	failure
DOT08	75	100	164	60	0.18			$2.6 \cdot 10^{-3}$	failure
DOT09	100	100	169	1500	0.20			$4.2 \cdot 10^{-5}$	failure
DOT10	200	100	200	610	0.26			$1.2 \cdot 10^{-4}$	failure
DOT11	75	100	155	70	0.16			$2.0 \cdot 10^{-3}$	failure
DOT12	150	100	205	10700	0.13	0.07479	0.06242		
DOT101	100	100	111	79000	0.04	0.07408	0.01461		
DOT103	100	100	152	4700	0.06	0.08448	0.02383		
DOT104	50	100	154	900	0.06	0.10740	0.02420		
DOT105	150	100	154	22000	0.05	0.04628	0.02349		
DOT107	100	200	113	5100	0.05	0.08024	0.02006		
DOT108	100	200	61	26000	0.03	0.09907	0.00841		
DOT109	50	50	156	25000	0.04	0.05044	0.02188		
DOT110	100	50	110	154000	0.03	0.04583	0.01472		

For examination of microstructures we used a scanning electron microscope (SEM, Zeiss Ultra 55 Plus) on broad ion beam (BIB, Jeol IB-19520CCP) polished sections. High resolution analysis was done using a transmission electron microscope (TEM, Fei Tecnai G2 F20 x-Twin) on focused ion beam (FIB, Fei FIB200TEM) prepared foils.

4 Results

In total, we performed 20 creep tests on samples at confining pressures of 50 – 200 MPa and temperatures between 50 and 200 °C. The applied differential stresses (corrected for jacket strength) were between ≈ 60 and 205 MPa, resulting in transient creep curves. Tests were either

manually stopped after some time or beyond sample failure after passing a secondary and finally accelerating creep phase, depending on conditions. The corresponding total creep time varied between 1 minute and 165 hours ($\approx$ 1 week) and the associated axial strain between $\approx$3 and 26 % (**Tab. 1**). In most tests the conditions were chosen such that 2 of the 3 parameters (confinement, temperature, differential stress) were fixed and the third parameter was changed in order to constrain the influence of the varying parameter on the resulting creep rate.

4.1 Creep Behavior

Some typical creep curves of deformed Dotternhausen shales are shown in **Fig. 1**. At constant pressure and temperature, creep rates increased with increasing differential stress, independent of the specific P, T - conditions (**Fig. 1a − d**). Samples subjected to low differential stress showed primary creep behavior, where the strain increment per unit time step continuously decreases with increasing time (primary or decelerating creep phase). In contrast, samples loaded at high differential stress showed subsequently secondary creep with a linear increase in strain with increasing time (i.e. constant creep rate) and finally tertiary (accelerating) creep until failure. The transition from primary to secondary creep occurred in a narrow stress range, corresponding to about 84 – 90 % of the compressive strength obtained in constant strain rate tests of 5×10^{-4} s^{-1} under similar P, T - conditions (Rybacki et al. 2015). Reproducibility was high at low stress, but decreased at high stress deformation (**Fig. 1a**). An increase of confining pressure at constant temperature and stress yielded a decrease of creep rate, i.e., strengthening (**Fig. 1e**). In contrast, increasing temperature at constant confinement and stress resulted in weakening, i.e., increasing creep rate (**Fig. 1f**). We conclude that the creep behavior of Posidonia shale at elevated P, T - conditions is sensitive to stress, pressure and temperature, as expected for semibrittle deformation.
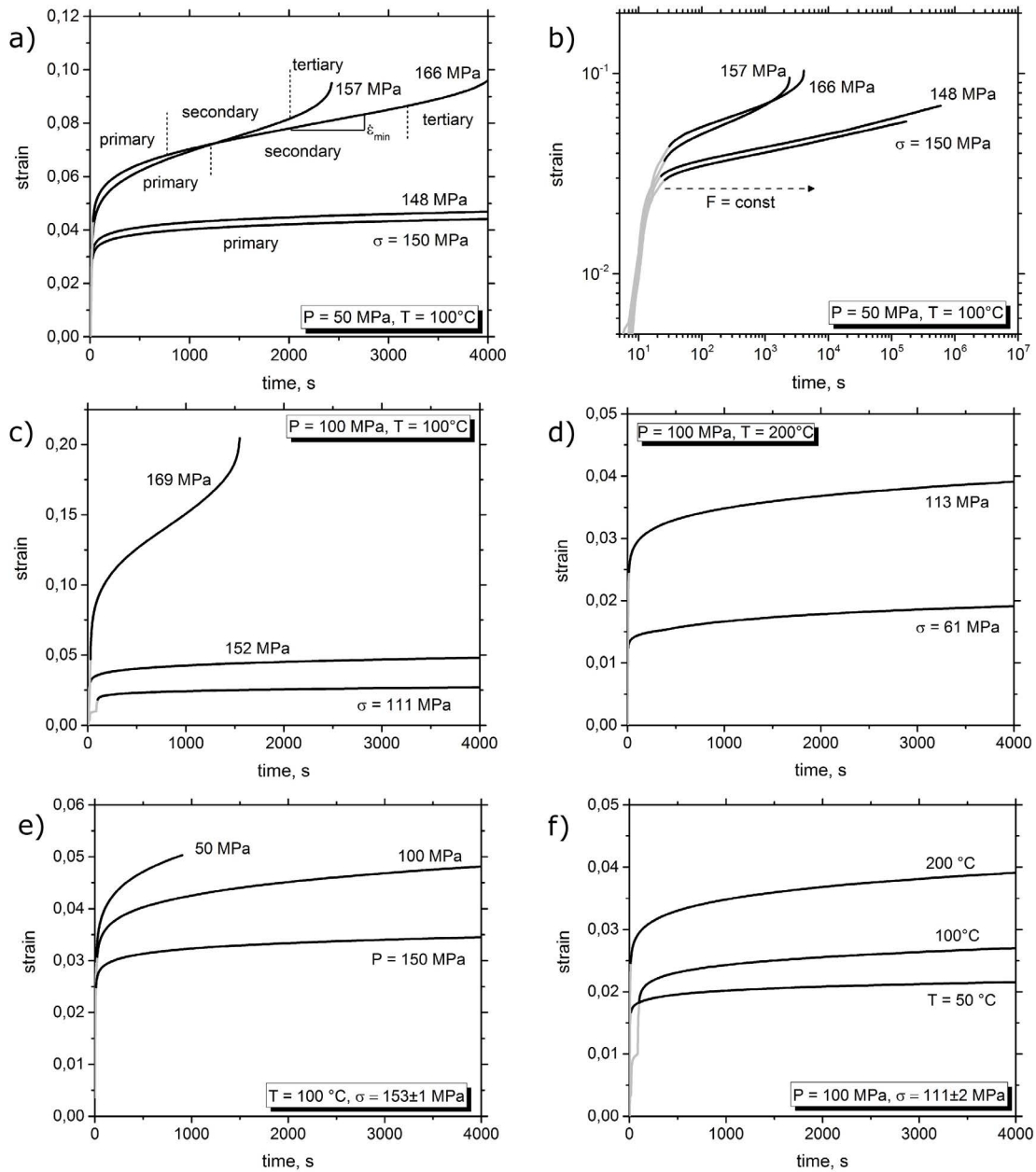
Figure 1 Creep curves of Dotternhausen Posidonia shale in relation to applied differential stress σ (**a** − **d**), confining pressure P (**e**) and temperature T (**f**). At high stress, creep curves show not only primary (decelerating), but also secondary (quasi steady state) and tertiary (accelerating) creep leading to final failure. Increasing pressure reduces the creep rate (**e**), whereas increasing temperature enhances the creep rate (**f**). For comparison, all curves are cut off at 4000 s except in (**b**), where complete curves are shown in log-log scale. During the first few seconds the applied force F was increased up to the desired level that stabilized within 10-20 sec and subsequently held constant until manual test termination or sample failure (**b**).

An example of calculated strain (creep) rates of samples deformed at 50 MPa confinement and 100 °C temperature (DOT01-DOT04, **Tab. 1**), are shown in **Fig. 2**. Here, we show smoothed curves since the numerical derivation of strain rate from strain-time curves yielded noisy results. For comparison, two exemplary unsmoothed curves are shown in light gray in **Fig. 2a**. The two low stress samples deformed in the primary creep regime at 148-150 MPa stress show continuously decreasing strain rates down to about 10^{-8} s^{-1} until test termination, even after about one week deformation (sample DOT 04, deformed at $\sigma = 148$ MPa). The other two samples deformed at higher stress experienced minimum creep rates of about 10^{-5} s^{-1} before failure (**Fig. 2a, Tab. 1**).
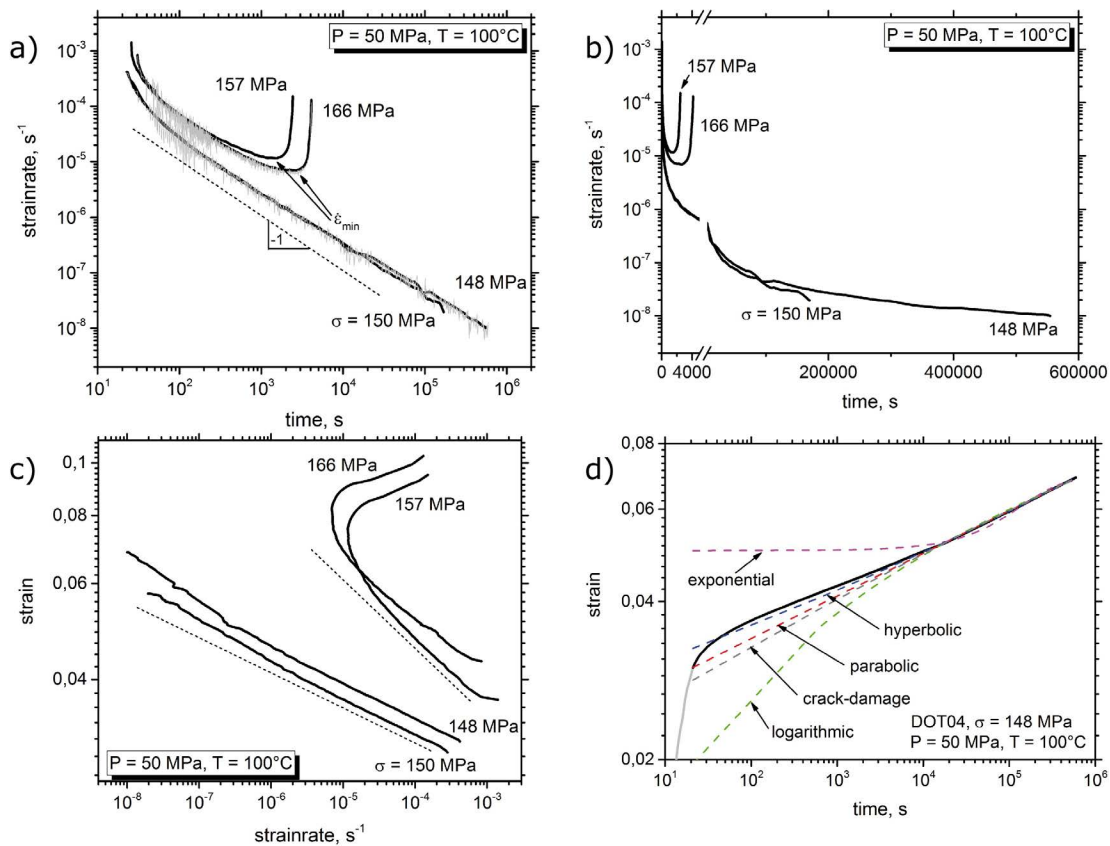
Figure 2 Creep curves of Posidonia shale deformed at 50 MPa pressure and 100 °C temperature, scaled in (**a**) log (strain rate) versus log(time), (**b**) log (strain rate) vs time and (**c**) log (strain) vs log (strain rate). In (**a**) two unsmoothed curves are shown in light grey. For primary creep at low stress, the strain rate decreased continuously with increasing time (**a, b**) or strain (**c**). Minimum strain rates for secondary creep of high stress samples are indicated in (**a**). Dashed lines in (**a**) and (**c**) indicate linear relationships between strain rate and time or strain in log-log scale, respectively. Note the break of time-scale in (**b**). Fitted curves for primary creep of sample DOT04 ($\sigma = 148$ MPa) using different creep laws are shown in (**d**) in log (strain) vs log (time) scale. See text for details.

We fitted several suggested creep laws to our laboratory-derived creep curves (duration < 1 week). Some commonly used empirical laws describing time-dependent strain from primary creep are:

$$\text{parabolic:} \quad \varepsilon = At^m \tag{1}$$

$$\text{logarithmic:} \quad \varepsilon = A + Blog(t) \tag{2}$$

$$\text{exponential:} \quad \varepsilon = A\left(1 - Be^{-\frac{t}{t_0}}\right) \tag{3}$$

$$\text{hyperbolic:} \quad \varepsilon = Asinh[(Bt)^s] \tag{4}$$

$$\text{crack-damage:} \varepsilon = Ae^{-\frac{B}{\ln(kt)}} \tag{5}$$

with ε = strain, t = time, and A, B, m, t_0, s, k = constants. Equations (**1**) - (**4**) have frequently been used to describe the decelerating transient behavior of rocks, soils and metals (Findley et al. 1976; Gupta 1975; Karato 2008; Paterson 2013; Stouffer and Dame 1996). Recently, Brantut et al. (2013) suggested **Eq. (5)** to express crack-damage related brittle creep of rocks. In terms of strain rate-time relation, the power-law creep **Eq. (1)** predicts a slope of m-1 in a double-logarithmic plot. For logarithmic creep (**Eq. 2**) the slope of strain rate versus time should be -1, which does not agree with our measurements (**Fig. 2a**). For the exponential creep law (**Eq. 3**), the logarithmic strain rate should decrease linearly in time. However, a constant slope of -log(e)/t_0 does not match our results that rather suggest a non-linear relationship (**Fig. 2b**). The exponential creep equation 3 is based on the Zener rheological model. This phenomenological model is composed of a combination of linear elastic springs and a linear viscous dash-pot (i.e., the standard linear solid). If the mechanical behavior does not depend on deformation history, a mechanical equation of state may exist and the relation between strain and strain rate can be described in the form $\varepsilon = A\dot{\varepsilon}^r$, where $\dot{\varepsilon}$ is strain rate and A and r are constants (Hart 1970; Karato 2008). In double-logarithmic space this would result in a linear relation with slope r, in contrast to what is suggested by our

measurements (**Fig. 2c**). This implies that the creep behavior of shales does indeed depend on deformation history and stress path, as expected for porous rocks.

Using a non-linear fitting procedure, we fitted **Eqs. (1 − 5)** to the creep curve of sample (DOT04). The test performed on this sample had the longest duration of about 1 week (**Fig. 2d**). The corresponding fit-parameters A, B, m, t_0, s, k and the fitting determination coefficients (r_{fit}^2) for the whole (inelastic) test duration of $\approx$ 1 week are given in **Tab. 2**. The best fit with highest r_{fit}^2 is obtained by the hyperbolic creep law, in descending order followed by the parabolic, crack-damage, logarithmic and finally exponential relationship (**Tab. 2**). Except for the Zener model, all others show a relatively good match with the data at test durations $\geq$ 5 hours, whereas for shorter duration the misfit increases (**Fig. 2d**). To compare results from all low stress experiments performed at different boundary conditions and terminated after different times, we refitted sample DOT04 in the time interval 50-5000 s. This interval of $\approx$ 1.4 h covers the duration of all low stress experiments except one (**Tab. 1**). It corresponds roughly to a strain difference of 1 % for all low stress tests. The determined fit parameters are listed in **Tab. 2**, revealing slightly different values than those obtained after one week duration.

Table 2 Primary creep fit parameter for sample DOT04

creep law	parameter for time-interval	22 – 595395 s (≈ 1 week)	50 – 5000 s (≈ 1.4 h)
parabolic	A	0.02340	0.02738
	m	0.08117	0.06474
	r_{fit}^2	0.99858	0.99972
	strain after 3 years	0.104 (92.9%)	0.090 (80.4%)
logarithmic	A	0.00514	0.0237
	B	0.01096	0.00641
	r_{fit}^2	0.98809	0.99861
	strain after 3 years	0.093 (83.0%)	0.075 (67.0%)
exponential	A	0.06847	0.0474
	B	0.01843	0.00984
	t_0	1.58263×10^5	1.4184×10^3
	r_{fit}^2	0.97169	0.97841
	strain after 3 years	0.069 (61.6%)	0.074 (66.1%)
hyperbolic	A	0.0217	0.2374
	B	2.82	2.24×10^{-15}
	s	0.0438	0.0640
	r_{fit}^2	0.99909	0.99971
	strain after 3 years	0.112 (100%)	0.091 (88.4%)
crack-damage	A	530.15	2.84
	B	1018.30	270.96
	k	4.336×10^{42}	1.141×10^{25}
	r_{fit}^2	0.99737	0.99954
	strain after 3 years	0.101 (90.2%)	0.085 (72.3%)

Extrapolation of the experimental data using the fit parameters to estimate the strain accumulated after 3 years creep duration yields extrapolated strains between 0.112 and 0.069 (**Tab. 2).** A time period of 3 years is the typical time interval between refrac operations in unconventional reservoirs. Likely, the hyperbolic fit for one week test duration best represents the creep behavior with a resulting creep strain of 0.112 (here set to 100 %). Extrapolation from this fit is taken as the reference strain accumulated after 3 years. Extrapolating strain using a hyperbolic fit to a 1.4 h test interval yields a strain of 0.091, i.e., 11.6 % less than the reference strain. In the following, for

simplicity we use the power law fit (**Eq. 1**) to data from all tests. Compared to the hyperbolic fit the strain extrapolated to a creep period of 3 years using the power law is 7.1 % (1 week fit) and 19.6 % (1.4 h fit) less than the reference strain.

The power law fit parameters A and m for all tests showing mainly primary creep are given in **Tab. 1**. They vary for A between 0.015 - 0.062 s^{-m} and for m between 0.046 - 0.107, depending on deformation conditions. For samples that showed also secondary and tertiary creep until failure, power law parameters for primary creep for the same time interval of 50-5000s could not be estimated because most samples failed earlier (**Tab. 1**).

To our knowledge no microphysical models for semibrittle creep of multiphase materials exist, which allow predicting stress, temperature and pressure dependence of A and m. Inspection of the experimental data (**Fig. 1, Tab. 1**) suggests that parameters A and m in equation 1 increase with increasing stress and temperature and with decreasing confining pressure. To fit the data, we use a modified constitutive power law commonly used to describe the steady state creep rate (cf., **Eq. 9**) in the high temperature (ductile) regime. Here we account for the observed dependence of parameters A and m on stress, temperature and pressure using the relations $A = A_0 \sigma^{n_1} e^{-\left(\frac{Q_1 + P*V_1}{R*T}\right)}$ and $m = m_0 \sigma^{n_2} e^{-\left(\frac{Q_2 + P*V_2}{R*T}\right)}$ which yields:

$$\varepsilon = At^m = A_0 \sigma^{n_1} e^{-\left(\frac{Q_1 + P*V_1}{R*T}\right)} t^{m_0 \sigma^{n_2} e^{-\left(\frac{Q_2 + P*V_2}{R*T}\right)}} \tag{6}$$

where n is stress exponent, Q is activation energy (in kJ/mol), V is activation volume (in cm^3/mol), σ is stress (in MPa), T is (absolute) temperature (in K), P is pressure (in GPa) R is the (molar) gas constant and A_0, m_0 are rock-specific constants. In this approach, we assume that the combined operation of microphysical processes accommodating semibrittle flow of shales like dislocation slip, microcracking, granular flow, bending of sheet silicates and compaction are captured phenomenologically. The stress, temperature and pressure dependence of A and m may be also described by other relationships, but **Eq. (6)** allows comparing the derived parameter-sensitivities

to the results of high temperature creep of rocks. Taking the logarithm of **Eq. (6)** yields the following relations between A and m and σ, T and P:

$$\log(A) = \log(A_0) + n_1 * \log(\sigma) - \frac{Q_1 * \log(e)}{R*T} - \frac{P*V_1*\log(e)}{R*T} \qquad (7)$$

$$\log(m) = \log(m_0) + n_2 * \log(\sigma) - \frac{Q_2 * \log(e)}{R*T} - \frac{P*2*\log(e)}{R*T} \qquad (8)$$

where the subscripts 1 and 2 are used for the stress, temperature and pressure sensitivity of A and m, respectively. **Fig. 3** shows the corresponding plots of 10 measurements, for which at least two of the three parameters T, P and σ were fixed in the experiments (linked by dotted lines). The 11th measurement on sample DOT12 was neglected in the analysis, because it was performed at relatively high stress yielding an exceptionally high A value (**Tab. 1**). Data sets for log (A) and log (m) were fitted by multiple linear regression (broken lines in **Fig. 3**). Since m appears to be insensitive to stress (**Fig. 3b**), we fixed $n_2 \equiv 0$ (best fit estimate is n_2 = -0.03 ±0.03). In addition, the pressure-sensitivity of was fixed to V_1 = 0.92 cm^3/mol based on the almost linear slope shown in **Fig. 3e** (the best fit for all data would slightly increase this value to 3.01 cm^3/mol). The remaining fit parameters n_1, Q_1, A_0 and Q_2, V_2, m_0 are given in **Fig. 3** and **Tab. 3**. In general, the calculated regression lines show a good fit to the data, particularly for A and somewhat less for m.
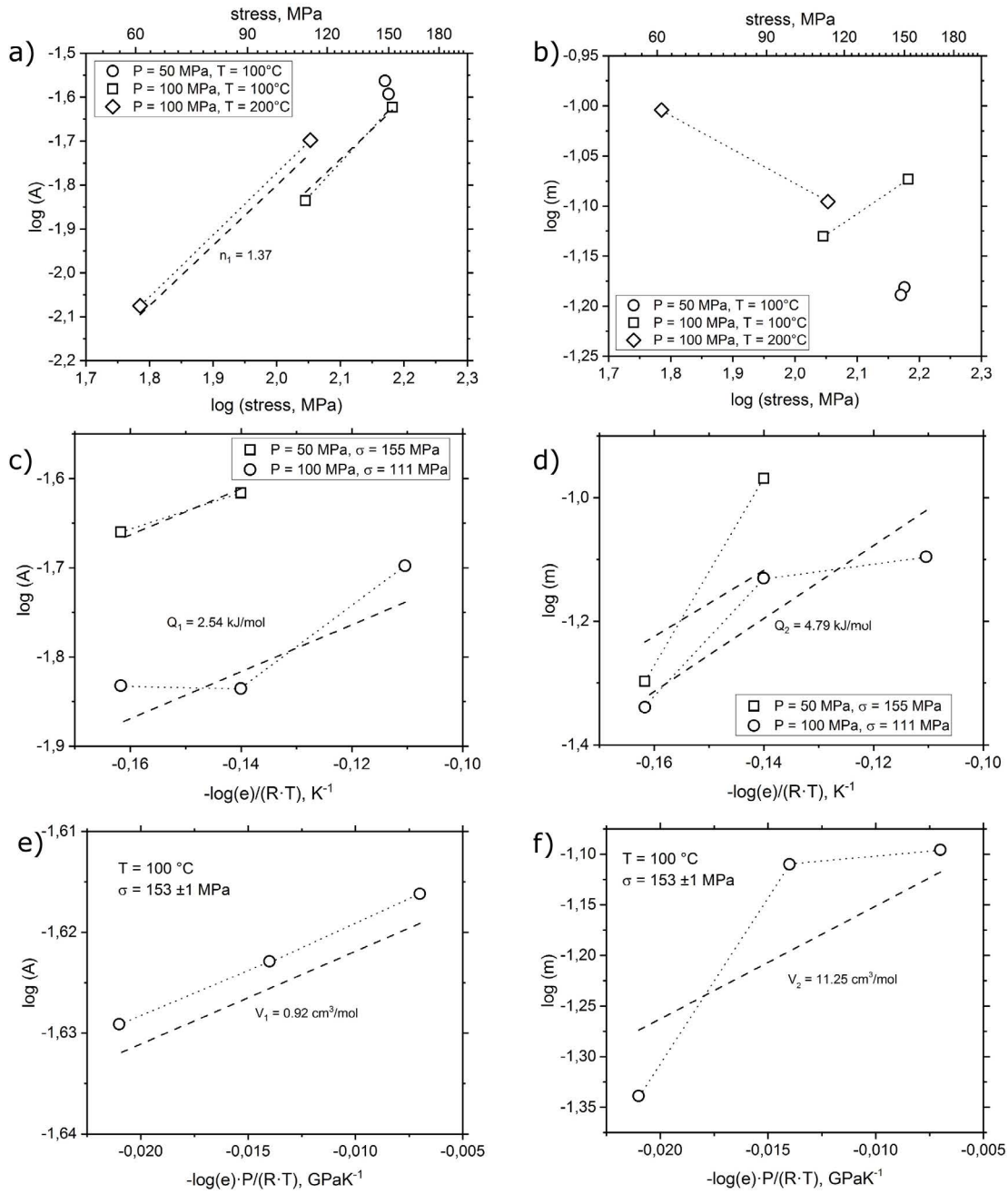
Figure 3 Variation of transient power law creep parameters A and m (cf., **Eqs. 1, 6**) with differential stress (**a, b**), temperature (**c, d**) and pressure (**e, f**). Deformation conditions are indicated. Broken lines show multiple regression fits for stress sensitivity (n), activation energy (Q) and activation volume (V) of A (subscript 1) and m (subscript 2), respectively.

Table 3 Parameters for stress, temperature and pressure dependence of primary and secondary creep

parameter	primary creep	secondary creep
n_1	1.37 ±0.10	
n_2	≡ 0	
n_3		4.8 ±18.3
Q_1	2.54 ±0.76 kJmol^{-1}	
Q_2	4.79 ±1.86 kJmol^{-1}	
Q_3		73.8 ±56.4 kJmol^{-1}
V_1	0.92 ±0.92 cm^{3}mol^{-1}	
V_2	11.14 ±6.84 cm^{3}mol^{-1}	
V_3		-11.3 ±167.2 cm^{3}mol^{-1}
A_0	(5.62 ±0.46) * 10^{-5} MPa$^{-1.37}$s^{-m}	
m_0	0.43 ±0.26	
B_0		(2.8 ±224) * 10^{-5} MPa$^{-4.8}$s^{-1}

Comparing strains extrapolated to 3 years creep period yields similar estimates (deviation <0.1 %) for multilinear fit and for values determined directly from A and m parameters given in **Tab. 1**. The standard deviation is 37 %. This is comparable to the uncertainty related to the choice of constitutive equation (**Eqs. 1 − 5**) which is also possibly affected by sample to sample variations. Since sample diameter increases with increasing strain at fixed load the applied stress decreased by 2 − 5 MPa between yield point and test termination. Accounting for this effect on extrapolation reduces 3 year strain estimates by about 3-7 %.

For extrapolation of strains from samples tested at high stresses, we calculated the minimum creep rates $\dot{\varepsilon}_{min}$ (**Fig. 2a** and **Fig. 1a − c**). The resulting set of strain rates are given in **Tab. 1**. The σ, T and P- dependence of $\dot{\varepsilon}_{min}$ was fitted to a power law creep equation used for dislocation creep in rocks and metals (Karato 2008; Paterson and Wong 2005):

$$\dot{\varepsilon}_{min} = B_0\sigma^{n_3}e^{-\left(\frac{Q_3+P*V_3}{R*T}\right)} \tag{9}$$

where B_0 is a material constant and the subscript 3 denotes the stress, temperature and pressure sensitivity for steady state creep. As for the primary creep regime, application of **Eq. (9)** to the semibrittle deformation regime is empirical and this relationship does theoretically not capture deformation processes other than dislocation creep. Taking as before the logarithm of **Eq. (9)** yields:

$$\log(\dot{\varepsilon}_{min}) = \log(B_0) + n_3 * \log(\sigma) - \frac{Q_3 * \log(e)}{R * T} - \frac{P * V_3 * \log(e)}{R * T} \tag{10}$$

Using **Eq. (10)** we fitted the measured minimum strain rates by multilinear regression yielding the parameters given in **Tab. 3**. It should be noted that uncertainties for the fitted parameters are high, presumably because the data obtained at 50 MPa pressure and 100 °C temperature (samples DOT 01, 03) appear to be very strong compared to the others. Accordingly, the error between measured and fitted strain rate is large (more than one order of magnitude) for some samples (**Fig. 4**).
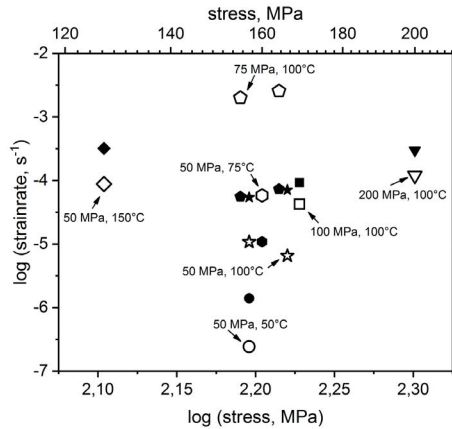
Figure 4 Measured (open symbols) and fitted (solid symbols) minimum creep strain rates of high stress samples versus applied stress. Pressure, temperature conditions are labelled.

4.2 Microstructures

Microstructures of starting material and deformed samples were investigated using scanning electron microscope (SEM) and transmission electron microscope (TEM) observations. In general, the microstructures as observed in SEM show only few changes compared to the starting material. For samples deformed in the primary creep regime, some samples show indentation of strong minerals into weaker phases (e.g., quartz into apatite, **Fig. 5b**), and bending of clays and mica (**Fig. 5c**). Samples that were deformed at higher stress until failure show formation of inter- and intracrystalline microcracks (**Figs. 5d** and **e**, respectively). Note stretching of pyrite framboids by deformation-induced sliding of microcrystallites (**Fig. 5d**). Pore collapse is also observed, in particular close to the macrofracture formed during sample failure (**Fig. 5f**), which is usually inclined by 35 ±2° with respect to the sample axis. This friction angle corresponds to a friction coefficient μ of 0.70 ±0.05 and is considerable higher than observed in constant strain rate tests on similar shale ($\mu \approx 0.2$, (Rybacki et al. 2015)).
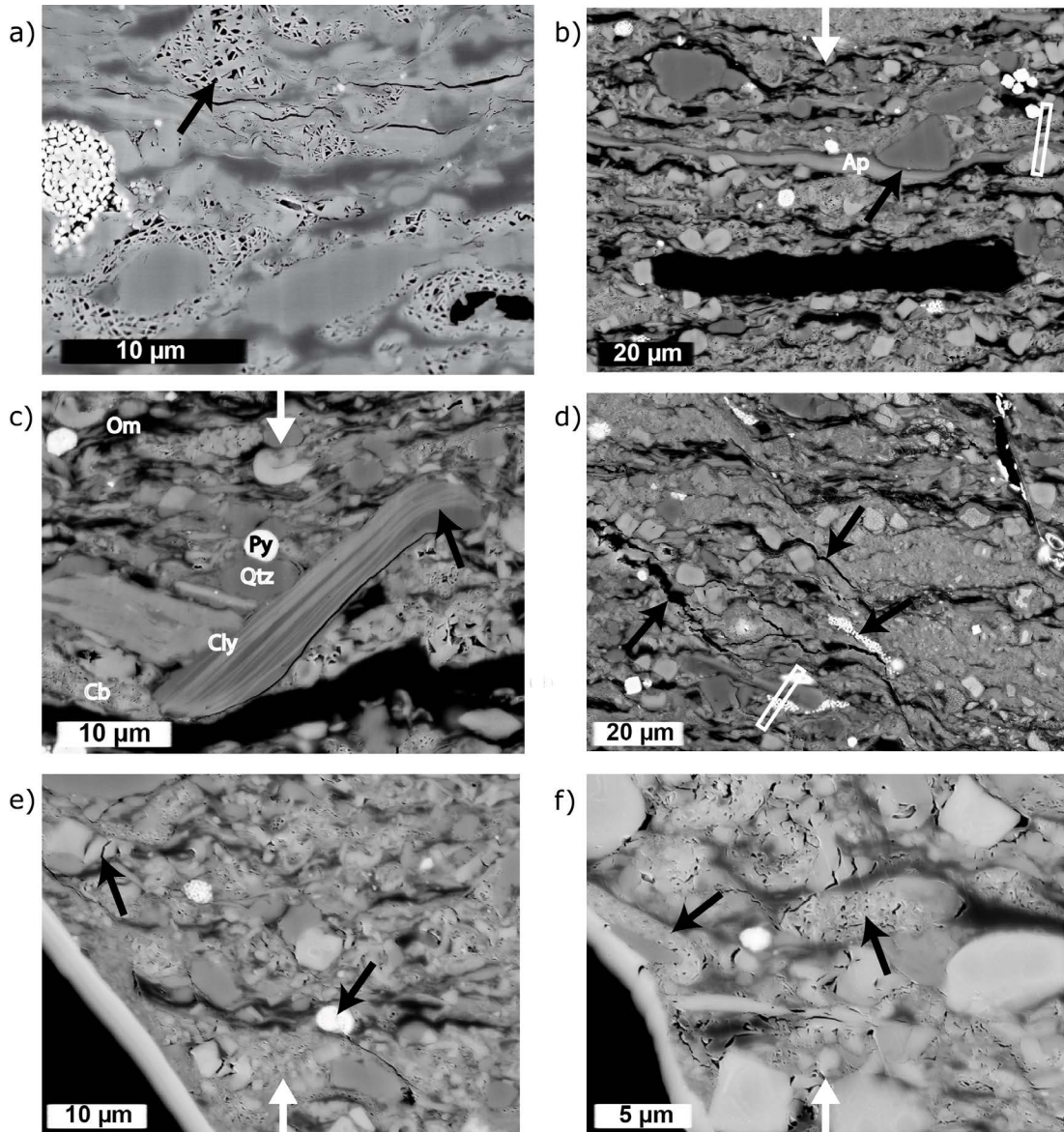
Figure 5 SEM-BSE images of undeformed (**a**) and deformed (**b-f**) Posidonia shale samples. White arrows indicate (vertical) loading direction. Main constituents are carbonates (Cb), clays (Cly), organic matter (Om), quartz (Qtz) and pyrite (Py), c.f., (**c**). Ap is apatite (**b**). Porosity is about 11 % (black arrow in **a**). Low stress sample DOT04 was deformed by primary creep, showing indentation of strong particles (Qtz) into the weaker matrix (arrow in b) and bending of phyllosilicates (arrow in **c**). High stress sample DOT07, formed until failure, reveals in addition formation of intercrystalline microcracks (arrows in d) oriented subparallel to the macrocrack (bottom left black area in **e** and **f**), intracrystalline cracks (arrows in **e**) and pore collapse adjacent to the macrocrack (arrows in **f**). Note that subhorizontal cracks are related to unloading. The white rectangles in (**b**) and (**d**) indicate the positions of FIB foils used for TEM (cf., **Fig. 6**).

TEM microscopy also reveals pore collapse in between calcite flakes under stress (**Fig. 6c, f**). The latter are partially crushed into small fragments (**Fig. 6g**). Larger calcite grains are enriched in Sr (**Fig. 6a, c**). In highly strained regions, framboidal pyrite initially containing pores and S-enriched

organic matter is fragmented and sheared (**Fig. 6e**). Clay minerals (mainly illite and kaolinite) are bent and wrapped around stronger quartz and calcite grains (**Fig. 6b, h**). In cases voids exist between clay flakes in face-to-face contact (**Fig. 6f**, top). Larger quartz aggregates are composed of fine grains with inclusions decorating grain boundaries (**Fig. 6g**). Few stretched Fluor-apatite grains consist of very small ($\approx$ 50 nm long) grains (**Fig. 6d**) that are occasionally embedded by calcite grains (**Fig. 6b**). High resolution TEM (not shown here) demonstrates that apatite is partially amorphous. Interestingly, all inspected grains are nearly free of dislocations (**Fig. 6h**) and just some larger calcite grains show few twins and low angle grain boundaries (not shown here).
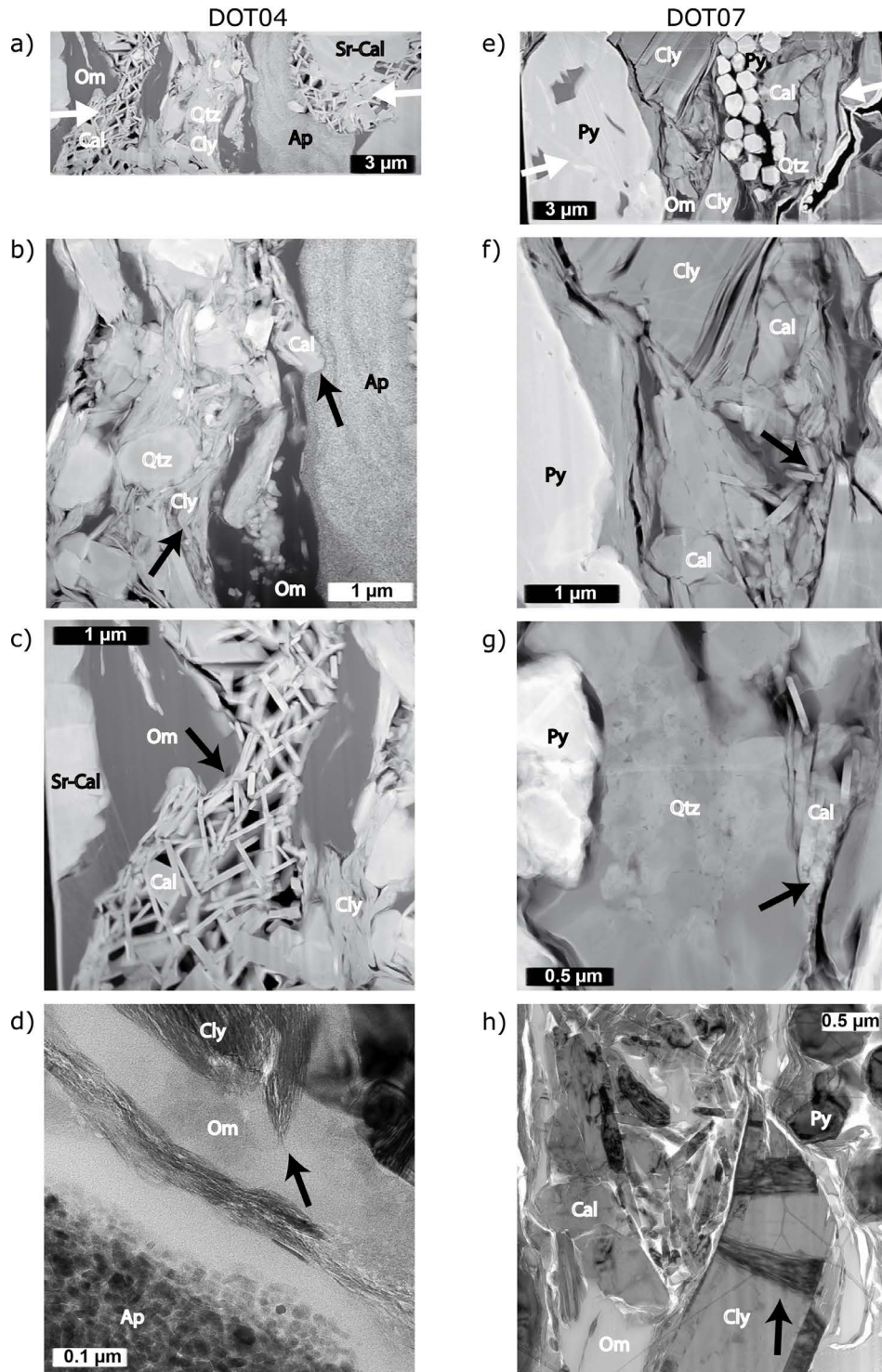
Figure 6 TEM micrographs of deformed low stress sample DOT04 (**a** − **d**) and high stress sample DOT07 (**e** − **f**). White arrows in overview images (**a**) and (**f**) indicate (subhorizontal) loading direction. For mineral abbreviations see **Fig. 5**. Cal is pure calcite and Sr-Cal is Sr-bearing calcite. In some places, the pore space between calcite flakes is reduced normal to the loading direction (black arrows in **c** and **f**). Calcite flakes are crushed if squeezed between strong neighboring grains (arrow in **g**) and embeds apatite (right arrow in

b), which is composed of abundant small grains (bottom left in **d**). Clays around strong particles are bent (left arrow in **b**, arrow in **h**) and embed the organic matter (arrow in **d**). Bright field images (**d, h**) show almost no dislocations within all minerals.

5 Discussion

The time-dependent (inelastic) creep strain response to an applied constant load is subdivided into primary, secondary and tertiary creep. Here, we discuss observations from shale samples deforming in primary and secondary creep regime, as indicated by mechanical data and microstructure observation.

5.1 Deformation Mechanisms and Constitutive Equations

The laboratory deformation experiments on Posidonia shale at elevated pressure and temperature reveal different creep behavior and deformation mechanisms, depending on applied stress and P, T - conditions. For axial stresses less than 84 – 90 % of the short-term compressive strength, samples deformed by primary creep with continuous hardening leading to a progressive strain rate reduction with increasing time and strain. The microstructural observations suggest that creep strain is primarily accommodated by deformation of the weak mineral and organic constituents (clays, organic matter), and pore space reduction. This may have involved frictional sliding of very fine mineral grains. Where present, organic material likely acts as a lubricant between grains and clays are expected to allow easy glide along aligned platy aggregates.

At higher stress, samples show apparent steady state and finally accelerating deformation, leading to shear failure. Deformation is locally accommodated by pronounced pore collapse and formation of inter- and intracrystalline microcracks. Progressive crack coalescence likely leads to macroscopic failure of samples. The Posidonia shale tested in this study contains a cumulative fraction of organic matter, clays and pores of about 44 vol% accommodating most of the strain. Crystal plastic deformation is limited to bending and intracrystalline gliding of clay layers and twinning in calcite grains.

Since the samples were not dried, chemical reactions may also lead to subcritical crack growth by stress corrosion. Time dependent creep strain and static fatigue of brittle rocks were explained by this thermally activated mechanism, where the crack velocity depends on humidity, stress intensity factor at the crack tip and temperature (e.g., Atkinson and Meredith 1987; Ciccotti 2009; Kranz 1980; Kranz et al. 1982; Heap et al. 2009a, 2009b). We expect that stress corrosion at least partially contributed to creep of our samples, although this cannot be verified by microstructural observations. High stress samples were deformed at about 84 – 90 % of the short-compressive strength indicating that dilatant behavior may have been initiated if compared to brittle creep of porous sandstone at room temperature, where the onset of dilatancy requires stresses less than 80-90 % of the compressive strength (Heap et al. 2009a). Unfortunately, we were not able to measure volumetric strain during the experiments allowing to record a potential onset of dilatant behavior of samples deformed under high stress.

Primary creep is usually described by empirical mechanical models that consist of a combination of elastic (spring) and viscous (dashpot) elements for viscoelastic creep (Hagin and Zoback 2004; Karato 2008; Masuti et al. 2016; Paterson 2013), which may be complemented by plastic (sliding friction) bodies, (e.g., Bonini et al. 2007; Jiang et al. 2013). These rheological models are often applied to high-temperature dislocation and diffusion creep of rocks and metals. The models do not account for brittle processes like microcrack formation and propagation, which may lead to cataclastic or granular flow. Mainly for deformation in the brittle field, microcrack damage evolution and stress corrosion was related to transient creep (Bikong et al. 2015; Brantut et al. 2012; Brantut et al. 2014; Brantut et al. 2013; Fjær et al. 2014; Heap et al. 2009a; Li and Shao 2016). Most of these models suggest a parabolic, logarithmic or exponential constitutive equation for brittle creep (e.g. **Eq. (5)** as above).

For steady state creep of rocks and metals, a flow law as in **Eq. (9)** is commonly applied to describe deformation accommodated dominantly by dislocation activity and diffusion of point defects (Frost and Ashby 1982; Karato 2008; Ranalli 1987). For brittle creep of rocks controlled by stress corrosion, the relation between minimum creep rate in the secondary regime and applied stress can be similarly described in a power law form (Heap et al. 2009; Brantut et al. 2012).

However, as observed here, semibrittle deformation of shales involves a complex interplay of several micromechanisms. The respective contributions of each mechanism may change with progressive strain. In particular if crack damage accrues leading to final failure, the time dependence of the secondary (steady state) creep interval may be regarded as a minimum rather than a steady state creep rate that would allow continuous deformation without failure (Brantut et al. 2012; Main 2000; Wilshire and Burt 2008).

We are not aware of any constitutive equation that describes primary or secondary creep in the semibrittle field. Due to the complexity of deformation mechanisms acting together during creep of multiphase shales, their mechanical behavior may be described by empirical laws such as **Eqs. (6) and (9)**. This approach is regarded to be acceptable to study fracture healing properties since experimental pressures and temperatures are similar to in situ values and the dominant micromechanisms accommodating deformation are not expected to change between experimental duration and time intervals of several years relevant in the field. Also, differential stresses applied in experiments are expected to reflect the enhanced stresses induced by proppant embedment or in the load-bearing parts of self-propped fractures.

5.2 Effect of Stress, Pressure and Temperature on Primary Creep

5.2.1 Effect of Stress

For primary creep, we used the power law description of creep strain as a function of time (**Eq. (6)**). Fitting **Eq. 6** to our data from tests performed at different pressures and temperatures indicates that the stress dependence n_2 in the power law (expression for the time exponent m) vanished. The parameter A depends on stress raised to a power of $n_1 \approx 1.4$ (**Eq. (6), Tab. 3**). This result suggests that creep shows a non-linear dependence on stress, i.e., creep is not Newton-viscous, for which n_1 would be equal 1. In contrast, creep experiments on a number of American shales (Barnett, Haynesville, Marcellus, Eagle Ford, Fort St. John, Bakken, Three Forks, Lodgepole) showed linear-viscous behavior instead (Almasoodi et al. 2014; Li and Ghassemi 2012; Rassouli and Zoback 2015; Sone and Zoback 2013, 2014; Yang and Zoback 2016). However, in

these earlier studies the applied differential stresses ($\sigma < 90$ MPa, mostly < 40 MPa) and the confining pressures ($P < 60$ MPa, mostly $15 - 40$ MPa) were substantially lower compared to our tests performed at pressures $P \geq 50$ MPa and stresses $\sigma \leq 200$ MPa (**Tab. 1**). Only for Marcellus shale deformed at $P = 19$ MPa viscosity was reported to become nonlinear for $\sigma > 80$ MPa (Li and Ghassemi 2012). In addition, maximum strains achieved in these tests were relatively low (usually $< 10^{-4}$) compared to our study with inelastic strains $> 10^{-2}$.

Unfortunately, no deformation mechanisms were reported in the studies cited above. We speculate that pore space compaction and closing of preexisting microcracks may have accommodated much of the measured strain, whereas in our experiments other additional processes (plastic deformation of weak phases, grain boundary sliding and limited microcracking) were active, likely resulting in stress exponent n_1 higher than 1. In addition, almost all experiments on North American shales were performed by stepwise increasing the stress, which may have influenced subsequent creep steps at higher loads due to the irreversible modifications of the microstructure in preceding steps at low loads. This approach may have resulted in lower strain rates than would be obtained in single runs at constant stresses as presented here. Accordingly, the expected stress sensitivity n_1 in our tests is likely higher than that reported on shales in the literature.

5.2.2 Effect of Pressure

We observed that increasing confining pressure reduced the total strain accumulated per time during primary creep of Posidonia shale (**Fig. 1e**). This indicates that strength increased with increasing confining pressure as expected for the semibrittle behavior of this shale (Rybacki et al. 2015). The strengthening effect is presumably caused by enhanced compaction of voids and microcracks with increasing pressure. Also, frictional sliding of grains at high P is expected to contribute less to deformation. The effect of pressure on crystal plastic deformation (of the weak phases) is usually small, yielding activation volumes for high temperature steady state creep rate of common silicates in the range of $\approx 10 - 40$ cm^3/mol (Bürgmann and Dresen 2008). Interestingly, we obtained $V_2 \approx 11$ cm^3/mol as pressure sensitivity of m in low temperature transient creep of shales, which is of the same order as for high-temperature creep of silicates. In contrast, V_1 is close

to zero as is the measurement error indicating that the influence of pressure on A is minor or even negligible (**Tab. 3**). It should be recalled, however, that the tested shales deformed in a semibrittle regime. Therefore, we point out that the exponential pressure dependence of primary creep strain expressed by an activation volume is purely empirical. The estimated pressure dependence may not capture the pressure sensitivity of brittle deformation mechanisms resulting in pore space compaction or dilatant microcracking. Using activation volumes V_1 and V_2, the pressure-related creep strain after 3 years at a temperature of 75 °C and stress of 30 MPa would be reduced by about 11 % if pressure increased from 50 to 75 MPa (corresponding to a stress change from 2 to 3 km depth, respectively), which is mainly related to the reduction of m. For comparison, for an increase in differential stress at depth from 30 to 40 MPa, creep strain accumulated after 3 years is about 48 % larger. It is interesting to note that low stress - low strain creep tests performed on Barnett, Haynesville, Eagle Ford and Fort St. John seem independent of confining pressure between $P = 10$ and 60 MPa (Sone and Zoback 2013, 2014). Creep strain even increased with increasing confinement at $P = 0.1 - 19$ MPa for Barnett, Haynesville and Marcellus shale (Li and Ghassemi 2012). This is in stark contrast to our observations. In those studies tests were performed at lower pressures and stresses compared to the ones presented here. It is conceivable that in those studies shear enhanced compaction significantly increased with increasing confinement (Almasoodi et al. 2014). Instead in our tests performed at relatively higher pressures, samples may have already compacted during the isostatic pressurization stage prior to axial loading.

5.2.3 Effect of Temperature

To our knowledge, the influence of temperature on creep of shales was not investigated so far. Constant strain rate tests on shales at elevated pressure and temperature show that the strength decreases with increasing temperature as expected for deformation that involves plastic processes (Ibanez and Kronenberg 1993; Rybacki et al. 2015). We also observed increasing primary creep strain with increasing temperature (**Fig. 1f**), presumably related to the temperature sensitivity of deformation of weak phases. However, the obtained activation energies of $Q_1 \approx 2.5$ kJ/mol and $Q_2 \approx 4.8$ kJ/mol are very low compared to values for high-temperature plasticity of silicate rocks, which typically amount to hundreds of kJ/mol for dislocation or diffusion creep, depending on

composition, water content and dominating deformation mechanism (Bürgmann and Dresen 2008). For creep of fine grained carbonates Q is about $200 - 300$ kJ/mol (e.g., Rybacki et al. 2003), for mica $\approx 50 - 90$ kJ/mol (Ibanez and Kronenberg 1993) and for bitumen ≈ 145 kJ/mol (Mouazen et al. 2011). Stress corrosion, which is also temperature sensitive, yields Q-values between 30 and 50 kJ/mol in the secondary regime (Brantut et al. 2012), which is also higher than Q_1 and Q_2. The difference to the low Q values obtained in this study may partially arise from the comparison of transient with steady state deformation conditions and from the nature of predominant deformation processes, which in case of shale deformation is a combination of plastic and brittle mechanisms. Semibrittle deformation likely has relatively low temperature sensitivity since the brittle mechanisms involved are much less affected by T than thermally activated plastic deformation (Lockner 1995). In line with that, we observed only a minor dislocation activity in our samples, indicative of high temperature creep deformation. In addition, partial dehydration of clay minerals may have occurred at high temperature, depending on local pore fluid pressure. If so, it may have contributed to the observed temperature sensitivity of creep curves.

It should be noted that we used total strain for derivation of parameters n, Q and V. Since the total strain includes elastic deformation, these parameters, in particular n, will change if restricted to inelastic strain and may then reflect better microphysical creep processes. Here, we prefer using total strain allowing easy comparison with known literature data and extrapolation to natural conditions.

5.3 Effect of Composition, Orientation and Brittleness on Primary Creep

To estimate the influence of shale composition on primary creep, we used a slightly modified form of the power law creep equation (1):

$$\varepsilon = B * \sigma^n * t^m \tag{11}$$

where A in **Eq. (1)** is replaced by $B \cdot \sigma^n$ to be able to compare our data with data available in the literature. For Barnett, Haynesville, Eagle Ford and Marcellus shale we calculated average B and m values from published creep data provided by Li and Ghassemi (2012); Rassouli and Zoback (2015) and Sone and Zoback (2014). Mean values determined for bedding-normal and, if available, bedding-parallel deformation are summarized in **Tab. 4**, together with the approximate composition. As mentioned above, these authors measured the creep behavior at room temperature at low confining pressure and stress. For comparison to our data we set $P = 20$ MPa in line with the approximate pressure used. Note that these authors did not find any dependence of creep strain on pressure (see above) and that they measured linear-viscous creep with $n = 1$.

The resulting total creep strain after 3 years deformation at an applied stress of 30 MPa is given in **Tab. 4** and plotted in **Fig. 7** in relation to shale porosity, volumetric fraction of clay plus organic matter (ClyTOC), carbonates (Cb), and fraction of strong minerals (QFP = quartz + feldspar + pyrite). As expected from microstructural observations, the creep strain increases strongly with increasing porosity, although the error due to averaging is relatively large (**Fig. 7a**). For Posidonia shale our measured (opposing) effects of pressure and temperature on primary creep reveal that the *P-T* influence is of the same order as compositional changes. This is shown in **Fig. 7a** for simulated depths up to about 4 km (solid dots). For comparison, the orientation of the maximum principal stress with respect to bedding also has a distinct impact on the creep rate, where samples loaded parallel to bedding plane orientation are creeping at a lower rate compared to those deformed perpendicular to bedding (**Fig. 7a, Tab. 4**). The impact of water content on creep is also important as shown by Sone and Zoback (2014) for Haynesville shale dried at 100 °C in comparison to as-is samples (**Fig. 7a, Tab. 4**). Enhanced creep rates for water saturated samples compared to dry samples of Eagle Ford shale were also recognized by Almasoodi et al. (2014) and for Callovo-Oxfordian argillite by Zhang and Rothfuchs (2004). Water may enhance creep rates in various ways, for example by capillary suction and osmotic swelling, poroelastic effects in saturated rocks or enhanced microcrack development in highly stressed clay-rich rocks (Nara et al. 2011; Schmitt et al. 1994; van Oort 2003; Sone and Zoback 2014). It should be recalled, however, that

our calculated absolute values are biased by the choice of empirical flow law and used time interval for fitting as discussed above.

Table 4. Primary creep strain of various shales

shale	poro, [vol%]	QFP, [vol%]	Cb, [vol%]	ClyTOC, [vol%]	B_T [MPa^{-n}s^{-m}]	B_{II} [MPa^{-n}s^{-m}]	m_T	m_{II}	ε_T [%]	ε_{II} [%]	ε_{T-dry} [%]	ε_T [%]	ε_T [%]	ε_T [%]	$B_{porocomp}$
T [°C]					20	20	20	20	20	20	20	50	75	100	
Pc [MPa]	/	/	/	/	20	20	20	20	20	20	20	50	75	100	/
Pos[a]	11	14	42	33	$2.0\cdot10^{-5}$		0.05		0.57			0.67	0.75	0.82	0.18
Bar1[b]	5	51	2	42	$4.0\cdot10^{-5}$	$2.3\cdot10^{-5}$	0.02	0.016	0.17	0.09					0.52
Bar2[b]	1	41	52	6	$1.5\cdot10^{-5}$	$1.4\cdot10^{-5}$	0.017	0.01	0.06	0.05					0.55
Bar3[c]		60	10	30	$4.5\cdot10^{-8}$		0.35		0.08						0.63
Hay1[b]	6	33	21	40	$5.0\cdot10^{-5}$	$2.1\cdot10^{-5}$	0.05	0.038	0.38	0.13	0.27				0.37
Hay2[b]	3	23	51	23	$2.2\cdot10^{-5}$	$1.7\cdot10^{-5}$	0.037	0.025	0.13	0.08					0.31
Hay3[d]		27	8	65	$4.5\cdot10^{-5}$	$2.3\cdot10^{-5}$	0.055	0.018	0.37	0.09					0.28
Hay4[c]		25	23	51	$1.0\cdot10^{-7}$		0.47		1.78						0.29
Eag1[b]	6	24	50	20	$5.0\cdot10^{-5}$	$2.0\cdot10^{-5}$	0.058	0.04	0.44	0.13					0.32
Eag2[b]	6	15	71	8	$3.8\cdot10^{-5}$	$1.8\cdot10^{-5}$	0.058	0.038	0.33	0.11					0.23
Mar1[c]		28	9	64	$2.6\cdot10^{-7}$		0.35		0.48						0.29

poro= porosity, QFP = quartz+feldspar+pyrite, Cb = carbonates, ClyTOC = clays + organic matter, B and m = power law parameter for primary creep (cf., **Eq. 11**), ε = creep strain after 3 years at σ = 30 MPa and P, T - conditions indicated, $B_{porocomp}$ = brittleness index; subscripts T and II refer to loading perpendicular and parallel to bedding, respectively, dry = dried at 100 °C; Pos = Posidonia, Bar = Barnett, Hay = Haynesville, Eag = Eagle Ford, Mar = Marcellus; superscript a = this work, b = Sone and Zoback (2014), c = Li and Ghassemi (2012), d = Rassouli and Zoback (2015)
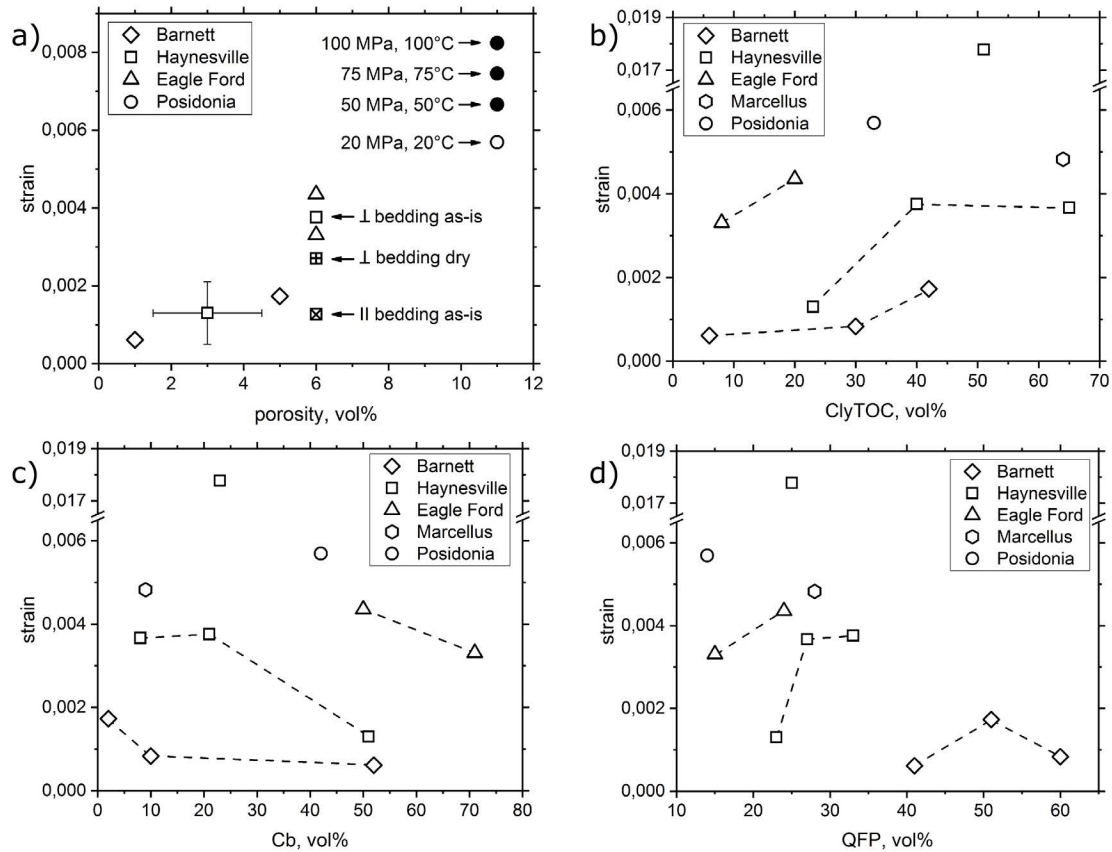
Figure 7 Calculated creep strain for primary creep of various shales after 3 years at 30 MPa stress versus porosity (**a**), fraction of clays and organic matter (**b**), carbonate content (**c**) and amount of quartz + feldspar + pyrite (**d**). Open symbols denote estimated strain at a pressure of 20 MPa and temperature of 20 °C for shales with as-is water content, deformed perpendicular to bedding. Solid dots are calculated strains for Posidonia shale at elevated temperatures and pressures simulating depth of 2, 3 and 4 km assuming a geothermal gradient of 25 °C/km and overburden of 25 MPa/km, respectively. Centered squares show the effect of drying and bedding-parallel (II) deformation on creep of Haynesville shale. Data of American shales are mean values estimated from data published (Sone and Zoback (2014); Li and Ghassemi (2012) and Rassouli and Zoback (2015).

For a given shale formation, the amount of primary creep within 3 years increases with increasing fraction of weak phases (clays and kerogen) and decreasing proportion of carbonates (connected by broken lines in **Fig. 7**), as may be expected comparing the relative strength of the mineral and organic constituents. However, at least for carbonates, this conclusion is not valid if all data of all shown shales are considered. It should be noted that one calculated strain value for Haynesville (Hay4) is much higher than the others, which is associated with the unusual high m-value and low B-value determined by Li and Ghassemi (2012). In general, strain decreases with increasing

fraction of strong (QFP) minerals, but not for single formations (broken lines in **Fig. 7d).** This increase of strain after 3 years deformation with larger fraction of strong minerals for individual formations seems counter-intuitive and may be explained only by the combined effect of all phases together on deformation as already noted for the short-term strength of shales (Rybacki et al. 2015). The same dataset is plotted in a ternary diagram of composition with superposed creep strain values given in % (**Fig. 8a**). Low strains, indicative for strong shales, are more common towards the lower left corner of the diagram, i.e., for formations with high fraction of strong phases. For individual formations with approximately similar QFP-amount (connected by broken lines in **Fig. 8a**) the combined increase of weak phases and decrease of carbonates yields slightly increasing strains, but this effect is minor compared to the volumetric effect of strong minerals. This result suggests that the capacity of building a load bearing framework of strong minerals is important for the creep behavior of shales, at least at room temperature conditions.

Figure 8 Creep strain (in %) after 3 years deformation at 30 MPa stress and 20 °C temperature, 20 MPa pressure (**a**) and brittleness ($B_{porocomp}$) determined from composition (**b**) plotted in ternary diagrams with fraction of mechanically weak phases (clay, organics, pores), strong phases (QFP = quartz + feldspar + pyrite) and intermediate strong carbonates (Cd). Data of American shales are mean values estimated from data published Sone and Zoback (2014); Li and Ghassemi (2012) and Rassouli and Zoback (2015).

The prospectivity of shales is often assumed to be linked to the so-called brittleness of rocks, where a number of different empirical definitions exist (Rybacki et al. 2016; Zhang et al. 2016a). As a

first approximation, brittleness can be simply determined from composition if P-T effects are neglected. As shown by Rybacki et al. (2016), in the brittle to semibrittle deformation regime at low depth ($\lesssim$ 4 km), brittleness may be estimated from composition using the index:

$$B_{porocomp} = \frac{F_{QFP}}{F_{QFP}+0.5F_{Cb}+F_{ClyTOC}+\phi} \qquad (12)$$

where F indicate volumetric fraction of constituents and ϕ is porosity. Brittle behavior is indicated by $B \to 1$ and ductile behavior by $B \to 0$. For B-values > 0.2 this brittleness index correlates rather well with deformation energy-based definitions (Rybacki et al. 2016). We calculated $B_{porocomp}$ (**Tab. 4**) and superposed the values in a similar ternary diagram (**Fig. 8b**). High brittleness correlates mainly with high amount of strong phases and less with the combined fraction of carbonates and weak phases, similar to creep strain. A (negative) correlation between strain and brittleness indicates that brittleness estimated from composition or short-term deformation experiments may be used to estimate the long-term fracture healing of shales (**Fig. 9**). However, for individual shale formations (e.g., Eagle Ford and Haynesville in **Fig. 9**) this correlation is not clear.

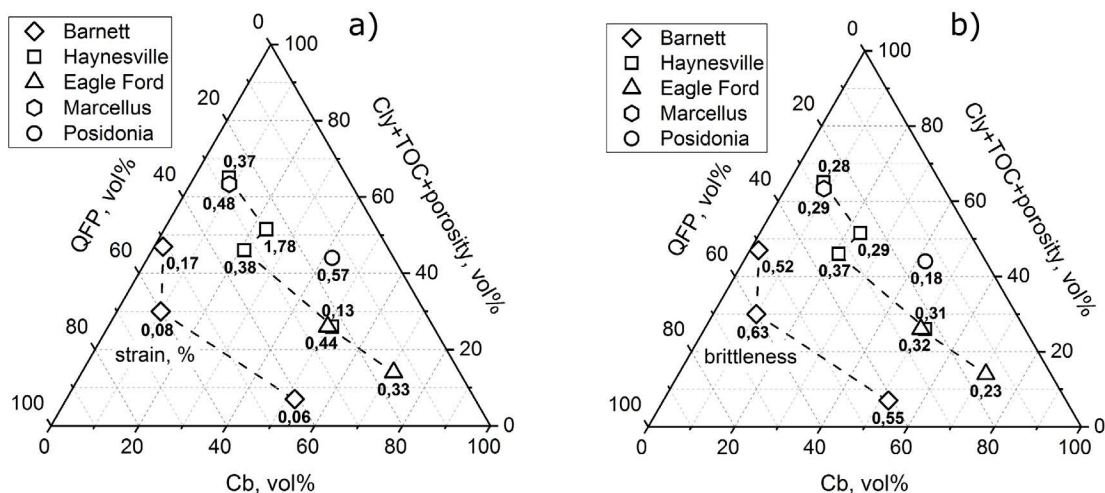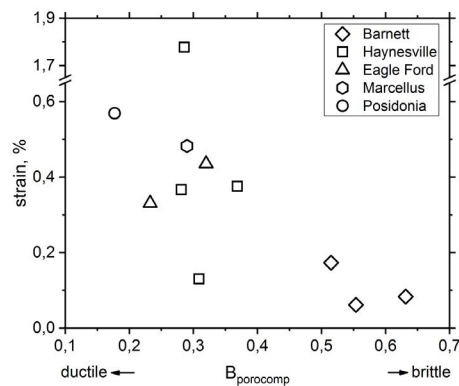**Figure 9** Creep strain (in %) after 3 years deformation at 30 MPa stress and 20 °C temperature, 20 MPa pressure versus brittleness ($B_{porocomp}$) determined from composition. Data of American shales are mean values estimated from data published Sone and Zoback (2014); Li and Ghassemi (2012) and Rassouli and Zoback (2015).

5.4 Effect of Stress, Pressure and Temperature on Secondary Creep

The best fit of **Eq. 9** to the secondary creep data yields large error bars. Irrespective of this, we find that the stress exponent $n_3 \approx 4.8$ (**Tab. 3**) clearly points to non-linear secondary creep. n-values between 3 and 5 are considered typical for high temperature dislocation creep of silicate rocks (Karato 2008). Assuming stress corrosion to be rate-limiting, the stress exponent for brittle creep of hard rocks (granite, basalt, sandstone) was found to be between $\approx$ 7 and 19 (Brantut et al. 2012). However, the stress exponent resulting from a best fit to our data likely represents the stress sensitive of a transient interplay of several different micromechanisms. We are not aware of any other published steady state creep data on shales. Few data exist on creep behavior of Opalinus clay (Naumann et al. 2007), Boom clay (Yu et al. 2015) and Callovia-Oxfordian Bure Clay (Gasc-Barbier et al. 2004) and other argillaceous rocks (Fabre and Pellet 2006; Zhang and Rothfuchs 2004). These studies show that even under low differential stress ($<$ 16 MPa) the apparent steady creep rate increases with stress nonlinearly. For Opalinus clay n is estimated close to 5 (Naumann et al. 2007). The appearance of a 'steady state' creep regime in this kind of rocks seems to depend on composition. For long time uniaxial creep tests lasting over hundreds of days, the creep rate tends to stabilize at about 10^{-11}-10^{-10} s^{-1}, sometimes also associated with dilatational behavior (Fabre and Pellet 2006; Naumann et al. 2007; Yu et al. 2015; Zhang and Rothfuchs 2004).

The temperature sensitivity of secondary creep with an activation energy Q_3 of about 74 kJ/mol is considerably higher than observed in the primary regime ($\approx$ 3 – 5 kJ/mol). This may reflect a combination of the temperature sensitivity of creep of bitumen with Q between 114 and 175 kJ/mol (Mouazen et al. 2011) and of micas with Q = 47 – 89 kJ/mol (Ibanez and Kronenberg 1993) which we assume similar to clays. For comparison, the activation energy for stress corrosion in granite and sandstone in the secondary regime is about 40$\pm$10 kJ/mol (Brantut et al. 2012), which is less than our best fit value. The estimated activation volume $V_3 \approx$ -11 cm^3/mol suggests that increasing pressure enhances shale creep rate which is counter-intuitive in the semibrittle deformation regime. However, the error bar of 167 cm^3/mol is rather large, so that V_3 should be considered just as a best fit value. Note that the influence of V_3 on the creep rate is low compared to that of Q_3, so that estimations of creep strains are still feasible.

Assuming that secondary creep can be activated at 30 MPa stress, the calculated strain after 3 years is between 0.25 % at $T = 20°$, $P = 20$ MPa and 217 % at $T = 100°$, $P = 100$ MPa, respectively, which is considerably larger than in the primary regime (**Tab. 4**).

5.5 Effect of Creep on Fracture Healing

Healing of hydraulic fractures in shale formations may occur by several mechanisms. These include swelling of clay particles adjacent to the fracture by frac water penetration, chemical reaction between host rock and proppants in the presence of fluids leading to dissolution-precipitation processes, shear-enhanced fracture closure of non-propped fractures, creep of the host rock and embedment of proppants due to stress concentrations (e.g., Fisher et al. 2013). Here, we consider the impact of creep on proppant embedment and fracture healing.

After hydraulic fracturing time-dependent deformation of asperities on the fracture plane and the embedment of proppants may lead to closure of the fracture as implied by declining production rates. The healing process will be affected by elastic deformation, due to Hertzian contact forces or with progressive indentation by an empirical power law relationship (Chen et al. 2017). Inelastic creep will further lead to time-dependent proppant embedment possibly up to complete closure. Modelling of the complex stress distributions in such a scenario is beyond the scope of this study. For simplicity, we roughly estimate the creep-related healing by assuming that the proppants or asperities are composed of stiff cylindrical pillars between fracture faces with a diameter of $d = 0.3$ mm, typical for 40/70 mesh proppants. The indentation rate $\dot{h}$ of these pillars into the shale matrix by creep may be estimated (Dorner et al. 2014):

$$\dot{h} = \dot{\varepsilon} * \frac{d}{c_2} \tag{13}$$

where the constant c_2 is 0.755 and $\dot{\varepsilon}$ is the strain rate determined in conventional uniaxial creep experiments. The stress σ_{net} acting on the indenter is related to the corresponding uniaxial stress σ by $\sigma_{net} = \sigma / c_1$ with $c_1 = 0.296$. Integration of **Eq. 13** and inserting **Eqs. 6 and 9** yields a proppant indentation depth h after time t of:

$$h_{pri} = \frac{d}{c_2} A_0 \sigma^{n_1} e^{-\left(\frac{Q_1 + P*V_1}{R*T}\right)} t^{m_0 \sigma^{n_2}} e^{-\left(\frac{Q_2 + P*V_2}{R*T}\right)} \tag{14}$$

for primary creep and

$$h_{sec} = \frac{d}{c_2} B_0 \sigma^{n_3} e^{-\left(\frac{Q_3 + P*V_3}{R*T}\right)} t \tag{15}$$

for secondary creep, respectively.

Assuming one monolayer of proppants of fixed diameter covering the entire hydrofrac then the fracture will be closed if an indentation depth of $h = 0.15$ mm into both fracture surfaces is reached. We further assume that the net stress σ_{net} acting on the indenter is 30 MPa, corresponding to a uniaxial stress σ of about 10 MPa. For primary creep the time of complete closure is then between $1.4 \cdot 10^{29}$ and $2.2 \cdot 10^{25}$ years in a depth range between 2 km (with $P = 50$ MPa, $T = 50$ °C) and 4 km (with $P = 100$ MPa, $T = 100$ °C), respectively. Assuming instead a local stress concentration of $\sigma_{net} = 150$ MPa (i.e., $\sigma \approx 50$ MPa), the time reduces to $7.2 \cdot 10^{12}$ - $2.4 \cdot 10^{10}$ years. Therefore, primary creep appears to be insufficient for fracture healing in situ, where production rates strongly declines within several years. Repeating the calculation for secondary creep, we obtain for $\sigma_{net} = 30$ MPa closure times of $13.9 - 0.3$ years in $2 - 4$ km depth, i.e., much more realistic time intervals, and for $\sigma_{net} = 150$ MPa a duration of only between 2.2 days and 1.2 hours. This comparison suggests that fracture healing can be explained by creep-induced proppant

embedment if local stress concentrations are sufficiently high so that long-term creep rates do not decline significantly with time as would be deduced if only primary creep data are considered for extrapolation. Note, however, that these estimates assume constant stress on a cylindrical indenter and an initial fracture opening of only 0.3 mm. In addition, we ignored initial elastic indentation.

6 Conclusions

Creep experiments on Dotternhausen Posidonia shale at elevated pressure and temperature show the creep strain (rate) depend on the applied stress, temperature and pressure, indicative for semibrittle deformation. Most of the induced strain is accommodated by the weak phases (organic matter and phyllosilicates) and pore collapse. Dislocation activity in carbonate and strong minerals in minor and localized microcrack evolution only evident in samples deformed until failure.

At relatively low differential stress, samples showed primary creep with continuously decreasing creep rate. At higher stress we observed secondary and tertiary creep until final failure. To account for the stress, temperature and pressure dependence of strain (rate), we applied empirical power law creep equations in the primary and secondary creep regime. Estimation of the associated indentation rates of strong proppants into hydraulically fractured shale suggest that creep-induced healing may occur by local stress concentration that exceed stresses leading to primary creep alone, even for the investigated relatively weak Dotternhausen shale.

To our knowledge, this is the first investigation of creep of shales at high pressure and temperature conditions. In the primary creep regime, a comparison of our results with published creep data of North American shales measured at ambient temperature indicates that the reservoir depth-related influence of pressure and temperature on long term-creep strain is on the same order as the effect of changes in composition, bedding orientation, or variation in water content. The magnitude of creep strain is strongly influenced by the amount of strong minerals, allowing to form a load-bearing framework at high fraction. Therefore, the long-term creep properties of shale may be correlated to composition-based brittleness at low depth.

Acknowledgements

Chapter 4: Comparison between the creep properties of Bowland and Posidonia shale at In Situ p_c, T - conditions

1 Summary

To unravel their long-term creep properties at simulated reservoir conditions, we conducted constant stress deformation experiments at elevated confining pressures, $p_c = 50 - 115$ MPa, and temperatures, $T = 75 - 150$ °C, on Posidonia (GER) and Bowland (UK) shale, which exhibit varying petrophysical and mechanical properties. Depending on applied p_c, T - conditions and sample composition, recorded creep curves exhibit either only a primary (decelerating) or additionally a secondary (quasi steady state) and subsequently a tertiary (accelerating) creep phase during deformation. At high temperature and axial differential stress and low confining pressure, creep strain is enhanced and a transition from primary towards secondary and tertiary creep behavior is observable. Creep strain of Posidonia shale, which is rich in weak constituents (clay, mica, organic content), is enhanced when compared to creep strain recorded during deformation of either carbonate-or quartz-rich Bowland shale. Electron microscopy observations revealed that the creep strain is mainly accommodated by deformation of weak minerals and local pore space reduction. In addition, micro crack growth occurred during secondary creep. An empirical correlation between creep strain and time based on a power law was used to describe the decelerating creep phase, also accounting for the influence of confining pressure, temperature and axial differential stress. The results suggest that the primary creep strain can be correlated with mechanical properties determined from short-term constant strain rate experiments such as static Young's modulus and triaxial compressive strength.

List of symbols

ε_t	Total axial strain	$\dot{\varepsilon}_{creep}$	Creep strain rate
ε_{el}	Elastic axial strain	$\dot{\varepsilon}_0$	Applied constant strain rate
ε_{inel}	Inelastic axial strain	ΔQ	Stress deficit
σ	Axial differential stress	σ^*	Characteristic activation stress
σ_{TCS}	Triaxial compressive strength	K	Strength parameter
E	Static Young's modulus	o	Strain hardening exponent
t	Experimental time	p	Strain rate sensitivity
n	Stress exponent	ϕ	Porosity
Q	Activation energy	p_c	Confining pressure
V	Activation volume	T	Temperature
R	Gas constant	a, a_0, b	constants
		b_0, c_0, α	
T_{abs}	Absolute temperature		
B_E	Brittleness		
μ	Viscosity		
$\dot{\varepsilon}_{min}$	Minimum strain rate		

2 Introduction

Currently, energy consumption depends largely on conventional and unconventional resources, e.g., coal, oil or gas (Kuchler 2017). The use of hydrocarbons from unconventional reservoirs such as shale plays may help to bridge the transition from conventional towards renewable energy resources (Hausfather 2015; Zhang et al. 2016; Kuchler 2017). For example, shale gas production

has increased tremendously over the past decades (Howarth and Ingraffea 2011; McGlade et al. 2013; Wu et al. 2017). Specifically in North America, gas production from shale reservoirs has had a major impact on the energy supply (McGlade 2013; Kuchler 2017). In Europe unconventional shale reservoirs exist (e.g., Posidonia, Bowland-Hodder formations) showing potential for economical production of hydrocarbons (Andrews 2013; Kuchler 2017; Wiseall et al. 2018).

As the permeability of shales is very low (e.g., Naumann et al. 2007; Holt et al. 2012; Villamor et al. 2016), reservoir stimulation using hydraulic fracturing is needed to increase well productivity and allow economical exploitation (Li et al. 2015). Commonly, proppants (quartz, bauxite ceramic) are added to the frac fluid to keep fractures open. However, recorded production curves of fractured wells typically exhibit a rapid decline within the first few years (Hughes 2013; Wang 2016; Al-Rbeawi 2018) as a result of reservoir depletion and fracture closure due to time dependent proppant embedment (Sone and Zoback 2014; Wang 2016; Cerasi et al. 2017). Several studies show that fracture closure is influenced by temperature (Johnston 1987; Brantut et al. 2013; Masri et al. 2014), confining pressure (Niandou et al. 1997; Petley 1999; Naumann et al. 2007; Kuila et al. 2011; Islam and Skalle 2013; Brantut et al. 2013), stress conditions (Swan et al. 1989; Chong and Boresi 1990; Ibanez and Kronenberg 1993; Kwon and Kronenberg 1994; Brantut et al. 2013; Sone and Zoback 2013a; Rybacki et al. 2015, 2017) and mechanical and petrophysical properties (Brantut et al. 2013; Rybacki et al. 2016; Cerasi et al. 2017; Morley et al. 2017; Teixeira et al. 2017).

Since proppant embedment and fracture closure depend on the long-term creep behavior of shales, we conducted a series of deformation experiments at simulated reservoir conditions. In an effort to characterize the time-dependent deformation behavior of shale rocks we conducted tests at a broad range of conditions, since only limited data on the creep properties of shale rocks exist until now (Sone and Zoback 2010, 2013b, 2014; Li and Ghassemi 2012; Almasoodi et al. 2014; Rassouli and Zoback 2015; Rybacki et al. 2017). We established empirical relations between the stress-induced creep strain and time, which also account for the influence of confining pressure and temperature on the creep rate.

3 Sample material

We examined shale rocks from two European formations, namely Lower Jurassic Posidonia (GER) shale and Carboniferous Bowland (UK) shale (**Tab. 1**). The latter comprises samples of the Upper Bowland (BOS) formation from two different localities: (1) drill core samples (BOS1 – 7, depth z ≈ 2076 – 2345 m) from the well Preese Hall 1 (PH1) drilled in 2010 (Green et al. 2012) and (2) outcrop samples (BOS_OC) collected within the county of Lancashire (NW England). Posidonia (POS) shale sample were taken from core material (Harderode-HAR, Haddessen-HAD) recovered at shallow depth (z ≈ 58 – 61 m) from research wells drilled in N-Germany in the 1980s (Gasparik et al. 2014).

Maturation measurements, VRr, indicate maximum temperatures T_{max} at peak oil maturity (VRr = 0.9 %) experienced by Posidonia (HAR) and Bowland shale. Posidonia (HAD) shale is an overmature gas shale (VRr = 1,2 %). The vitrinite reflectance of sample BOS1 (VRr = 0.67 %) indicates that shale specimens recovered from the Preese Hall well PH1 are immature.

In addition, we compare our results to published data on an immature Lower Jurassic Posidonia shale. Sample material was recovered from a quarry in SW Germany, close to the village Dotternhausen (DOT) (Rybacki et al. 2015). Details on the sample material and acronyms are given in Table 1.

The composition of specimens was determined using X-ray diffraction analysis (XRD). Samples contain a mixture of quartz (Qtz), clay (Cly), carbonates (Cb), mica (Mca), feldspar (Fsp), pyrite (Py) and organic matter (TOC) (**Tab. 1**). Porosity (incl. micro pores) was determined by Helium-pycnometry. For Posidonia and Bowland shale samples, porosity ranges between 1 and 12 % (**Tab. 1**). Note that mineral data in **Tab. 1** is given in vol%, as mechanical behavior of the samples largely depends on volumetric fraction and spatial distribution of the components. Posidonia shale is rich in mechanically weak phases (Cly + TOC + Mca + pores) and Upper Bowland shale samples are either quartz-or carbonate-rich (**Fig. 1**, **Tab. 1**). For simplification purposes, we will use the attribute 'weak' in the following for Posidonia shale with respect to sample composition, where 'weak' represents Cly + TOC + Mca and pores. Outcrop material of

Upper Bowland shale contains higher fractions of clay, mica and pores compared to core derived samples, likely due to weathering (**Tab. 1**). Microstructural observations reveal a very fine-grained matrix with a grain size $\leq$ 20 µm for Posidonia and Bowland shales (**Fig. 5 a, b**). The bedding orientation is characterized by preferred alignment of organic matter and phyllosilicates (**Fig. 5**).

For deformation experiments, cylindrical samples of 10 mm diameter and 20 mm length were prepared with their axis oriented perpendicular to bedding orientation. All specimens were dried at 50 °C for at least 48 h before starting deformations experiments.
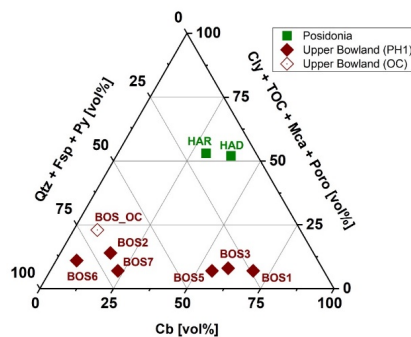
Figure 1 Ternary plot displaying mineral composition of investigated samples. Composition is separated into mechanically strong (Qtz + Fsp + Py), intermediate strong (Cb) and weak (Cly + TOC + Mca + Poro) fractions. Qtz = quartz, Fsp = feldspar, Py = pyrite, Cb = carbonate, Cly = clay, TOC = total organic carbon, Mca = mica. Mineral data are given in vol%, normalized to 100 vol% taking also the sample porosity into account. Posidonia (HAR, HAD) shales are clay-rich, whereas Bowland shales are either carbonate-or quartz-rich. Outcrop samples of Bowland shale reveal higher amounts of weak material than core derived samples. PH1 = Preese Hall 1, OC = outcrop, HAR = Harderode, HAD = Haddessen, BOS = Bowland

Table 1 Petrophysical data of investigated samples

Sample	Depth [m]	VRr [%]	$\rho\ [\frac{g}{cm^3}]$	ϕ [vol%]	TOC [vol%]	Cly [vol%]	Mca [vol%]	Cb [vol%]	Qtz [vol%]	Py [vol%]	Fsp [vol%]	CTMP [vol%]	Cb [vol%]	QFP [vol%]
HAD	60.8	1.2	2.36	12	12	32	0	46	9	1	0	52	39	9
HAR	58.2	0.9	2.46	3	11	32	0	40	15	2	0	53	30	17
BOS1	2076.2	0.76	2.68	3	2	0	3	70	22	1	2	7	69	24
BOS2	2078.1	/	2.65	3	3	3	6	18	66	2	2	14	17	69
BOS3	2079.2	/	2.66	1	3	0	2	62	31	1	1	8	60	32
BOS5	2087.1	/	2.70	3	2	0	3	56	37	1	1	7	55	38
BOS6	2342.5	/	2.61	2	4	0	7	7	78	1	3	11	7	82
BOS7	2344.7	/	2.65	2	1	0	3	23	68	1	4	7	23	70
BOS_OC	surface	0.9	2.51	8	5	4	9	8	71	2	1	23	8	69

Sample abbreviation that were used experimental procedure. HAD = Haddessen, HAR = Harderode → Posidonia formation; BOS1 – 7 → Upper Bowland formation (PH1); BOS15 → Upper Bowland formation (OC). CTMP (= Cly + TOC + Mica + ϕ), Cb and QFP (= Qtz + Fsp + Py) display weak, intermediate and strong phases in vol %

4 Experimental methods

We used a Paterson-type deformation apparatus (Paterson 1970) to perform triaxial creep experiments at elevated confining pressures (p_c = 50 – 115 MPa), temperatures (T = 75 – 150 °C) and axial differential stresses (σ = 9 – 453 MPa) (**Tab. 2**). For simplicity, we will use in the following the term 'stress' instead of 'axial differential stress'. Argon gas was used as confinement medium due to its inert properties. To prevent intrusion of the Argon gas into the samples, they were jacketed by thin (wall thickness $\approx$ 0.35 mm) copper sleeves. Axial load was measured using an internal load cell, installed within the pressure vessel. Calibration runs were performed on pure copper samples to correct for copper jacket strength. Measured axial load was then converted to stress assuming constant volume deformation. Uncertainties of resulting peak stresses are < 4 %. Recorded axial displacement, measured by a linear variable differential transformer (LVDT) was corrected for system compliance and converted to total axial strain, ε_t. The error of calculated strains is < 6 %.

All experiments were performed with loading direction normal to bedding orientation. The triaxial compressive strength, σ_{TCS}, and static Young's modulus, E, of investigated samples were determined in previous constant strain rate experiments performed at similar confining pressures and temperatures (Herrmann et al. 2018).

For creep testing, the axial load was increased to the desired level, which typically stabilized within $\approx$ 20 s. Subsequently, the load was held constant until the end of the experiment. Depending on deformation conditions, experiments were stopped either after sample shear failure, or after a fixed time if no failure occurred. The total duration of creep tests was between 22s and $\approx$ 15 days with maximum total axial strains of $\varepsilon_t \approx$ 0.5 – 5.5 % (**Tab. 2**).

Scanning electron microscope observations (SEM) were performed on mechanically polished thin sections using a Zeiss Ultra 55 Plus-microscope. High-resolution analysis of microstructures was performed using transmission electron microscopy (TEM, Fei Tecnai G2 F20 x-Twin) on focused ion beam (FIB, Fei FIB200TEM) prepared foils.

Table 2 Experimental conditions

Sample	T [°C]	p$_c$ [MPa]	σ [MPa]	ε$_{max}$ [/]	t$_{max}$ [s]	a [s^{-b}]	b [/]	ε̇$_{min}$ [s^{-1}]	Rem
HAR8	75	75	197	0.043	31134	/	/	1.9E-7	Failure
HAR9	100	75	191	0.051	1122	/	/	1.1E-5	
HAR11	80	75	190	0.041	400	/	/	1.7E-5	Failure
HAR12	85	75	194	0.041	3623	/	/	1.6E-6	Failure
HAR13	90	75	198	0.042	19385	0.00296	0.19209	/	
HAR14	95	75	193	0.046	1384	0.00354	0.26815	/	
HAR15	80	75	198	0.042	25189	0.00283	0.19466	/	
HAR16	85	75	193	0.040	649	/	/	1.1E-5	Failure
HAR17	85	75	192	0.044	802	/	/	1.1E-5	Failure
HAR18	90	75	193	0.047	4122	/	/	2.0E-6	
HAR19	90	65	191	0.044	192	/	/	5.5E-6	Failure
HAR31	90	85	195	0.045	5708	0.00506	0.17762	/	
HAR32	90	95	195	0.045	11443	0.00639	0.1379	/	
HAR33	90	105	194	0.042	22632	0.0061	0.12285	/	
HAR34	90	115	198	0.040	24904	0.00525	0.12232	/	
HAR35	90	80	196	0.041	9860	0.00418	0.16519	/	
HAR36	90	80	196	0.042	7382	0.00466	0.16356	/	
HAR38	90	75	160	0.026	20512	0.00134	0.17873	/	
HAR39	90	75	170	0.027	20144	0.00122	0.19206	/	
HAR40	90	75	180	0.030	22721	0.00121	0.20652	/	
HAR41	90	75	190	0.039	102334	0.00367	0.13731	/	
HAR42	90	75	199	0.046	106820	0.00291	0.18252	/	
HAR43	90	75	202	0.054	2485	/	/	5.0E-6	
HAR44	90	75	196	0.039	112746	0.00378	0.13258	/	
HAR45	90	75	197	0.051	175923	/	/	4.5E-8	
BOS16	90	75	209	0.022	258517	0.00274	0.07206	/	
BOS17	90	75	222	0.021	72088	0.00162	0.10299	/	
BOS18	90	75	237	0.023	69603	0.00231	0.08666	/	
BOS19	90	75	259	0.026	68736	0.00278	0.08402	/	
BOS20	90	75	301	0.035	64398	0.00507	0.08605	/	
BOS23	90	75	316	0.042	986	/	/	5.5E-6	Failure
BOS24	90	75	313	0.033	83820	0.0037	0.09255	/	
BOS25	75	75	312	0.032	82248	0.00334	0.0951	/	
BOS26	100	75	314	0.033	76620	0.00409	0.0829	/	
BOS27	150	75	301	0.044	69	/	/	1.2E-4	Failure

BOS28	125	75	313	0.037	81016	0.00611	0.07853	/	
BOS29	140	75	314	0.037	86188	0.00633	0.07272	/	
BOS30	90	115	312	0.031	82124	0.00345	0.08064	/	
BOS31	90	65	313	0.038	62229	/	/	4.2E-8	Failure
BOS33	90	90	312	0.031	88260	0.00283	0.09993	/	
BOS34	90	70	305	0.038	1429	/	/	2.1E-6	
BOS35	90	70	309	0.039	34409	/	/	9.1E-8	Failure
BOS1	90	75	436	0.035	3689	/	/	2E-6	
BOS2	90	75	450	0.018	66506	0.00373	0.05851	/	
BOS3	90	75	431	0.023	22	/	/	/	Failure
BOS5	90	75	452	0.017	87611	0.00277	0.08038	/	
BOS6	90	75	447	0.024	92759	0.00293	0.08957	/	
BOS7	90	75	453	0.014	99629	0.00265	0.05835	/	
HAD	100	50	9 – 140	0.030	1294861	/	/	/	

Sample abbreviation that were used during experimental procedure. HAD = Haddessen, HAR = Harderode → Posidonia formation; BOS1 – 7 → Upper Bowland formation (PH1); BOS16 – 35 → Upper Bowland formation (OC)

5 Results

In total, we performed 49 triaxial creep experiments. During 42 experiments, we fixed two of the three parameters p_c, T and σ and changed the remaining third parameter within a given range in order to investigate the influence of this particular parameter on the resulting creep strain behavior (**Tab. 2**). In addition, in one triaxial creep experiment axial stress was changed stepwise to investigate possible sample strain hardening effects. The three different creep phases (primary, secondary, tertiary, cf., **Fig. 3b**) as well as how to distinguish between them will be explained in detail in section 5.1 below.

After a tertiary creep phase, some samples failed along a single shear fracture inclined at $\varphi \approx 35 \pm 2$ ° with respect to the sample axis. From this we estimated an apparent coefficient of internal friction of $\mu_i \approx 0.7 \pm 0.05$.

5.1 Effect of loading history (strain hardening)

To investigate potential effects of loading history on the creep behavior of shale rocks, we performed one experiment at constant confining pressure of 50 MPa, 100 °C temperature and stepwise increased and decreased stresses between $\sigma = 9$ and 140 MPa (**Fig. 2**). The experiment was performed on Posidonia (HAD) shale, with a similar mineral composition as Posidonia (HAR) shale (**cf., Fig. 1**). During testing the axial stress was first increased in two steps (σ_1, σ_2), then decreased to σ_3 and subsequently increased up to σ_2 in four steps. Finally, the sample was loaded again by repeating stress steps $\sigma_3 - \sigma_5$ (**Fig. 2**). For the first two steps, creep strain increases with increasing stress, but for the next 4 steps the creep strain is almost negligible, even when approaching the same stress, σ_1, as applied in the first step. This was also found for the last three loading steps. Repeated loading at the highest stress level (σ_2) also reveals a considerably lower strain rate for the subsequent loading cycle (see lines in **Fig. 2**). This decrease in strain rate at similar stress demonstrates strain hardening of the shale, possibly caused by non-reversible pore collapse and closure of preexisting microcracks. Consequently, to exclude any influence of loading history on the creep behavior in the remaining tests, we performed creep experiments using a single loading step at predefined stress levels.
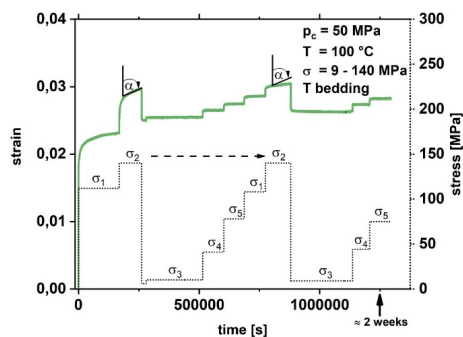

Figure 2 Creep curve of Posidonia (HAD) shale recorded at 50 MPa confining pressure, 100 °C temperature and stepwise stepped stress, σ_i. Initially, creep strain is increasing with increasing stress. Sample strain hardening is evident after repeated loading at similar stress levels by a decrease of associated strain rate (e.g., α for σ_2).

5.2 Effect of composition

Triaxial creep experiments on Bowland (PH1) and Posidonia (HAR) shale were performed at 90 °C temperature and 75 MPa confining pressure, simulating p_c, T - conditions at about 3 km depth. Creep curves of Bowland shales recovered from borehole PH1 at different depths display varying creep strengths, which change with composition (**Fig. 3a**). A clear trend accounting for varying amounts of intermediate strong (Cb) or strong (Qtz) sample constituents is not evident. Quartz-rich samples appear to be stronger than carbonate-rich samples and deform solely by primary creep at the applied stress of 442 ± 11 MPa. The latter exhibit only primary creep (BOS5) or in addition secondary (quasi steady-state) and tertiary (accelerated) creep stages (BOS1) until failure occurred (BOS3). In comparison, the Bowland (OC) shale and Posidonia (HAR) shale showed comparable creep strain values, but at considerably lower stress of 206 ± 4 MPa (**Fig. 3b**). This relatively low stress level was used since Posidonia (HAR) would fail immediately when applying higher stresses (**Fig. 3a**). Under these conditions, quartz-rich Bowland shale collected from the outcrop was distinctively stronger, exhibiting only primary creep, than weak Posidonia (HAR) shale, which showed all three creep phases before the test was terminated.
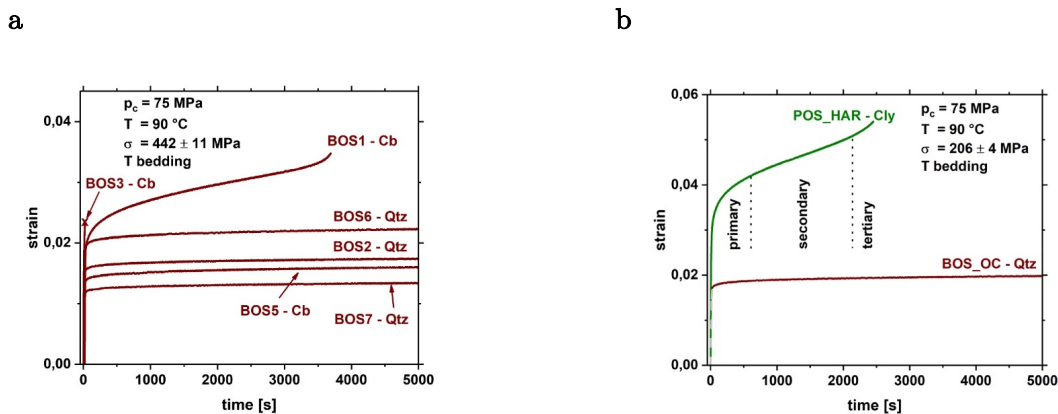

Figure 3 Creep curves of Posidonia (HAR) and Upper Bowland (PH1) shales measured at a confining pressure of 75 MPa and 90 °C temperature. The influence of sample composition on creep behavior of the rocks is separated into various Bowland shales recovered from well PH1 (**a**) and a comparison of Posidonia (HAR) and Bowland (OC) shales (**b**). A unique trend, accounting for the amount of strong (Qtz) or intermediate strong (Cb) components on the measured creep strain is not evident (**a**). However, with the exception of sample BOS5, quartz-rich Bowland shale samples (BOS7, BOS2, BOS6) appear to be stronger than carbonate-rich samples (BOS1,

BOS3). The weak Posidonia shale (HAR) is distinctively weaker than quartz-rich outcrop material of Bowland (OC) shale (**b**). Note the difference in stress in (**a**) and (**b**). Depending on mineralogy, samples display only primary (decelerating) or in addition to primary, also secondary (quasi-steady state) and tertiary (accelerated) creep (**b**). Deformation conditions are indicated. Cly = clay, Qtz = quartz, Cb = carbonate, POS = Posidonia shale, BOS = Bowland shale, HAR = Harderode, OC = outcrop, PH1 = Preese Hall 1, x = failure

5.3 Effect of confining pressure, temperature and stress

Selected creep curves of Posidonia (HAR) and Bowland (OC) shale at various p_c, T, σ - conditions are shown in **Figs. 4a, c, e** and **Figs. 4b, d, f,** respectively. Creep strain of both shale formations at T = 90 °C is generally decreasing with increasing confining pressure (**Figs. 4a, b**). Note that the applied stress on Bowland (OC) shale (σ ≈ 300 MPa) is about 100 MPa higher than exerted on Posidonia (HAR) samples (σ ≈ 200 MPa). In most cases, samples deformed at low confining pressure display primary creep followed by secondary and tertiary creep including sample failure, indicated by (x) in **Fig. 4**. In contrast, at high confining pressure, samples deformed only by primary creep. Outliers, which do not follow the general trend are indicated by dashed lines in **Fig. 4**. They reflect sample to sample variations caused by the relatively strong compositional heterogeneity of shale rocks (Könitzer et al. 2014; Ougier-Simonin et al. 2016; Ilgen et al. 2017).
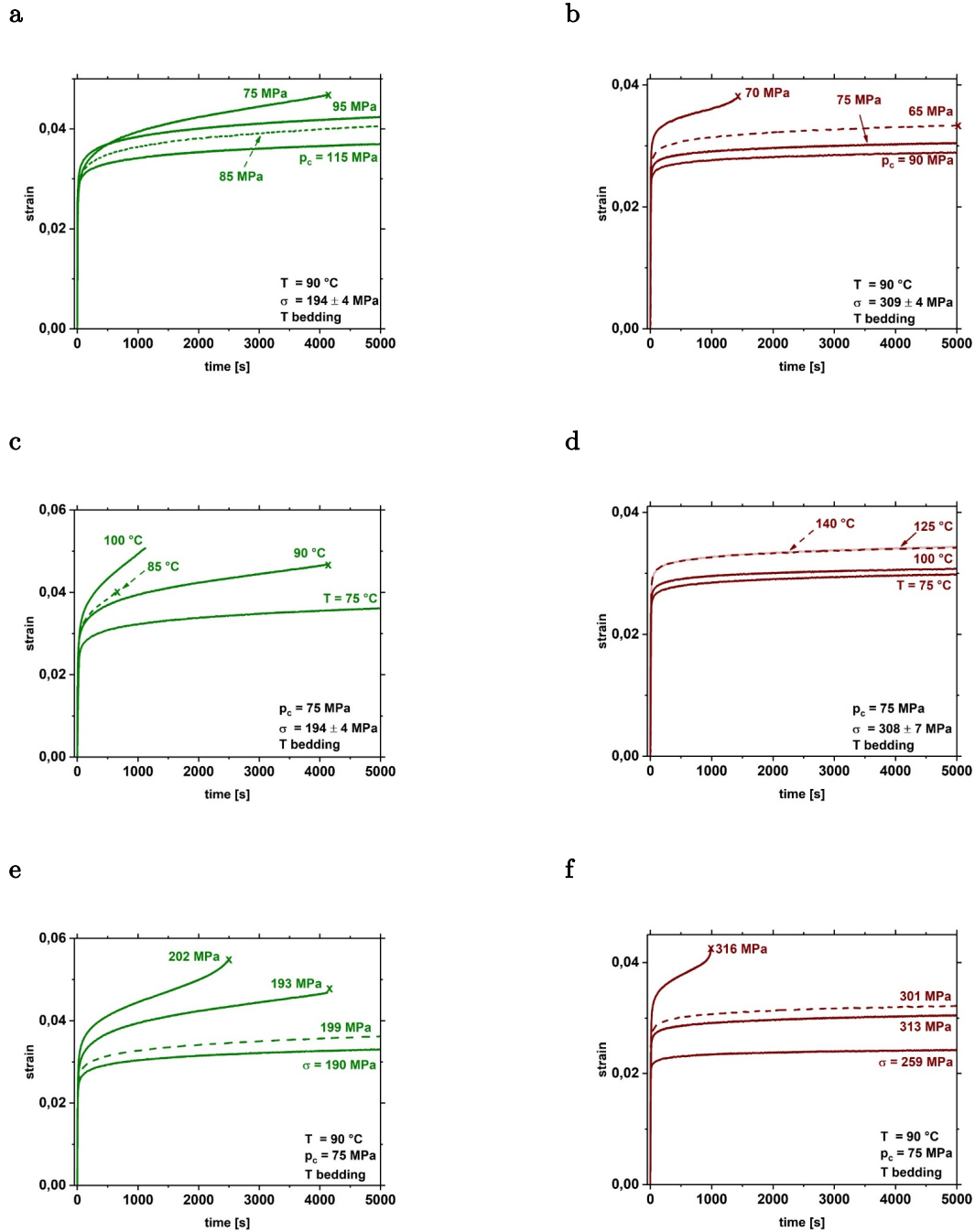
Figure 4 Selected creep curves of Harderode Posidonia (HAR) (**a, c, e**) and Bowland (OC) shale (**b, d, f**) in relation to a variation of confining pressure (**a, b**), temperature (**c, d**) and stress (**e, f**). Creep curves display mainly primary creep. At high temperatures and stresses and at low confining pressures, the creep curves reveal in addition to primary also secondary and tertiary creep, leading to failure of some samples, as indicated (x). In general, with increasing confining pressure, the creep rate of both shales is reduced, whereas it is enhanced with increasing temperature and stress. Outliers of this overall trend are indicated by dash lines. Weak Posidonia (HAR) shale is more sensitive to changes in confining pressure, temperature and stress than quartz-rich Bowland (OC) shale. For comparison, all curves were cut off at 5000 s, but the duration of most tests was much longer (**Tab. 1**). Deformation conditions are indicated.

At similar stresses and constant confining pressure of 75 MPa, the creep strain of Posidonia (HAR) and Bowland (OC) shale is increasing with increasing temperature, but with a higher sensitivity in Posidonia (HAR) shale (**Figs. 4c, d**). Posidonia (HAR) shale loaded at high temperature deformed also by secondary creep, but Bowland (OC) shale showed only primary creep behavior in the investigated temperature range.

The effect of increasing stress at p_c = 75 MPa and T = 90 °C on creep of Posidonia (HAR) and Bowland (OC) shale is shown in **Figs. 4e, f**. Samples subjected to high stress display all 3 creep phases (primary, secondary and tertiary) in contrast to samples deformed at low stress, which reveal only primary creep behavior. The transition from primary creep to secondary and tertiary creep of both shales appears to occur within a relatively narrow stress range of $\Delta\sigma \approx$ 15 MPa.

In summary, the creep behavior of both shales is sensitive to the applied p_c, T, σ - conditions. Quartz-rich Bowland (OC) shale is less sensitive to variations of p_c, T, σ - conditions than weak Posidonia (HAR) shale. Most creep experiments were finished within one day, either by manual termination or by sample failure (**Tab. 1**).

5.4 Microstructures

The microstructures of deformed samples of Posidonia (HAR) and Bowland (OC) shale were investigated using scanning electron microscopy (SEM, **Fig. 5**) as well as transmission electron microscopy (TEM, **Fig. 6**). The microstructures of samples of both shales that were deformed at low stresses in the primary creep regime (**Fig. 5c, d**) are hard to distinguish from those of undeformed samples (**Fig. 5a, b**). Deformed Posidonia (HAR) shale sometimes reveals slightly deformed pyrite (**Fig. 5c**, bold black arrow) and intracrystalline fracturing of dolomite (**Fig. 5c**, open black arrows). Bowland (OC) shale may displays minor bending of phyllosilicates (**Fig. 5d**, bold black arrow).

Figs. 5e-h show microstructures of samples that failed after tertiary creep. The main shear fracture within Posidonia (HAR) samples is mainly composed of crushed material with small grain size (**Fig. 5e**). Deformation is accompanied by sheared framboidal pyrite aggregates (open black arrows) and rotation of larger grains close to the main fracture (bold black arrow). Close to the tip of the fracture (indicated by the dashed white line in **Fig. 5g**), intracrystalline fractures within calcite grains (bold black arrow) are visible. The main fracture terminated at the weak organic matter (center of **Fig. 5g**). Within Bowland (OC) shale (**Fig. 5f**) a discrete fracture developed, partially formed by coalescence of broken dolomite grains and transecting weak phyllosilicates (bold black arrows). Strong pyrite grains are often bypassed (open black arrow). Larger quartz grains show intra- (dashed, open black arrows) and intercrystalline (dashed, bold black arrow) fractures oriented subparallel to the main fracture.

In a Bowland (OC) shale sample deformed in tertiary creep, intracrystalline fracturing of apatite (open black arrow) and bending of phyllosilicates (bold black arrow) is observed (**Fig. 5h**).
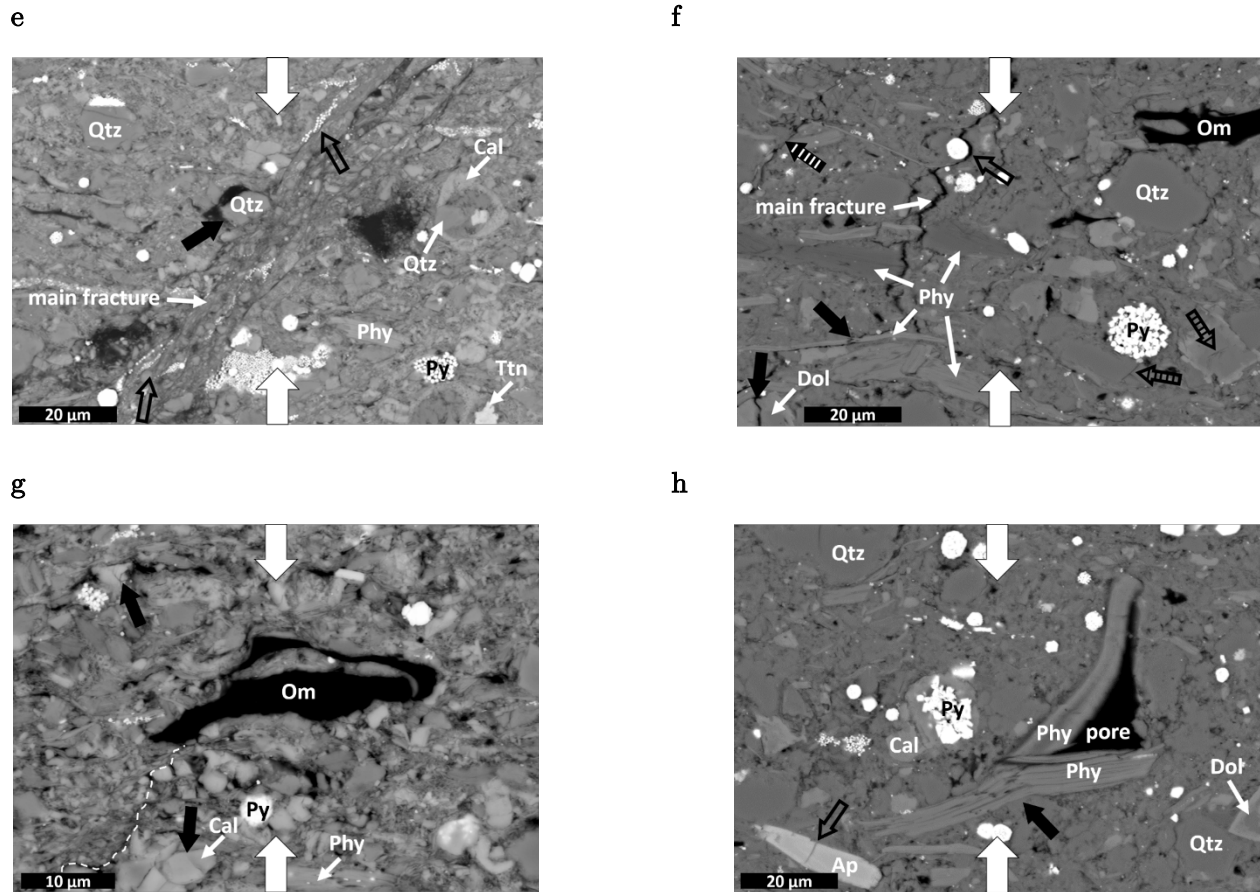
a

b

c

d
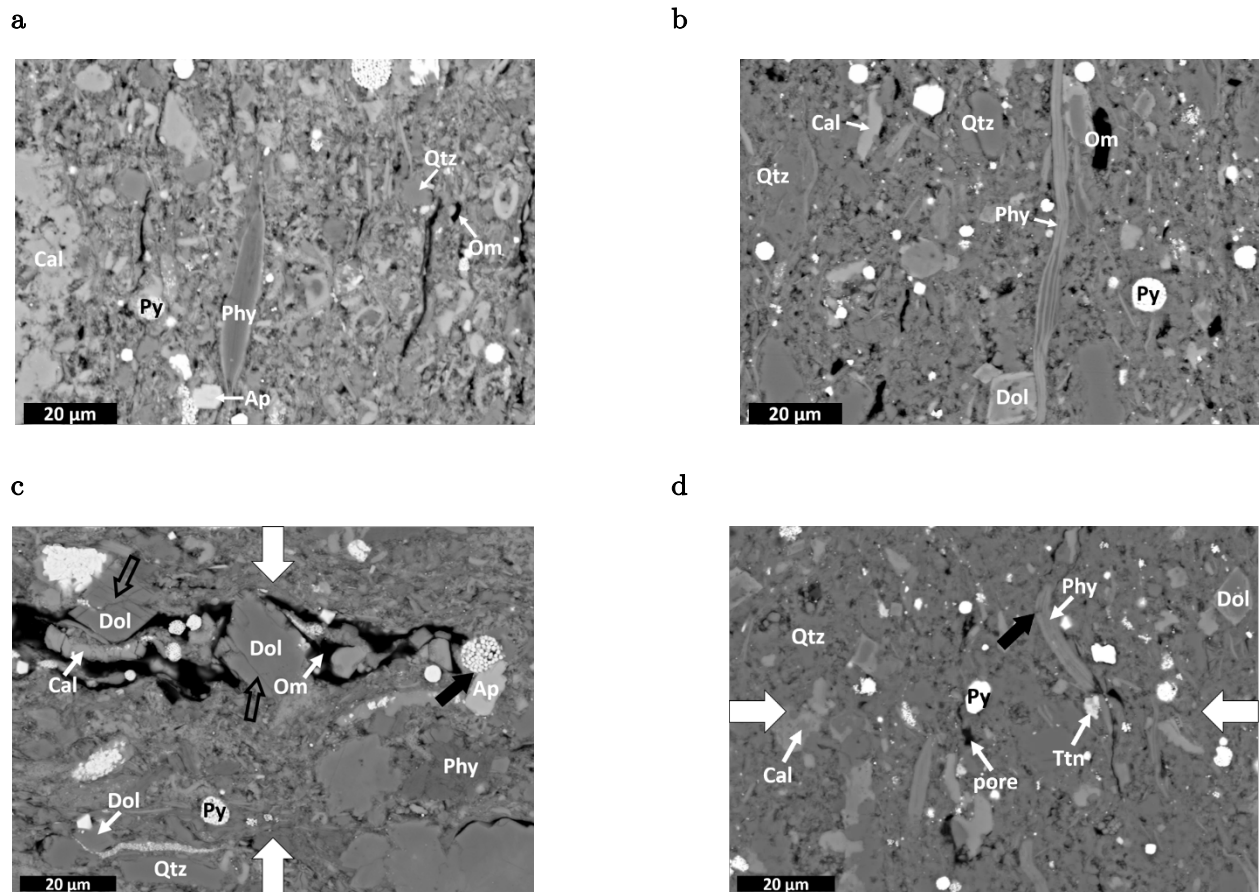
Figure 5 SEM-BSE images (**a, c, e, g**) of low porous ($\approx$ 3 %) Posidonia shale (HAR) and (**b, d, f, h**) porous ($\approx$ 8 %) Bowland shales (OC). (**a**) and (**b**) show undeformed samples. (**c** − **h**) display samples deformed by primary creep and (**e** − **h**) those deformed until failure. Bold white arrows indicate loading direction. Main constituents of both shales are mechanically weak phyllosilicates (Phy) and organic matter (Om), intermediate strong calcite (Cal) and dolomite (Dol) and strong quartz (Qtz) and pyrite (Py). Ap and Ttn are apatite and titanite, respectively. Pores and organic matter appear nearly black, quartz is medium grey, phyllosilicates and carbonates (Cal + Dol) are light grey and pyrite is almost white. Microstructures indicative of primary creep (**c, d**) are hardly visible, but can be identified by deformed pyrite aggregates (**c**, bold black arrow) and formation of intracrystalline fractures in dolomite (**c**, open black arrows) for Posidonia shale (HAR38). Primary creep of Bowland shale (BOS16) may induce bending or minor fracturing of phyllosilicates (**d**, bold black arrow). Tertiary creep behavior (**e** − **h**) of both shales is accompanied by fracture initiation and propagation. Additional deformation mechanisms within Posidonia shale (HAR43) are crushing and shearing of pyrite framboids (**e**, open black arrows) and rotation of larger quartz close to the main fracture (**h**, bold black arrow). Bowland shale (BOS34) exhibit fracturing of dolomite and phyllosilicates (**f**, bold black arrows), but no deformation of pyrite grains (**f**, open black arrow). In addition, inter (**f**, dashed, bold black arrow)- as well as intracrystalline (**f**, dashed, open black arrows) fractures subparallel to the main fracture are evident. Near the fracture tip of Posidonia (HAR) shale (**g**, dashed white line), deformation is indicated by intracrystalline fractures in calcite (**g**, bold black arrow). Bowland (OC) shale shows in addition to intracrystalline fractured apatite (**h**, open black arrow) also bending of phyllosilicates little beyond the fracture tip (**h**, bold black arrow).

High resolution TEM micrographs of shales deformed by primary creep are shown in **Fig. 6**. The overview images of Posidonia (HAR) and Bowland (OC) shale show little evidence of brittle deformation features (**Fig. 6a, b**, respectively). Instead, deformation of Posidonia (HAR) shale appears to be accommodated by local pore space reduction between calcite flakes (**Fig. 6c**, bold black arrow) and bending of weak phyllosilicates around strong quartz grains (**Fig. 6c**, open black arrow). Primary creep of Bowland (OC) shale is mainly assisted by bending of weak phyllosilicates around stronger grains, e.g., apatite (**Fig. 6d**, bold black arrow).
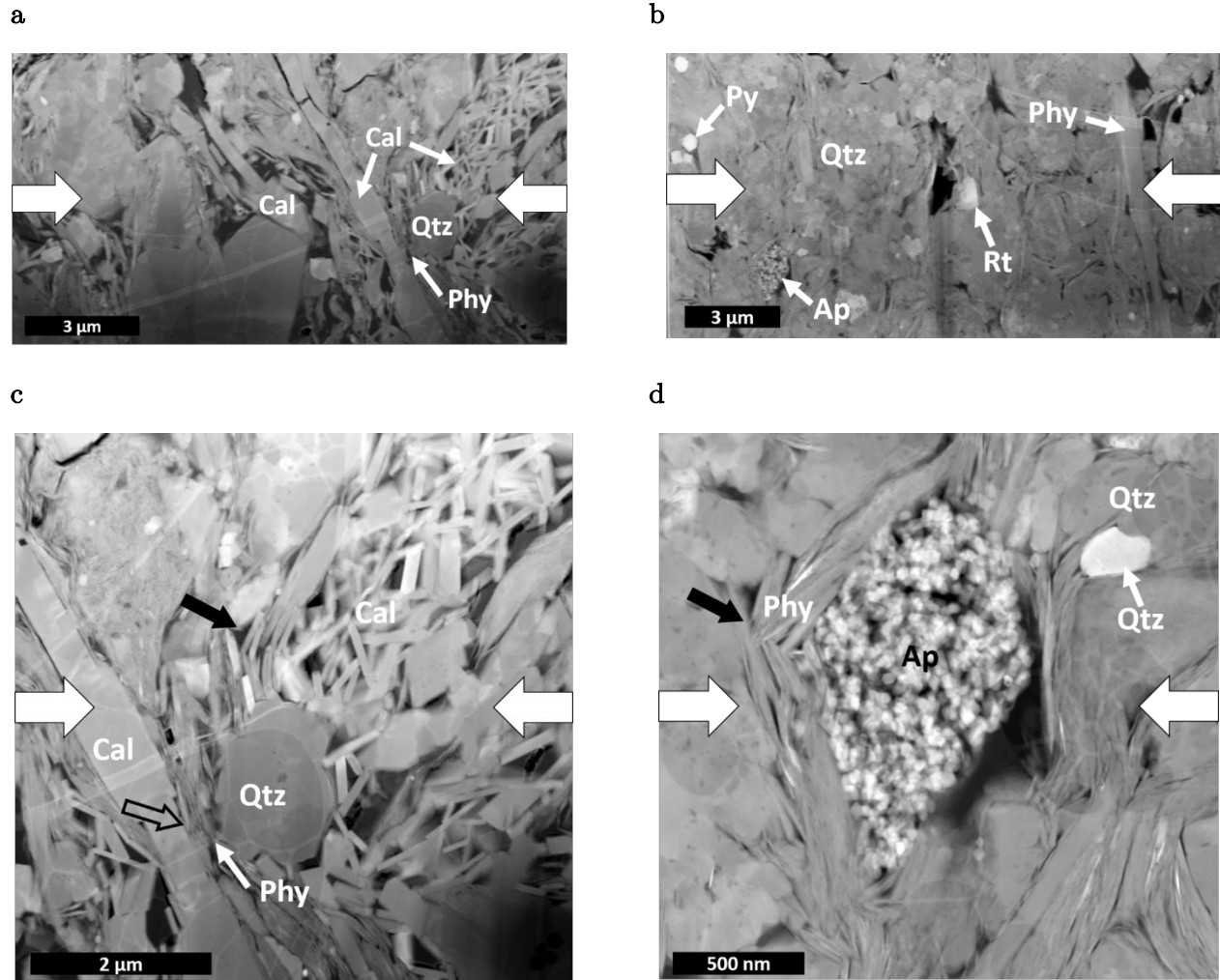
Figure 6 High resolution TEM photographs of primary deformed (**a, c**) low porous Posidonia (HAR38) and (**b, d**) porous Bowland (BOS16) shale. Deformation conditions are p_c = 75 MPa, T = 90 °C, σ (HAR38) = 160 MPa and σ (BOS16) = 209 MPa. Almost no brittle deformation is visible in images (**a, b**). Deformed Posidonia (HAR) shale shows pore space reduction between calcite flakes (**c**, bold black arrow) and bending of phyllosilicates around stronger quartz grains (**c**, open white arrow). For Bowland (OC) shale, transient creep is mainly accommodated by bending of weak phyllosilicates around stronger grains, e.g., apatite (**d**, bold black arrow). Loading direction is perpendicular to bedding orientation and indicated by bold white arrows. For mineral abbreviations see **Fig. 5**. Rt is rutile.

In summary, our microstructure observations on deformed Posidonia and Bowland shale samples indicate that a range of deformation mechanisms operate including plastic dislocation and diffusion activities and brittle microcracking. However, it is not possible to infer how the respective contributions of the different mechanisms depend on the prevailing conditions.

6 Discussion

The time-dependent deformation (creep) behavior and deformation mechanisms of the investigated shale rocks strongly depend on sample mineralogy and experimental conditions such as confining pressure, temperature and stress, as recognized also for other shales (Sone and Zoback 2013b, 2014; Rybacki et al. 2017). Here, we discuss the influence of these parameters on the creep behavior of Posidonia (HAR) and Bowland (OC) shale and compare the results to literature data that was obtained on other European and North American shale rocks (Sone and Zoback 2014; Rybacki et al. 2017).

6.1 Deformation Mechanisms

Black shales are usually highly anisotropic and deform by a combination of brittle and ductile mechanisms since they consist of many different phases with different strength. Therefore, it is difficult to establish a constitutive equation that describes the macroscopic mechanical behavior based on microphysical deformation mechanisms. Commonly, the total axial strain is described by adding the elastic and inelastic strain components in each of the three different creep regimes separately (Gao et al. 2010; Brantut et al. 2012, 2013, 2014; Dewers et al. 2017). This approach was successfully applied to monophase materials (e.g., metals, (Chindam et al. 2013)) and may serve as a first approach also to describe the mechanical response of polyphase shale rocks, although the semibrittle deformation behavior of shales suggests that several mechanisms operate in parallel, probably with a dominant process acting in each regime.

Depending on the applied deformation conditions (p_c, T, σ) and composition of the investigated shale rocks, we either observed only primary creep (group 1) or primary and subsequently secondary and finally tertiary creep (group 2) (cf., **Figs. 3, 4**). It is conceivable that different deformation mechanisms may have been active in the samples, such as plastic dislocation activity and brittle micro cracking. By definition, primary creep occurs at continuously decreasing axial creep strain rate, $\dot{\varepsilon}_{creep}$, whereas secondary and tertiary creep are characterized by a constant (minimum), $\dot{\varepsilon}_{min}$, and increasing strain rate, respectively (e.g., Brantut et al. 2014; Rybacki et al.

2017). To distinguish samples belonging to group *1 or group* 2, we calculated for every single experiment strain rate as a function of time. One example is given in **Fig. 7**, showing the change of strain rate with time for the two Posidonia (HAR) and Bowland (OC) samples (HAR43 and BOS16) plotted in **Fig. 3b**. Obviously, the quartz-rich Bowland shale (BOS_OC - Qtz) deformed solely by primary creep (group 1), displaying a continuously decreasing strain rate over time with progressive hardening. In contrast, the weak Posidonia shale (POS_HAR-Cly) exhibits first a decrease of strain rate with time, but subsequently an increase after passing a minimum value, which is characteristic for the three creep phases of primary, secondary and tertiary creep (group 2). For samples of group 2 we determined the minimum strain rate (**Tab. 2**).
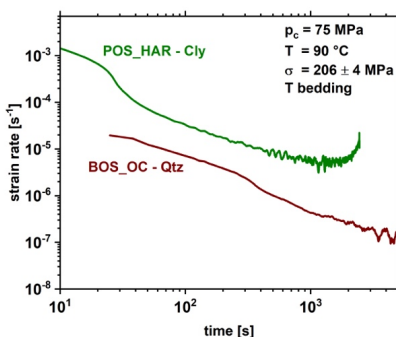

Figure 7 Strain rate versus time curves of Posidonia (POS_HAR - Cly) and Bowland (BOS_OC - Qtz) shale, deformed at 75 MPa confining pressure, 90 °C temperature and 206 ± 4 MPa stress (cf., **Fig. 3b**) in double-logarithmic scale. Sample BOS_OC - Qtz deformed by primary creep, indicated by a continuously decreasing strain rate with increasing time. The Posidonia (HAR) shale sample shows in addition a secondary and tertiary creep phase, for which the strain rate reaches minimum value (secondary creep) before it increased with time (tertiary creep). Note that the strain rate data are smoothed because of numerical noise.

Our microstructural observations of deformed Posidonia (HAR) and Bowland (OC) shales suggest that primary creep is mainly accommodated by deformation (e.g., bending) of weak material (**Figs. 5f, 6b, d**), and partly by local pore space reduction (**Fig. 6c**). We assume that plastic flow of organic matter and shearing of clay flakes as well as intracrystalline dislocation glide in phyllosilicates contributes to viscous creep. This may be combined with subcritical crack growth via chemical reactions (stress corrosion) during the secondary creep regime (Rybacki et al. 2017). Samples exhibiting tertiary creep show strongly localized deformation close to a macroscopic shear

fracture. Here, deformation is mainly assisted by inter- and intracrystalline microcracking as well as crack coalescence.

Empirical models in the form of parabolic, exponential, logarithmic or hyperbolic dependence of strain on time have frequently been used to describe the decelerating creep phase (group 1) of rocks, soils and metals (Gupta 1975; Findley et al. 1976; Karato 2008; Paterson 2013). If the strain depends linearly on stress, e.g., in many cases for small stress levels, linear viscoelastic models can be used to describe the (primary) creep of a polyphase material (Sone and Zoback 2013b, 2014). The basic elements of linear viscoelastic models (elastic spring and viscous dashpot, each of them representing the endmember phenomenon of elastic and viscous properties of a specific mineral) may be combined to describe the constitutive behavior of the rock (Li and Ghassemi 2012; Almasoodi et al. 2014). However, this requires the knowledge of the elastic and viscous properties of each phase under the applied deformation (p_c, T, σ) conditions, that are typically not available. In addition, these models cannot capture the volumetric and spatial distribution of the different phases, as well as possible brittle fracturing of some constituents. For stress corrosion, Brantut et al. (2013) recently suggested a model using an exponential law to approximate crack-damage related primary creep of rocks.

The secondary creep of rocks (group 2) at high confining pressure and temperature has been characterized by quasi-constant strain rate over time (balance between the rate of strain hardening and softening), where deformation may be accommodated by dislocation and diffusion activity or other ductile processes, which is commonly described by flow models based on a power law (Evans and Kohlstedt 1995; Bieniawski 2008; Dorner et al. 2014; Rybacki et al. 2017). Brantut et al. (2012) and Heap et al. (2009) established a similar power law creep relation between strain rate, stress and confining pressure in the secondary creep regime. Here, it is assumed that the dominating deformation mechanism is subcritical microcrack growth (stress corrosion). The crack velocity of this thermally activated mechanism depends on several factors such as temperature, humidity or stress intensity factor at the crack tip (Kranz 1980; Kranz et al. 1982; Atkinson 1987; Ciccotti 2009; Heap et al. 2009). Although our samples were dried at 50 °C for at least 48 h, fluids may remain within unconnected pores, potentially leading to time-dependent creep strain and

static fatigue of the investigated samples due to subcritical crack growth by stress corrosion (Brantut et al. 2012; Brantut et al. 2014).

Unfortunately, the Paterson deformation apparatus does not allow measurement of the load-normal lateral strain, and thus the volumetric strain, which would allow to detect microcrack activity. Instead, we measured the porosity of samples before and after deformation. **Fig. 8** shows the calculated porosity reduction, $\phi_{\text{reduction}} = \phi_{\text{prior deformation}} - \phi_{\text{after deformation}}$, where $\phi_{\text{reduction}} > 0$ represents pore space reduction due to sample deformation and vice versa. For primary creep, **Fig. 8** suggests that an increase in confining pressure yields porosity reduction, while increasing stress leads to porosity increase, likely by microcrack evolution. Posidonia (HAR) (**Figs. 8a, c, e**) as well as Bowland (OC) shale (**Figs. 8b, d, f**) specimens belonging to group 2 (post primary creep) exhibit the largest porosity increase after sample deformation, independent of applied confining pressure (**Figs. 8a, b**), temperature (**Figs. 8c, d**) and stress (**10e, f**). An increasing $\phi_{\text{reduction}}$ with increasing confining pressure may be explained by Goetze's criterion, which suggests that dilatancy and microcrack formation may occur as long as $\sigma > p_c$ (Evans and Kohlstedt 1995). These observations suggest that group 2 samples may have accommodated part of the deformation by subcritical crack growth due to stress corrosion. For porous sandstone deformed at room temperature, Heap et al. (2009) suggested the onset of dilatancy already at stresses of about $80 - 90\,\%$ of the triaxial compressive strength also leading to secondary and eventually tertiary creep. Since the applied stresses in this study are close to the short-term triaxial compressive strength obtained under similar p_c, T - conditions (Herrmann et al. 2018), we expect at least a partial contribution of this mechanism to the creep of our investigated samples.
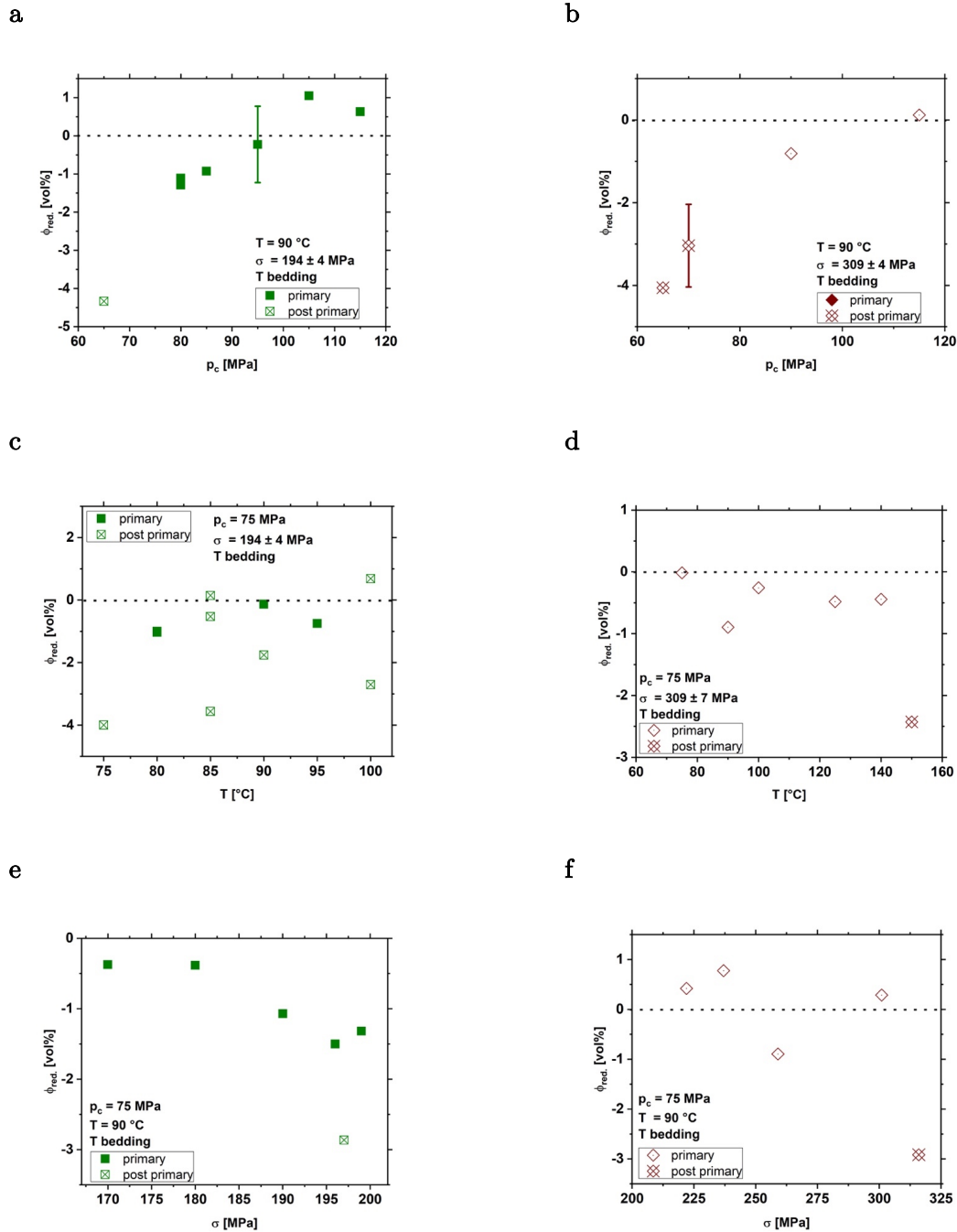
Figure 8 Reduction in sample porosity of Posidonia (HAR) (**a, c, e**) and Bowland (OC) shale (**b, d, f**), $\phi_{\text{reduction}} = \phi_{\text{prior deformation}} - \phi_{\text{after deformation}}$ depending on p_c (**a, b**), T (**c, d**) and σ (**e, f**). $\phi_{\text{reduction}} > 0$ represents pore space reduction, whereas $\phi_{\text{reduction}} < 0$ displays increasing porosity due to deformation. Primary = samples exhibiting only primary creep behavior, post primary = samples exhibiting in addition to primary also secondary and partly tertiary creep behavior. Deformation conditions are indicated.

Alternatively, secondary creep can be regarded as a (long-lasting) transient creep phenomenon at minimum strain rate, where the deformation mechanisms, which are responsible for primary and tertiary creep balance by recovery or recrystallization over a certain period (Zener and Hollomon 1946). Brantut et al. (2013) also noted that creep driven by irreversible crack growth is not a steady-state process and may be more likely an inflexion between the primary and tertiary creep phase, which exhibits a specific minimum creep strain rate.

The following discussion will focus on the influence of composition and boundary conditions (σ, T, p_c) on the primary creep phase of shale rocks since most of the deformed shale specimens exhibited this creep behavior. An attempt to quantify the influence of σ, T and p_c on the secondary creep phase of the investigated shales is given in the appendix, revealing large uncertainties of the calculated parameters.

6.2 Effect of confining pressure, temperature and stress on primary creep of shale rocks

To discuss the influence of confining pressure, temperature and stress on the primary creep phase of Posidonia (HAR) and Bowland (OC) shales, we use a simple phenomenological power law approach:

$$\varepsilon_t = \varepsilon_{el} + \varepsilon_{inel} = \frac{\sigma}{E} + a * t^b \tag{1}$$

where: ε_t = total axial strain, ε_{el} = elastic axial strain, ε_{inel} = inelastic axial strain, σ = axial differential stress, E = static Young's modulus, t = experimental time and 'a' and 'b' are constants.

As suggested by Rybacki et al. (2017), the following empirical correlations were used to account for the influence of p_c, T and σ on the constants 'a' and 'b' used in **Eq. 1**:

$$a = a_0 * \sigma^{n_a} * e^{-\left(\frac{Q_a + p_c * V_a}{R * T_{abs}}\right)} \tag{2}$$

$$b = b_0 * \sigma^{n_b} * e^{-\left(\frac{Q_b + p_c * V_b}{R * T_{abs}}\right)} \tag{3}$$

yielding:

$$\varepsilon_t = \frac{\sigma}{E} + \left(a_0 * \sigma^{n_a} * e^{-\left(\frac{Q_a + p_c * V_a}{R * T_{abs}}\right)}\right) * t^{\left(b_0 * \sigma^{n_b} * e^{-\left(\frac{Q_b + p_c * V_b}{R * T_{abs}}\right)}\right)} \tag{4}$$

where: a_0 and b_0 are rock constants, $n_{a, b}$ = stress exponent, $Q_{a, b}$ = activation energy, $V_{a, b}$ = activation volume, R = molar gas constant and T_{abs} = absolute temperature. This approach was adopted from constitutive equations describing high temperature creep of rocks, where the stress dependence is expressed by the stress exponent, the temperature sensitivity by the activation energy and the confining pressure dependence by the activation volume. Note, however, that these correlations are empirical and do not claim to correctly express the underlying microphysical processes assumed here such as dislocation glide and bending and shearing of phyllosilicates, compaction or granular flow.

The amount of elastic strain in **Eq. 1** may be determined by calculating the ratio of applied stress and static Young's modulus. We used Young's modulus data from constant strain rate experiments previously performed on similar shale samples at similar p_c, T - conditions (Herrmann et al. 2018). Since the authors measured no confining pressure or temperature dependence of E, we assume no significant change of elastic axial creep strain with varying p_c, T - conditions in our experiments.

The inelastic axial creep strain of each experiment was calculated by subtracting the elastic strain from the total measured axial creep strain. Plotting the inelastic axial creep strain versus time and fitting the curve by non-linear regression yields the constants 'a' and 'b' for each experiment. The parameter 'a' varies between 0.0011 and 0.00639 s^{-b} and 'b' between 0.03839 and 0.26815 (**Tab. 2**).

We also determined the parameters 'a' and 'b' of group 2 samples by fitting only the primary part of creep curves, which results in substantially higher values compared to those obtained for group 1 samples. This indicates a difference in the relative contribution of the present deformation mechanisms, which act in the primary creep regime of both sample groups. Therefore, the approach given in **Eq. 1** may not fully represent the time dependent deformation behavior of shale rocks under all p_c, T, σ - conditions, especially with respect to proppant embedment, where high stresses due to low contact areas between proppant agent and fracture surface ae expected. However, since the lifetime of stimulated wells is typically only a couple of years, we assume that this approach is still useful to discuss the potential of a shale play for the economical extraction of hydrocarbons.

Taking the logarithm of **Eqs. 2** and **3** yields the following correlations:

$$\log(a) = \log(a_0) + n_a * \log(\sigma) - \frac{Q_a * \log(e)}{R * T_{abs}} - \frac{V_a * p_c * \log(e)}{R * T_{abs}} \tag{5}$$

$$\log(b) = \log(b_0) + n_b * \log(\sigma) - \frac{Q_b * \log(e)}{R * T_{abs}} - \frac{V_b * p_c * \log(e)}{R * T_{abs}} \tag{6}$$

which were used to determine the sensitivity of 'a' and 'b' to a change of p_c, T and σ. The corresponding plots to determine the parameters n, Q and V for Posidonia (HAR) and Bowland (OC) shales are given in **Fig. 9**. In each figure two of the three deformation conditions (p_c, T, σ) are fixed to determine the sensitivity of parameters 'a' and 'b' on the remaining one. Linear

regression fits for the parameters are shown by dashed lines in **Fig. 9** and summarized in **Tab. 3**, including the calculated constants a_0 and b_0. They are discussed separately in the following three sections.

Table 3 Parameters accounting for influence of confining pressure, temperature and stress on primary and secondary creep of Posidonia (HAR) and Bowland (OC) shale.

Parameter	Posidonia shale (HAR)		Bowland shale (OC)	
	Primary creep	Secondary creep	Primary creep	Secondary creep
n_a	5.39 ± 4.16	/	1.87 ± 0.75	/
n_b	$\equiv 0$	/	$\equiv 0$	/
α	/	$\equiv 0.16$	/	$\equiv 0.57$
Q_a	14.39 ± 8.49 kJ/mol	/	13.12 ± 1.55 kJ/mol	/
Q_b	$\equiv 0$	/	$\equiv 0$	/
Q_c	/	$\equiv 98$ kJ/mol	/	$\equiv 140$ kJ/mol
V_a	$\equiv 0$	/	$\equiv 0$	/
V_b	31.36 ± 6.51 cm³/mol	/	11.97 ± 10.96 cm³/mol	/
V_c	/	76.44 ± 696.35 cm³/mol	/	187.13 ± 1466.24 cm³/mol
a_0	$(2.11 \pm 0.71) * 10^{-13}$ MPa$^{-5.39}$ s^{-b}	/	$(6.63 \pm 1.44) * 10^{-6}$ MPa$^{-1.87}$ s^{-b}	/
b_0	0.4 ± 0.07	/	0.12 ± 0.02	/
$\log(c_0)$	/	$- 3.81 \pm 7.49 \log(e^{-0.16\text{MPa}} * s^{-1})$	/	$- 60.87 \pm 14.55 \log(e^{-0.57\text{MPa}} * s^{-1})$

The constitutive equation suggested here to express the stress, - temperature and confining pressure dependence of primary creep of shale rocks is phenomenological. However, one may argue that the stress and temperature sensitive creep parameter 'a' we obtained suggest that mainly viscous mechanisms are described by this creep parameter, since these mechanisms are known to be stress and temperature sensitive (Sherby et al. 1999; Hobbs and Ord 2015). In contrast, brittle processes may be connected to the power law exponent 'b', since this latter is strongly influenced by confining pressure (Hobbs and Ord 2015).

6.2.1 Effect of axial stress

The effect of stress on the primary creep behavior of Posidonia (HAR) and Bowland (OC) shale is expressed by the stress sensitivity n_a and n_b of the power law creep parameters 'a' and 'b', respectively. The stress exponent $n_a = 5.4$ of weak Posidonia (POS_HAR) shale is almost three times higher than $n_a = 1.9$ of quartz-rich (outcrop) Bowland (BOS_OC) shale (**Fig. 9a**). Both values are distinctly higher than $n_a = 1$, which is expected if the rocks would deform in a linear viscous manner. This non-linear viscous behavior may be caused by a range of mechanisms including dislocation glide or cracking. As the applied stresses of 160 – 316 MPa are close to the triaxial compressive strength (Herrmann et al. 2018), we suggest that the generation of cracks and their interaction may also play a role at these conditions.

Comparable results for Posidonia (DOT) shale ($n_a = 1.4$), deformed at similar confining pressures and temperatures, were found by Rybacki et al. (2017). Also, Marcellus shale deformed at $p_c = 19$ MPa, T = 20 °C and σ < 90 MPa exhibited non-Newtonian primary creep (Li and Ghassemi 2012). In contrast, other North American and Canadian shales such as Eagle Ford, Barnett, Haynesville and Fort St. John were found to deform linear viscously (Li and Ghassemi 2012; Sone and Zoback 2013, 2014; Almasoodi et al. 2014; Rassouli and Zoback 2015). Note that in the latter studies creep experiments were performed at low stresses (σ < 90 MPa, mostly < 45 MPa) and confining pressures (p_c < 60 MPa), which are substantially lower than the applied stresses and resulting strains in our study. Also, experiments reported in the literature were performed at ambient temperature only. Therefore, the expected deformation mechanisms are likely different for shales deformed at low and high stresses and temperatures, respectively. At lower stress conditions the strain may be accommodated mainly by closing of preexisting micro cracks and pores, whereas at high stress the generation (and subcritical growth) of microcracks, grain boundary sliding and plastic deformation of weak mineral phases may have also operated.

As observed by Rybacki et al. (2017) on Posidonia (DOT) shale, the stress dependence of the power law exponent 'b' (**Eq. 6**), n_b, of Posidonia (HAR) as well as Bowland (OC) shale appears to be negligible (**Fig. 9b**).

A stepwise increasing stress irreversibly changes the microstructure of the samples within each single step, thereby affecting the deformation behavior of the subsequent creep steps (**Fig.2**). Since most published creep experiments on shales were performed stepwise, we assume that the experimental protocol also affected the stress sensitivity of the investigated rocks (Brantut et al. 2013).

6.2.2 Effect of temperature

With increasing temperature, we observed an increasing primary creep strain (cf. **Fig. 4c, d**). This may be due to the presence of weak phases with temperature-sensitive flow strength, such as clays and organic matter (Mikhail and Guindy 1971). Least square fitting of the temperature sensitivity of the creep parameter 'a' yields similar apparent activation energies of $Q_a = 14 \pm 9$ kJ/mol for Posidonia (HAR) shales and $Q_a = 13 \pm 2$ kJ/mol for Bowland (OC) shale (**Fig. 9c**). Regarding parameter 'b', we obtain no clear correlation with temperature ($Q_b \equiv 0$ kJ/mol) for Posidonia (HAR) shale deformed at constant stress and confining pressure (**Fig. 9d**), suggesting minor temperature dependence. A best fit of the Bowland (OC) shale data (p_c, σ = const.) would give a negative activation energy of $Q_b \approx$ - 5 kJ/mol. Since this is counterintuitive, we also fixed Q_b (BOS_OC) $\equiv 0$ kJ/mol. This seems to be reasonable, since Bowland (OC) shale consists of $\approx$ 70 vol% quartz minerals, the strength of which is believed to be hardly sensitive to temperature changes in the investigated range, at least at relatively dry conditions.

The calculated activation energies for primary creep of Posidonia (HAR) and Bowland (OC) shales are in relatively good agreement with estimates of $Q_a \approx 3$ kJ/mol and $Q_b \approx 5$ kJ/mol of other Posidonia (DOT) shales deformed in the primary regime (Rybacki et al. 2017). These values are lower than activation energies for steady state creep of the weak phases ($\approx 50 - 150$ kJ/mol; cf., Rybacki et al. 2017; Herrmann et al. 2018) and for stress corrosion of sandstone and granite ($\approx 30 - 50$ kJ/mol; Brantut et al. 2012). The difference presumably results from the simultaneous operation of deformation mechanisms acting in the primary and secondary creep

regime and from the multiphase composition of the investigated shales. Our determined apparent activation energies represent a bulk temperature sensitivity of primary creep of the shale samples.

6.2.3 Effect of confining pressure

With increasing confining pressure, we observed reduction in total axial strain (rate) for Posidonia (HAR) and Bowland (OC) shale deformed in the primary regime (**Fig. 4a, b**), revealing material strengthening with increasing confining pressure, as expected for semibrittle deformation due to compaction of pores, closure of preexisting microcracks and enhanced friction between grains with increasing p_c. This observation is in line with an increasing triaxial compressive strength with increasing confining pressures at constant strain rate as observed by Herrmann et al. (2018) for the same types of shale rocks.

To empirically quantify the influence of confining pressure on the primary creep phase of Posidonia (HAR) and Bowland (OC) shales, we estimated an apparent activation volume, yielding V_b (POS_HAR) = 31±7 cm^3/mol and V_b (BOS_OC) = 12±11 cm^3/mol for the power law creep parameter 'b' (**Fig. 9f**). A higher value for Posidonia shale than for Bowland shale is likely related to the higher amount of weak sample constituents of Posidonia shale (**Tab. 1).** The power law parameter 'a' shows almost no pressure sensitivity and was therefore fixed to zero (V_a (POS_HAR) = V_a (BOS_OC) ≡ 0 cm^3/mol) (**Fig. 9e**), in agreement with results observed for Posidonia (DOT) shale (Rybacki et al. 2017). In contrast, Sone and Zoback (2013, 2014) found no significant influence of confining pressures on the primary creep behavior of Barnett, Eagle Ford, Fort St. John and Haynesville shale. The authors also observed linear viscoelastic creep for their investigated shales, indicating that pressure-sensitive brittle deformation mechanisms were likely not the dominant mechanisms accommodating creep in their experiments. The low pressure sensitivity may be explained by the relatively low confining pressures (p_c = 10 – 60 MPa) and stresses (σ = 3 – 45 MPa) used by Sone and Zoback (2013, 2014) which minimizes pore collapse and microcrack generation.
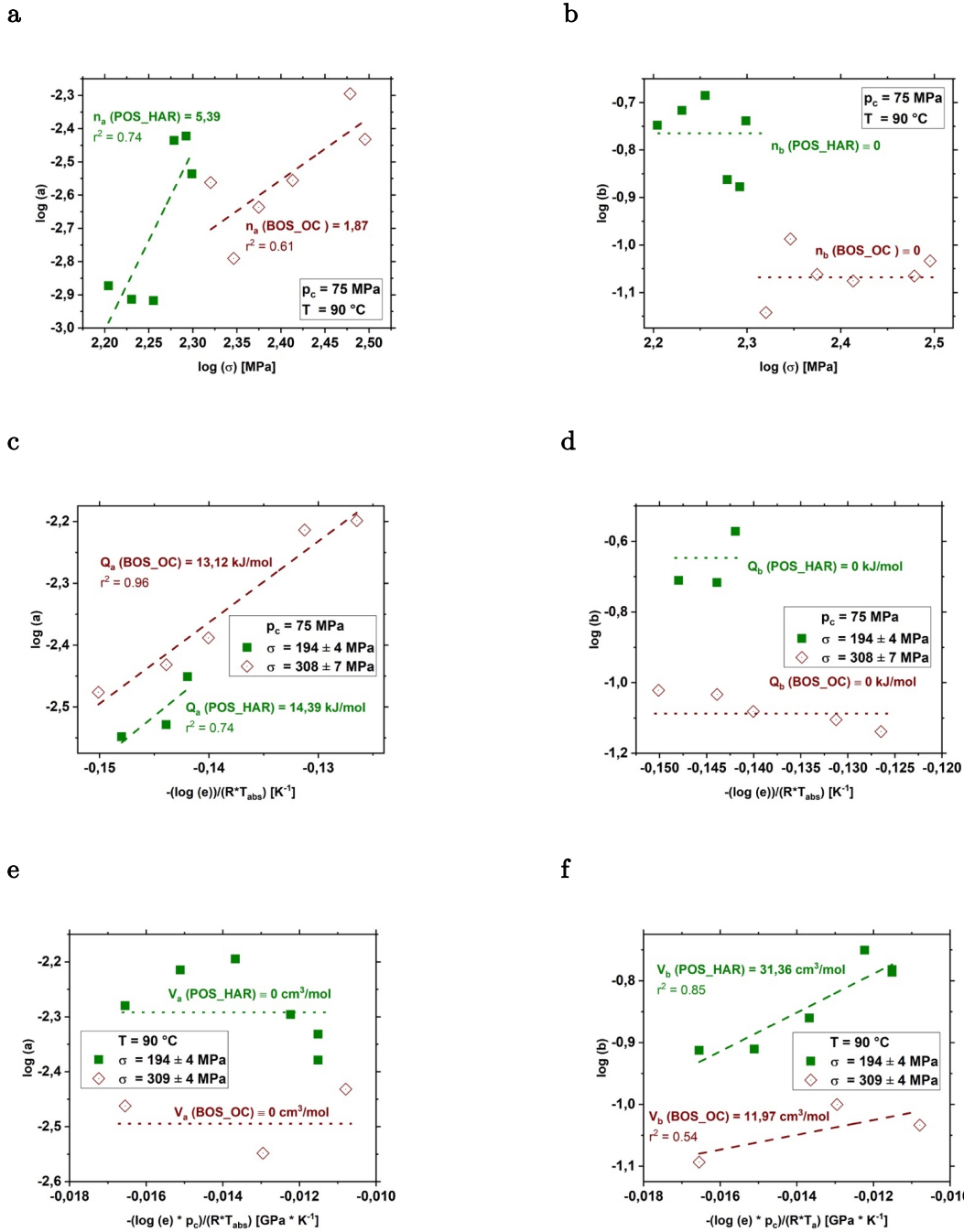
Figure 9 Influence of axial differential stress (**a, b**), temperature (**c, d**) and confining pressure (**e, f**) on power law creep parameter 'a' and 'b' used to describe inelastic strain during primary creep. Dashed lines show linear regression fits for stress sensitivity (n) (**a, b**), activation energy (Q) (**c, d**) and activation volume (V) (**e, f**). Dotted lines indicate no correlation. Subscripts a and b belong to power law creep parameter 'a' and 'b', respectively. Deformation conditions and the coefficient of determination (r^2) are indicated.

6.2.4 Effect of sample composition and mechanical properties

To investigate the influence of shale composition and their mechanical properties on the primary creep behavior of shale rocks, we estimated the total primary creep strain after three years deformation, during which most of the production decline in shale gas reservoirs occurs. For comparison with literature data on Posidonia (DOT) shale (Rybacki et al. 2017) as well as on Barnett, Haynesville and Eagleford shale (Sone and Zoback 2014), we used a modified form of **Eq. 1** by replacing the power law parameter 'a' by a = A $*\sigma^{n_a}$, yielding:

$$\varepsilon_t = \frac{\sigma}{E} + A * \sigma^{n_a} * t^b \tag{7}$$

For determination of ε_t after 3 years deformation, we recalculated the values A and b for deformation conditions of p_c = 20 MPa, T = 20 °C and σ = 25 MPa to allow for comparison with the experiments on N-American shales that were performed at low stresses and confining pressures and at ambient temperature. Results are given in **Tab. 4** together with the approximate composition and porosity. Note that Sone and Zoback (2014) and Rybacki et al. (2017) fitted measured creep curves of total axial strain, ε_t. Therefore, no elastic strain was added to the strain values determined from the literature. For comparison, we additionally calculated the elastic, ε_{el}, and inelastic strain values, ε_{inel} (**Tab. 4**), using the data provided by Sone and Zoback (2014).

Table 4 Calculated primary creep strains after 3 years

shale	Ref.	A [MPa^{-a}s^{-b}]	b	ε_t [%]	ε_{el} [%]	ε_{inel} [%]	QFP [vol%]	Cb [vol%]	Clay+TOC+Mica+ϕ [vol%]	ϕ [vol%]	σ_{TCS} [MPa]	E [GPa]
POS_HAR	*	5.63 * 10^{-16}	0.3092	0.28	0.27	0.01	17	39	45	3	165****	9****
BOS_OC	*	2.98 *10^{-8}	0.1087	0.19	0.18	0.01	69	7	24	8	284****	14****
POS_DOT	**	2 * 10^{-5}	0.05	0.41	0.31	0.10	14	42	43	11	175****	8****
BAR$_I$	***	3.85 * 10^{-5}	0.05	0.14	0.10	0.04	48	2	50	7	210	26
BAR$_{II}$	***	1.5 * 10^{-5}	0.019	0.05	0.04	0.01	42	48	10	2	325	67
HAY$_I$	***	6.3 * 10^{-5}	0.05	0.39	0.16	0.23	32	20	48	6	145	16
HAY$_{II}$	***	2.35 * 10^{-5}	0.0425	0.13	0.06	0.07	23	49	28	4	240	42
EAG$_I$	***	5.55 * 10^{-5}	0.0615	0.43	0.14	0.29	24	46	30	6	200	18
EAG$_{II}$	***	4.65 * 10^{-5}	0.052	0.30	0.12	0.18	14	66	20	6	175	22

Ref. = reference, A and b = power law parameter (cf., **Eq. 7**), ε_t = primary creep strain after 3 years at σ = 25 MPa, p_c = 20 MPa and T = 20 °C, QFP = quartz + feldspar + pyrite, Cb = carbonates, TOC = total organic carbon, ϕ = porosity, σ_{TCS} = triaxial compressive strength, E = static Young's modulus obtained at elevated p_c and T, B = brittleness based on E, POS_HAR = Posidonia (Harderode), BOS_OC = Bowland (outcrop), POS_DOT = Posidonia (Dotternhausen), BAR = Barnett, HAY = Haynesville, EAG = Eagle Ford, * = this study. ** = Rybacki *et al.* 2017, *** = Sone and Zoback (2013, 2014), **** = Herrmann et al. (2018). Subscripts I and II indicate clay and organic-rich (I) and organic-poor (II) rocks, respectively.

119

The resulting total strains (in %) are shown in a tertiary diagram (**Fig. 10a**) to visualize the influence of sample mineralogy on the time-dependent creep behavior. As in **Fig. 1**, sample mineralogy is separated into strong (QFP), intermediate strong (Cb) and weak (Clay + TOC + Mica + ϕ) components. No correlation between ε_t and the amount of QFP, carbonates or weak phases is found (**Fig. 10a, Tab. 4**). There may be a negative correlation between ε_{inel} and QFP (cf., **Tab. 4**), if shale rocks are recovered from different formations, although an inverse trend was found for shale samples acquired from the same formation. However, it is important to recall, that the activated creep mechanisms of the various shales are probably different due to the different p_c, σ, T - conditions applied in the considered studies. Separating the influence of porosity on creep deformation also shows no trend (**Tab. 4**).
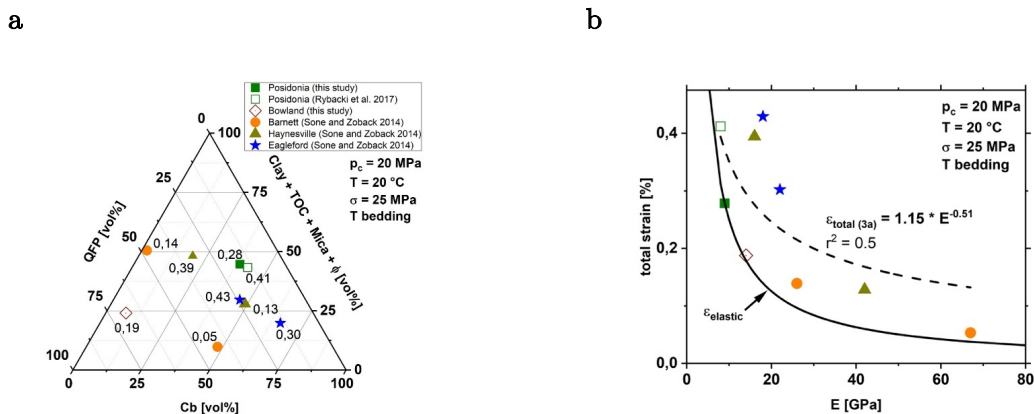

Figure 10 Calculated primary total strain (in %) after three years deformation at 20 MPa confining pressure, 20 °C temperature and 25 MPa stress versus composition (**a**) and static Young's modulus, E, (**b**). QFP = quartz + feldspar + pyrite, Cb = carbonates, TOC = total organic carbon, ϕ = porosity

The correlation between extrapolated total strain after 3 years deformation and the static Young's modulus (Herrmann et al. 2018; Sone and Zoback 2013, 2014) is shown in **Fig. 10b**. Note that E of Posidonia and Bowland shale was determined at different confining pressure (p_c = 50 MPa) and temperature (T = 100 °C), but the influence of p_c and T on E was found to be minor (Herrmann et al. 2018). The axial total strain decreases with increasing static Young's moduli (**Fig. 10b**) and

may be calculated using the correlation given in the figure (dashed line). Note that the correlation found in **Fig. 10b** is strongly influenced by the elastic strain (black line in **Fig. 10b**). Considering only the inelastic strain would yield a less pronounced trend (cf., **Tab. 4**). However, since the Young's modulus can be easily measured by wireline logs, this correlation may be especially interesting for practical purposes to estimate the long-term creep behavior of shale rocks. Note that this correlation is only applicable at shallow depth level and will change at greater depth with high pressure and temperature.

Total strains are also decreasing for strong samples with high triaxial compressive strength, σ_{TCS} (**Tab. 4**). This is in line with the positive correlation between σ_{TCS} and E of shale rocks (Herrmann et al. 2018).

The brittleness, B, of rocks is often quoted to represent an important parameter that allows to discriminate between prospective and non-prospective shales (Guo et al. 2013; Lora et al. 2016; Shah et al. 2017). It is a purely empirical rock parameter, which can be calculated based on several different definitions (e.g., Rybacki et al. 2016). Typically, B is normalized to a range between 0 and 1, where B = 0 and B = 1 represent ductile and brittle deformation, respectively. Since there is a strong correlation between E and the primary total strain after three years, we suggest to calculate the brittleness based on E to estimate the long-term creep behavior of shale rocks from short-term experiments. Since no correlation between primary total strain and composition was evident, brittleness based on shale composition (Rybacki et al. 2016) may not be used to estimate total strain values after three years. As pointed out by Rybacki et al. (2016) the definition of B based on E may adequately describe the mechanical behavior of shales in terms in brittleness, if the p_c, T - conditions do not exceed those expected at about 3 km depth.

In addition to the previously mentioned parameters (composition, E, σ_{TCS}, B), the angle between the maximum principal stress orientation and bedding orientation will also influence the primary creep strain due to the anisotropic character of shale rocks (Swan et al. 1989; Lora et al. 2016). If loaded parallel instead of perpendicular to bedding, samples would creep at slower rate yielding less creep strain after three years deformation (cf., Sone and Zoback 2014). Also, the

degree of anisotropy plays an important role in the deformation behavior of shale rocks, since bedding perpendicular and bedding parallel loading represent only endmembers, whereas in nature an intermediate state (of a loadbearing framework of hard mineral phases or interconnected weak layers) is more likely, as pointed out by Sone and Zoback (2013b).

The presence of water within samples also affects the creep behavior of shales in a way that creep is enhanced for samples with higher water content as shown for Haynesville shale by Sone and Zoback (2014) and Alum shale by Rybacki et al. (2017). This is presumably due to swelling of clay minerals or microcrack growth due to stress corrosion at higher stresses.

6.2.5 Rheological models

In addition to the empirical approach given in section 5.2 to characterize the primary creep behavior of shale rocks, we also tried to apply a linear viscoelastic model to fit the recorded primary creep data of shales, as has been suggested recently (Li and Ghassemi 2012 and Almasoodi et al. 2014). These models typically consist of a combination of rheological bodies such as springs (elastic) and dashpots (viscous). Note that these models ignore effects of changing confining pressure and temperature. Also, the models assume a linear correlation between strain and applied stress (n = 1), which was found to be different for the investigated shale rocks of these study. Irrespective of these limitations, we fitted a Zener-model in series with a Kelvin-Voigt model, as proposed by Almasoodi et al. (2014), to our recorded primary creep curves using the following equation:

$$\varepsilon_t = \frac{\sigma}{E} + \frac{\sigma}{E_1}\left(1 - e^{\frac{-E_1 * t}{\mu_1}}\right) + \frac{\sigma}{E_2}\left(1 - e^{\frac{-E_2 * t}{\mu_2}}\right) \qquad (8)$$

where µ = viscosity and subscripts 1 and 2 represent different sample constituents. This model was chosen since it is in good agreement with the approach of separating shale composition into weak (cly, TOC, ϕ) and strong (QFP, Cb, Mca) components, as suggested by Herrmann et al.

(2018) for the same shale rocks samples. Mca and Cb are regarded as strong mineral phases here, since they display relatively large Young's moduli (Mavko et al. 2009). Strong and weak components are represented by subscripts 1 and 2, respectively. Fitting this model to the recorded creep curves, using the non-linear Levenberg-Marquardt algorithm yielded strongly unstable results for Young's moduli and viscosities both for Posidonia and Bowland shale. Therefore, the use of such models based on springs and dashpots to characterize the time dependent primary creep behavior of shale rocks may only be feasible at low stresses in the Newtonian viscous regime. For non-linear viscous creep or if brittle mechanisms such as the initiation and coalescence of microcracks contribute to the overall deformation, these models may not be appropriate.

6.2.6 Correlation between primary creep and constant strain rate behavior

A theoretical approach to link results obtained from constant strain rate and creep experiments in the primary regime performed at low temperature (T < 0.3 T_m, where T_m is melting temperature) was suggested by Kassner and Smith (2014) for deformed Titanium alloy. The approach is based on a mechanical equation of state as reported by e.g., Zener and Hollomon (1946); Hollomon (1947) and Hart (1970). For materials showing strain hardening during constant strain rate deformation (up to peak stress), the authors propose that the strain-dependent stress can be described by:

$$\sigma = K * \varepsilon_{inel}^{o} * \dot{\varepsilon}_{0}^{p} \tag{9}$$

where K = strength parameter, ε_{inel} = inelastic axial strain, o = strain hardening exponent, $\dot{\varepsilon}_0$ = applied constant strain rate and p = strain rate sensitivity. Here, we set p ≡ 0.01, since the influence of applied strain rate on the resulting stress is minor (Herrmann et al. 2018). The strain hardening exponent, o, can be easily determined by calculating the slope of the log (σ)-log (ε_{inel}) plot recorded from a constant strain rate test. For Posidonia (HAR) shale deformed at p_c = 100 MPa, T = 100 °C and $\dot{\varepsilon}_0$ = 5 * 10^{-4} s^{-1} and Bowland (OC) shale deformed at p_c = 75 MPa, T

$= 100$ °C and $\dot{\varepsilon}_0 = 5 * 10^{-4}$ s^{-1} (Herrmann et al. 2018), we calculated o$_{(POS\_HAR)} = 0.063 \pm 0.001$ and o$_{(BOS\_OC)} = 0.048 \pm 0.001$, respectively. Neeraj et al. (2000) suggested a decreasing creep strain with a decreasing strain hardening exponent, which is in line with our observations (**Fig. 3b**). Nonlinear least square fitting of **Eq. 9** to stress-inelastic axial strain curves recorded during constant strain rate deformation results in K (POS_HAR) $= 314 \pm 1$ MPas and K (BOS_OC) $= 462 \pm 2$ MPas.

Rearranging **Eq. 9** and replacing $\dot{\varepsilon}_0$ by $\frac{\delta \varepsilon_{inel}}{\delta t}$ yields:

$$\varepsilon_{inel}^{\frac{o}{p}} * \delta\varepsilon_{inel} = \left(\frac{\sigma}{K}\right)^{\frac{1}{p}} * \delta t \tag{10}$$

Integrating **Eq. 10** and assuming $\sigma = $ const. (creep experiment) results in the following equation:

$$\varepsilon_{inel} = \left(\frac{\sigma}{K}\right)^{\frac{1}{o+p}} * \left(\frac{o+p}{p}\right)^{\frac{p}{o+p}} * t^{\frac{p}{o+p}} \tag{11}$$

Eq. 11 and **Eq. 1** appear to be similar suggesting the following equations to derive the creep parameters, 'a' and 'b', from constant strain rate experiments:

$$a = \left(\frac{\sigma}{K}\right)^{\frac{1}{o+p}} * \left(\frac{o+p}{p}\right)^{\frac{p}{o+p}} \tag{12}$$

$$b = \frac{p}{o+p} \tag{13}$$

For Posidonia (HAR) shale, we selected sample HAR_33 for comparison, since the applied deformation conditions (p_c = 105 MPa, T = 90 °C, σ = 194 MPa) were close to the applied deformation conditions of constant strain rate test (p_c = 100 MPa, T = 100 °C). For σ = 194 MPa, we obtained $a_{(POS\_HAR)}$ = (1.92 ± 0.08) * 10^{-3} and $b_{(POS\_HAR)}$ = 0.137 ± 0.002 from the performed constant strain rate test using **Eq. 11**. Extrapolated to strain achieved after three years deformation based on **Eq. 1** yields a total strain of ε_t = 0.045 ± 0.002. This value is somewhat lower than the total strain of ε_t = 0.08, extrapolated from the corresponding creep experiment.

For Bowland shale, sample BOS_26 was chosen (p_c = 75 MPa, T = 100 °C, σ = 314 MPa), for which we calculated the creep parameters $a_{(BOS\_OC)}$ = (1.74 ± 0.07) *10^{-3} and $b_{(BOS\_OC)}$ = 0.172 ± 0.003. Using these values, we obtain a total axial creep strain of ε_t = 0.064 ± 0.004 after three years deformation, which is relatively close to the extrapolated total strain of ε_t = 0.04 based on creep testing. The differences between extrapolated total axial strains from constant strain rate and constant stress tests may arise from slightly different deformation conditions or sample to sample variations. In addition, the approach is based on a mechanical equation of state, which assumes that the stress required for inelastic deformation depends only on the instantaneous values of strain, strain rate, temperature and confining pressure and not on the loading history, which is in contrast to our observations (**Fig. 2**). However, the obtained results suggest that quantitative estimates of the (long-term) creep strain of shale rocks from short-term constant strain rate experiments may be feasible, but only as a first order approximation.

7 Conclusions

Characteristic for semibrittle deformation, constant stress experiments performed on Posidonia (HAR) and Bowland (OC) shale reveal that the time dependent creep behavior of shale rocks is influenced by confining pressure, temperature and applied stress under the tested conditions. At high stress and temperature and at low confinement samples displayed in addition to primary creep also secondary and tertiary creep until sample failure. Primary creep strain is mainly accommodated by deformation of weak sample constituents (clays, TOC, mica) and local pore

space reduction. At the onset of tertiary creep, samples displayed localized deformation by formation of a single macrocrack, which is composed of coalesced subparallel microcracks for Bowland (OC) shale. Even in these high stress samples, the dislocation activity in quartz and carbonates is poor.

The effect of deformation conditions on the creep behavior is more pronounced for weak Posidonia (HAR) shale than for strong Bowland (OC) shale. Empirical power law correlations are applicable to account for the influence of stress, confining pressure and temperature on the primary creep phase of shale rocks.

The influence of sample composition on the general creep behavior is in the same order of magnitude as the effect of applied deformation conditions. A negative correlation between primary creep strain and sample strength and static Young's modulus is evident. These results are useful to assess the potential of a reservoir for an economical and sustainable extraction of hydrocarbons, since the Young's modulus can be easily and quickly estimated from wireline logs.

A correlation between the primary creep and constant strain rate behavior of shale rocks was found to some extent, if calculations are based on a mechanical equation of state.

This may be useful to estimate the long-term creep behavior of shale rocks from their short-term properties.

With respect to proppant embedment, our results predict a lower fracture closure rate of strong Upper Bowland (OC) shales compared to weak Posidonia (HAR) shale However, a decreasing fracture conductivity due to fines production as a result of proppant cracking is more likely in Bowland shale than in Posidonia shale reservoirs. To test this hypothesis, proppant embedment tests at elevated confining pressure and temperature are required.

Appendix

Influence of stress, temperature and confining pressure on secondary creep

Based on the assumption that dislocation glide in clay minerals is the main deformation mechanism (Ibanez and Kronenberg 1993), the minimum axial creep strain rate, $\dot{\varepsilon}_{\min}$, of samples which displayed secondary creep may be described by an exponential law in the form of:

$$\dot{\varepsilon}_{min} = c_0 * e^{\alpha * \sigma} * e^{-\left(\frac{Q_c + p_c * V_c}{R * T_{abs}}\right)} \tag{A1}$$

where c_0 and α are constants. Taking the logarithm of **Eq. A1** yields:

$$\log(\dot{\varepsilon}_{min}) = \log(c_0) + \alpha * \sigma * \log(e) - \frac{Q_c * \log(e)}{R * T_{abs}} - \frac{p_c * V_c * \log(e)}{R * T_{abs}} \tag{A2}$$

Linear regression of data using **Eq. A2** yields negative α and V_c-values, which is opposite to our experimental findings. This is probably due to a relatively small data base and large scatter. Therefore, we used values of $\alpha = 0.16$, $Q_c = 98 \pm 108$ kJ/mol and $\alpha = 0.57$, $Q_c = 140 \pm 120$ kJ/mol for Posidonia (HAR) and Bowland (OC) shale, respectively, which was previously determined from constant strain rate test (Herrmann et al. 2018). Using these values for multilinear regression yields log (c_0) = -3.81 ±7.49 e[-0.16MPa]s[-1], V_c = 76 ± 696 cm³/mol for Posidonia (HAR) shale and log (c_0) = -60.87 ±14.55 e[-0.57MPa]s[-1], V_c = 187 ± 1466 cm³/mol for Bowland (OC) shale (**Tab. 3**). These activation volumes are considerably higher than those determined for primary creep. The large uncertainties suggest that the characterization of secondary creep behavior of shale rocks based on dislocation glide in clay minerals as main deformation mechanism may not cover all present mechanisms during deformation, which is also in line with our observations that micro cracking contribute to deformation in the secondary creep phase (**Fig. 8**). Applying a power law approach

as suggested by Rybacki et al. (2017) also yielded negative Q_c and V_c values, which do not reflect the experimental observations.

Correlation between constant stress and constant strain rate

Under the assumption of brittle creep induced by subcritical crack growth due to stress corrosion, Brantut et al. (2014) suggested an empirical correlation between creep and constant strain rate deformation of sandstone based on a stress deficit, ΔQ, measured over a certain inelastic strain range (**Fig. A1a**). The authors performed constant strain rate as well as constant stress (creep) experiments at effective confining pressures of $p_{ceff} = p_c -$ pore pressure $= 10 - 40$ MPa and ambient temperature on three types of sandstones to investigate the relation between evolving creep strain rate, $\dot{\varepsilon}_{creep}$, and applied stress (in constant stress tests) and between measured evolving stress and applied constant strain rate, $\dot{\varepsilon}_0$, (in constant strain rate tests). Following Brantut et al. (2014), we plotted stress-inelastic axial strain curves recorded during the deformation of two Posidonia (HAR) shale samples, where one experiment was performed at constant strain rate (HAR sample taken from **Tab. 4** from Herrmann et al. (2018) and one at constant stress (sample HAR_43, this study) (**Fig. A1a**). Both experiments were conducted at 75 MPa confining pressure, but at slightly different temperatures (const. σ: T = 90 °C, const. $\dot{\varepsilon}$: T = 100 °C). Since during the 'constant stress test' only the applied load is constant, the real stress is slightly decreasing with increasing axial strain because of increasing sample diameter and assuming constant volume deformation. However, in the secondary creep regime, the applied stress was nearly constant ($\sigma = 202 \pm 2$ MPa) up to an inelastic axial strain of ≈ 0.032, followed by an abrupt decrease due to an enhanced creep strain rate close to sample failure. For the HAR sample, deformed at constant strain rate of $\dot{\varepsilon}_0 = 5 * 10^{-4}$ s^{-1}, the axial stress increases up to a peak value of ≈ 213 MPa at an inelastic axial strain of ≈ 0.023, after which it gradually decreased (**Fig. A1a**).
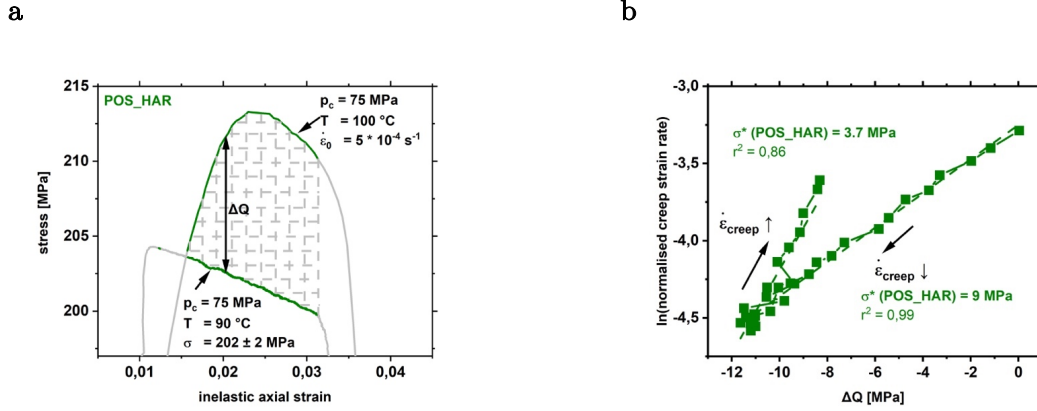
Figure A1 (a) Stress-inelastic axial strain curve of two Posidonia (HAR) samples deformed at either constant strain rate, $\dot{\varepsilon}_0$, or (quasi) constant stress, σ, recorded at slightly different temperatures. Due to the assumption of constant volume deformation (yielding an increasing sample diameter with increasing strain), σ of constant stress test is slightly decreasing, since a constant load was applied. Grey dashed area was used to calculate stress deficit, ΔQ. **(b)** ln of normalized creep strain rate versus stress deficit of the two Posidonia (HAR) samples shown in **(a)**. σ^* = activation stress. Deformation conditions are indicated.

In their experiments on sandstones, Brantut et al. (2014) observed that the two curves of samples deformed at constant strain rate and constant stress intersect twice, where after the second intersection the sample deformed at constant stress started to show accelerated creep strain rate (onset of tertiary creep phase). The area between the first and second intersection of stress curves recorded during deformation at constant stress and constant strain rate, represents the range, which was used by the authors (**Fig. 5** in Brantut et al. 2014) to calculate the stress deficit, ΔQ = $\sigma_{\text{creep test}} - \sigma_{\text{const. strain rate test}}$, for every single inelastic strain value. In our tests, the stress-inelastic axial strain curves did not intersect each other twice, since the sample deformed at constant stress failed earlier (**Fig. A1a**). This may be due to the slightly different temperatures since axial strain increases with increasing temperature (cf., **Figs. 4c, d**). Therefore, for calculation of ΔQ we used the area between the strain at the first intersection of recorded curves and the strain where tertiary creep started (dashed grey area in **Fig. A1a**).

Brantut et al. (2014) proposed the following correlation between creep strain rate, $\dot{\varepsilon}_{creep}$, at any given value of inelastic strain during constant stress deformation and ΔQ:

$$\frac{\dot{\varepsilon}_{creep}}{\dot{\varepsilon}_0} \approx e^{\frac{\Delta Q}{\sigma^*}} \tag{A3}$$

where $\dot{\varepsilon}_0$ = applied constant strain rate during constant strain rate test and σ^* = characteristic activation stress, which is a combination of parameters describing subcritical crack growth (Brantut et al. 2014).

Fig. A1b shows the natural logarithm of the creep strain rate normalized by the applied constant strain rate as function of ΔQ. In line with observations made by Brantut et al. (2014), the resulting curve has different slopes for the decreasing $\dot{\varepsilon}_{creep}$ ($\downarrow$) and the increasing $\dot{\varepsilon}_{creep}$ ($\uparrow$) with a minimum ΔQ at minimum $\dot{\varepsilon}_{creep}$. Fitting **Eq. A3** to Posidonia (HAR) shale data yielded $\sigma^* = 6.4 \pm 2.7$ MPa (**Fig. A1b**), which is larger than what was found for different sandstones ($\sigma^* = 1 - 2.7$ MPa) by Brantut *et al.* (2014). The contrasting results may originate from the different deformation conditions in our experiments and those performed by Brantut et al. (2014) and the different rock types. Also, during the deformation of Posidonia (HAR) shale other deformation mechanisms may be active but are not considered in the formalism above.

Interestingly, this approach was not applicable to Bowland (OC) shale, although it contains ≈ 70 vol% QFP and therefore should be better comparable to sandstones than Posidonia (HAR) shale. The applied constant stress, which is necessary to reach the secondary creep phase is slightly larger than the recorded stress during performed constant strain rate tests. This may be due to the relatively high applied constant strain rate, at which the shale sample cannot accommodate deformation over a certain time period, leading to lower strength due to increased pore pressures as a result of pore collapse as all experiments have been performed at undrained conditions. This may be more pronounced for porous Bowland (OC) than for low porous Posidonia (HAR) shale (**cf., Tab. 1**). Therefore, no ΔQ could be calculated.

However, the obtained results may be useful to subsequently assess specific rock properties of some shales, such as the stress intensity factor, time to failure as well as creep strain rates by only performing one constant stress and one constant strain rate test at the same p_c, T - conditions.

Chapter 5: General Conclusions

In this thesis, the short- as well as long term mechanical properties of shale rocks at simulated reservoir pressure, temperature and stress conditions were investigated. Sample material from European Posidonia shale (Germany) and Bowland shale (United Kingdom) was studied since these formations are considered to be prospective unconventional shale plays and therefore represent a potential target for the production of gas (Littke et al. 2011; Andrews 2013). The experimental investigations include the characterization of the petrophysical and geomechanical properties of the selected shales, such as composition, density, porosity and strength, Young's modulus and creep properties. The (peak) strength and Young's modulus were determined by performing a series of constant strain rate experiments. Furthermore, a series of constant stress deformation tests was conducted to characterize the time-dependent creep properties of these shale rocks. Most experiments were conducted at ambient and various enhanced confining pressure and temperature conditions. The microstructural analysis was largely based on scanning and transmission electron microscopy due to the fine grain size of the samples.

The triaxial compressive strength and static Young's modulus of the investigated shale rocks are strongly influenced by sample composition and are positively correlated to confining pressure conditions. Effects of varying temperature, strain rate and porosity on strength and Young's modulus are found to be minor. In general, the stress-strain curves recorded during constant strain rate deformation reveal dominantly a brittle to semibrittle deformation behavior at the imposed confining pressure and temperature conditions. Above $\approx 25-30$ vol% weak mineral phases (clay, mica, organic matter), the compressive strength and static Young's modulus decrease strongly with increasing amounts of weak sample constituents. This trend fits to predictions made by effective medium theories, where the experimental data plot mostly close to the lower (Reuss) bound. A comparable threshold value of ≈ 0.4 was found for the brittleness of these shales, calculated from their Young's modulus.

Indicative for semibrittle deformation, the creep behavior of Posidonia and Bowland shale at in situ deformation conditions is influenced by confining pressure, temperature and applied differential stress. The effect of these parameters was found to be more pronounced for weak Posidonia than for strong Bowland shale. At high stress and temperature and low confining pressure deformed shale rock material exhibits in addition to a decelerating (primary) creep phase also a quasi-steady state (secondary) and eventually an accelerating (tertiary) creep phase prior to sample failure. Most of the induced primary creep strain is accommodated by deformation of weak mineral phases and local pore space reduction. At the onset of the accelerating creep phase, deformation is mainly accommodated by the generation of microcracks, which form a single macrocrack at failure. Dislocation activity in carbonate and strong minerals is only minor. To account for the influence of the applied deformation conditions on the primary and secondary creep phase empirical power law equations were used, which allows extrapolating the laboratory results to longer durations that are relevant for a production decline in field operations. Fracture closure due to proppant embedment within a typical time period of about three years between new stimulation operations was to found to may occur only during the secondary creep phase presumably induced by local stress concentration (contact area between proppant agents and fracture surface). The influence of shale composition on the time dependent deformational behavior is in the same order of magnitude as the effect of applied deformation conditions. The amount of strong minerals, which may form a load bearing framework at high fraction, strongly influence the magnitude of creep strain of Posidonia shale from Southern Germany as reported in Chapter 3. Therefore, the long-term creep properties at low depth of this Posidonia shale may be correlated with composition-based brittleness index. A negative correlation between primary creep strain and sample strength and Young's modulus could be found for Posidonia and Bowland shale as shown in Chapter 4.

Assuming the indentation of strong proppant agents into the shale matrix as main mechanism for fracture closure, we suggest a substantially higher fracture closure rate of propped cracks within Posidonia shale than in Bowland shale. This is due to varying composition, strength, Young's modulus and creep properties of the different shale rocks. Semibrittle Posidonia shale,

which is rich in weak mineral phases such as clay, mica and organic material bents around stronger proppants whereas in brittle Bowland shale, which contains mainly quartz, an indentation of proppant agents may not occur due to the low strength contrast between proppants and shale matrix. On the other hand, for Bowland shale the high contact forces induce crushing of the proppants, which may result in a decreasing fracture conductivity due to fines generation. The lower hydrocarbon content of Bowland shale in conjunction with its low maturity may also limit its prospectivity compared to Posidonia shale.

The results of this study provide first order estimates on the time dependent fracture closure due to proppant embedment in shale rocks, which may be directly correlated with the productivity of wells. The correlation between mechanical properties such as the strength or Young's modulus and the creep behavior are specifically interesting for industry, since they can be quickly extracted from recorded stress-strain curves of constant strain rate experiments, which are performed with minor experimental effort. In addition, the (dynamic) Young's modulus, may also easily be derived from ultrasonic logs and, using our experimental results, may be used to estimate key aspects of shale reservoir rocks. With respect to the generation of fractures by hydraulic stimulation of the reservoir, the weak Posidonia shale may be more prospective since it exhibits considerably lower strength than the strong Bowland shale, resulting in a significantly lower fluid pressure, which is necessary to create fractures in the Posidonia than in the Bowland shale.

Additionally, the results of this study may be adapted to specific geothermal reservoirs, which are not located in (granitic) hard rocks, as it is currently under investigation within the European Initiative 'meet (Multi-sites EGS Demonstration)'. One main objective of this project is to demonstrate the viability of Enhanced Geothermal Systems (EGS) not only in granitic, but also sedimentary rocks. To maintain an economical energy production from these reservoirs, open fractures over long periods are necessary. Using the proposed constitutive equations may help to discriminate between geothermal reservoirs, which show a huge potential for an efficient and sustainable energy extraction and reservoirs, which are not suitable. The observations of this study may also find application with respect to the integrity of clays (or mudstones) for radioactive waste disposal, as currently investigated within the 'iCross' initiative (Integrity of nuclear waste

repository systems-Cross-scale system understanding and analysis) funded by the BMBF (German Federal Ministry of Education and Research). To guarantee the secure storage of radioactive waste, clays (or mudstones) in addition to salt or granitic rocks are regarded as potential host rock since they typically exhibit low permeability and the ability to retain radionuclides by physico-chemical adsorption. Potential reservoirs for radioactive waste disposal may be the Opalinus clay (Switzerland), the Boom Clay (Belgium) or the Callovo-Oxfordian clay (France). The sealing properties of natural or engineered clay barriers strongly depend on their long-term creep properties and may be estimated using the proposed constitutive equations. To reduce carbon dioxide (CO_2) emissions from the power or industrial sector, Carbon Capture and Storage (CCS) is considered as key technology. Suitable geological sites for CCS are in addition to saline aquifers also depleted oil and gas reservoirs. Thus, the observations of this study may also be adapted to estimate the usability of wells drilled in unconventional reservoirs for the secure

Chapter 6: Outlook

In this study we attempted to simulate in situ reservoir deformation conditions such as confining pressure, temperature and stress. However, the applied conditions may only represent a depth of $z \leq 4$ km and the results of this study are therefore potentially not applicable for reservoirs at larger depth. This may be due to different deformation mechanisms operating at larger depth, such as creep based on diffusion rather than dislocation processes. Thus, we suggest to perform deformation experiments also at higher p_c, T, σ - conditions as applied in this study. In addition, almost all experiments were performed perpendicular to bedding orientation. Several studies were conducted to investigate the influence of bedding angle on the mechanical properties of shale rocks as well as borehole stability (Meier et al. 2015; Sone and Zoback 2013b). They report an enhanced creep strain for shale samples loaded perpendicular to bedding compared to samples oriented parallel to bedding. Assuming a horizontal bedding orientation within the target horizon of an unconventional reservoir, this suggest a lower fracture closure rate of wells drilled in lateral direction. Therefore, the bedding direction should also be taken into consideration as a parameter influencing the productivity of a well drilled in unconventional shale reservoirs. For comparison, all experiments were performed after samples were dried at least for two days at 50 °C temperature. This clearly will not represent in situ conditions where rocks typically are at least partly saturated with the reservoir fluid. Since shale rocks are known to be very sensitive to changes in water content (Chong and Boresi 1990; Rutter and Mecklenburgh 2018; Sone and Zoback 2014), deformation experiments performed on Posidonia and Bowland shale at defined saturation states may be performed to unravel the influence of water content on the mechanical properties of these rocks. Additionally, the composition of the reservoir fluid as well as the frac fluid also has an effect on these properties due to chemical interactions between the fluid and the reservoir rock (Barbot et al. 2013; Hakala et al. 2017). Performing deformation experiments on shale rocks under true triaxial conditions may also be considered to gain more detailed knowledge of the short-and long-term behavior of these rocks.

Due to the strong heterogeneity of the investigated shale rocks, the constitutive equations we formulated describing the influence of applied deformation conditions are empirical and cannot cover all microphysical processes, which operate during deformation. Nonetheless, the empirical equations will be applicable to estimate the closure of fractures in shale rocks within the typical time period of a few years between refrac operations. Extrapolation to longer periods likely yields large errors and may require the analysis of synthetic shale samples, which allow studying the effect of varying composition. This will provide additional constraints on shale constitutive equations

As already stated in the 'General Introduction', the presented results of this study represent a first step in an effort to improve our understanding the time dependent fracture closure in shale reservoirs due to proppant embedment. Therefore, we will perform permeability measurements on Bowland and Posidonia shale samples including propped fractures in future studies. Here we will focus on the influence of boundary conditions (p_c, T, σ), petrophysical properties of the shale rocks, proppant properties, fluid chemistry, fracture geometry and proppant placement on the permeability decline of the propped fractures during constant stress deformation. Combining results of those experiments with the findings of this study and implementing them into numerical models will help to achieve an efficient and economic drainage of the reservoir.

References

Akrad OM, Miskimins JL, Prasad M (2011) The effects of fracturing fluids on shale rock mechanical properties and proppant embedment. In: SPE annual technical conference and exhibition. Society of Petroleum Engineers, Denver

Al-Rbeawi, Salam. 2018. "The Optimal Reservoir Configuration for Maximum Productivity Index of Gas Reservoirs Depleted by Horizontal Wells under Darcy and Non-Darcy Flow Conditions." *Journal of Natural Gas Science and Engineering* 49 (September 2017): 179–93. https://doi.org/10.1016/j.jngse.2017.11.012.

Akrad OM, Miskimins JL, Prasad M (2011) The effects of fracturing fluids on shale rock mechanical properties and proppant embedment. In: SPE annual technical conference and exhibition. Society of Petroleum Engineers, Denver

Almasoodi, Mouin M, Younane N Abousleiman, and Son K Hoang. 2014. "Viscoelastic Creep of Eagle Ford Shale : Investigating Fluid-Shale Geologic Settings of Eagle Ford Shale (Calcareous Mudstone)." *Society of Petroleum Engineers.*

Alramahi B, Sundberg MI (2012) Proppant embedment and conduc- tivity of hydraulic fractures in shales. In: 46th U.S. Rock Mechanics/Geomechanics Symposium. American Rock Mechanics Association, Chicago

Andrews, Ian J. 2013. "The Carboniferous Bowland Shale Gas Study: Geology and Resource Estimation." *British Geological Survey for Department of Energy and Climate Change, London, UK*, 64. https://doi.org/10.1080/10962247.2014.897270.

Atkinson, B. K. 1987. *Fracture Mechanics of Rock*. London: Academic Press. https://doi.org/10.1016/j.ica.2007.03.020.

Baihly JD, Altman RM, Malpani R, Luo F (2010) Shale gas production decline trend comparison over time and basins. In: SPE annual technical conference and exhibition. Society of

Petroleum Engineers, Florence

Bauer, A., R.M. Holt, J. Stenebråten, E.F. Sønstebø, and L. Marøen. 2014. "Thermally Induced Compaction of Shales." *48th US Rock Mechanics/Geomechanics Symposium.*

Bikong C, Hoxha D, Shao JF (2015) A micro-macro model for time- dependent behavior of clayey rocks due to anisotropic propagation of microccracks. Int J Plast 69:73-88

Berard, T, Q. Liu, F.-X. Dubost, and B. Jing. 2012. "A Screening Process for Shale Gas Prospecting." *EAGE Annual Conference & Exhibition*, no. June: 4–7.

Bieniawski, Z T. 2008. "ISRM International Symposium 2008." *Rock Mechanics*, no. November: 24–26.

Bonini M, Debernardi D, Barla M, Barla G (2007) The mechanical behaviour of clay shales and implications on the design of tunnels. Rock Mech Rock Eng 42:361

Bouazza, A., W. F. Van Impe, and W. Haegeman. 1996. "Some Mechanical Properties of Reconstituted Boom Clay." *Geotechnical and Geological Engineering* 14 (4): 341–52. https://doi.org/10.1007/BF00421948.

Bourg, Ian C. 2015. "Sealing Shales versus Brittle Shales: A Sharp Threshold in the Material Properties and Energy Technology Uses of Fine-Grained Sedimentary Rocks." *Environmental Science and Technology Letters* 2 (10): 255–59. https://doi.org/10.1021/acs.estlett.5b00233.

Brantut, N., P. Baud, M. J. Heap, and P. G. Meredith. 2012. "Micromechanics of Brittle Creep in Rocks." *Journal of Geophysical Research: Solid Earth* 117 (8): 1–12. https://doi.org/10.1029/2012JB009299.

Brantut, N., M. J. Heap, P. G. Meredith, and P. Baud. 2013. "Time-Dependent Cracking and Brittle Creep in Crustal Rocks: A Review." *Journal of Structural Geology* 52 (1): 17–43. https://doi.org/10.1016/j.jsg.2013.03.007.

Brantut, N, M J Heap, P Baud, and P G Meredith. 2014. "Rate- and Strain-Dependent Brittle

Deformation of Rocks." *Journal of Geophysical Research: Solid Earth*, 1–19. https://doi.org/10.1002/2013JB010448.

Brantut, Nicolas, Michael J Heap, Patrick Baud, and Philip G Meredith. 2014. "Mechanisms of Time-Dependent Deformation in Porous Limestone." *Journal of Geophysical Research: Solid Earth*, 5444–63. https://doi.org/10.1002/2014JB011186.

Britt, Larry Kevin, and Jerry Schoeffler. 2009. "The Geomechanics Of A Shale Play: What Makes A Shale Prospective." *SPE Eastern Regional Meeting*, no. September: 23–25. https://doi.org/10.2118/125525-MS.

Burger, Bruno. 2018. "Stromerzeugung in Deutschland Im Ersten Halbjahr 2018." Freiburg. https://www.ise.fraunhofer.de/content/dam/ise/de/documents/publications/studies/daten-zu-erneuerbaren-energien/ISE_Stromerzeugung_2018_Halbjahr.pdf.

Bürgmann R, Dresen G (2008) Rheology of the lower crust and upper mantle: evidence from rock mechanics, geodesy, and field observations. Annu Rev Earth Planet Sci 36:531–567

Cerasi, Pierre, Elisabeth Lund, Marta Laukeland Kleiven, Anna Stroisz, Srutarshi Pradhan, Claus Kjøller, Peter Frykman, and Erling Fjær. 2017. "Shale Creep as Leakage Healing Mechanism in CO2Sequestration." *Energy Procedia* 114 (1876): 3096–3112. https://doi.org/10.1016/j.egypro.2017.03.1439.

Chang, Chandong, Mark D. Zoback, and Abbas Khaksar. 2006. "Empirical Relations between Rock Strength and Physical Properties in Sedimentary Rocks." *Journal of Petroleum Science and Engineering* 51 (3–4): 223–37. https://doi.org/10.1016/j.petrol.2006.01.003.

Chang C, Zoback MD (2009) Viscous creep in room-dried uncon- solidated Gulf of Mexico shale (I): experimental results. J Pet Sci Eng 69:239–246

Chang C, Zoback MD (2010) Viscous creep in room-dried uncon- solidated Gulf of Mexico shale (II): development of a viscoplas- ticity model. J Pet Sci Eng 72:50–55

Chen D, Ye Z, Pan Z, Zhou Y, Zhang J (2017) A permeability model for the hydraulic fracture

filled with proppant packs under combined effect of compaction and embedment. J Pet Sci Eng 149:428–435

Chindam, Chandraprakash, Krishnamurthy Chitti Venkata, Krishnan Balasubramaniam, and Raghu V. Prakash. 2013. "Thermomechanical Response of Metals: Maxwell vs. Kelvin-Voigt Models." *Materials Science and Engineering A* 560: 54–61. https://doi.org/10.1016/j.msea.2012.08.152.

Chong, K, and A. P. Boresi. 1990. "Strain Rate Dependent Mechanical Properties of New Albany Reference Shale." *International Journal of Rock Mechanics and Mining Sciences And* 27 (3): 199–205. https://doi.org/10.1016/0148-9062(90)94328-Q.

Chong, K, P M Hoyt, J W Smith, and B Y Paulsen. 1980. "Effects of Strain Rate on Oil Shale Fracturing." *International Journal of Rock Mechanics and Mining Sciences & Geomechanics Abstracts* 17: 35–43. https://doi.org/10.1016/0148-9062(80)90004-2.

Chong, K, JW Smith, Bin Chang, MH Philip, and HC Carpenter. 1976. "Characterization of Oil Shale under Uniaxial Compression." *American Rock Mechanics Association* The 17th U. https://www.onepetro.org/conference-paper/ARMA-76-0465.

Chong KP, Smith JW, Khaliki BA (1978) Creep and relaxation of oil shale. In: 19th U.S. Symposium on Rock Mechanics (USRMS). American Rock Mechanics Association, Reno

Ciccotti, Matteo. 2009. "Stress-Corrosion Mechanisms in Silicate Glasses." *Journal of Physics D: Applied Physics* 42 (21). https://doi.org/10.1088/0022-3727/42/21/214006.

Cogan J (1976) Triaxial creep tests of Opohonga limestone and Ophir shale. Int J Rock Mech Min Sci Geomech Abstr 13:1–10

Crawford, B. R., D. R. Faulkner, and E. H. Rutter. 2008. "Strength, Porosity, and Permeability Development during Hydrostatic and Shear Loading of Synthetic Quartz-Clay Fault Gouge." *Journal of Geophysical Research: Solid Earth* 113 (3): 1–14. https://doi.org/10.1029/2006JB004634.

de Waal JA, Smits RMM (1988) Prediction of reservoir compaction and surface subsidence: field application of a new model. SPE Form Eval 3:347–356

Dewers, Thomas A., Kathleen A. Issen, David J. Holcomb, William A. Olsson, and Mathew D. Ingraham. 2017. "Strain Localization and Elastic-Plastic Coupling during Deformation of Porous Sandstone." *International Journal of Rock Mechanics and Mining Sciences* 98 (June): 167–80. https://doi.org/10.1016/j.ijrmms.2017.06.005.

Dong, Kangyin, Renjin Sun, and Xiucheng Dong. 2018. "CO2 Emissions, Natural Gas and Renewables, Economic Growth: Assessing the Evidence from China." *Science of the Total Environment* 640–641: 293–302. https://doi.org/10.1016/j.scitotenv.2018.05.322.

Dorner, D., K. Röller, and B. Stöckhert. 2014. "High Temperature Indentation Creep Tests on Anhydrite - A Promising First Look." *Solid Earth* 5 (2): 805–19. https://doi.org/10.5194/se-5-805-2014.

Draege, A., M. Jakobsen, and T. A. Johansen. 2006. "Rock Physics Modelling of Shale Diagenesis." *Petroleum Geoscience* 12 (1): 49–57. https://doi.org/10.1144/1354-079305-665.

Dudley JW II, Myers MT, Shew RD, Arasteh MM (1998) Measuring compaction and compressibilities in unconsolidated reservoir materials by time-scaling creep. SPE Reservoir Eval Eng 1:430–437

Energy Information Administration, US. 2018. "Natural Gas Annual 2017."

Eseme, E., J. L. Urai, B. M. Kross, and R. Littke. 2007. "Review of Mechanical Properties of Oil Shales: Implications for Exploitation and Basin Modelling." *Oil Shale* 24 (2): 159–74.

Evans, Brian, Joanne T. Fredrich, and Teng-fong Wong. 1990. "The Brittle-Ductile Transition in Rocks: Recent Experimental and Theoretical Progress." *Geophysical Monograph Series.* https://doi.org/10.1029/GM056p0001.

Evans, Brian, and David L. Kohlstedt. 1995. "Rheology of Rocks." In *Rock Physics and Phase Relations - A Handbook of Physical Constants*, 148–65. AGU Reference Shelf 3.

https://doi.org/10.1029/RF003p0148.

Fabre G, Pellet F (2006) Creep and time-dependent damage in argillaceous rocks. Int J Rock Mech Min Sci 43:950–960

Farrokhrouz, Mohsen, Mohammad Reza Asef, and Riyaz Kharrat. 2014. "Empirical Estimation of Uniaxial Compressive Strength of Shale Formations." *Geophysics* 79 (4): D227–33. https://doi.org/10.1190/geo2013-0315.1.

Findley, W., J. Lai, and K. Onaran. 1976. *Creep and Relaxation of Nonlinear Viscoelastic Materials with an Introduction to Linear Viscoelasticity. Dover Publication.* Vol. 19. New York. https://doi.org/10.1016/0032-3861(78)90187-8.

Fischer Q, Kets F, Crook A (2013) Self-sealing of faults and fractures in argillaceous formations: evidence from the petroleum indus- try. Nagra Arbeitsber. NAB 13-06

Fjær E, Larsen I, Holt RM, Bauer A (2014) A creepy model for creep. In: 48th U.S. Rock Mechanics/Geomechanics Symposium. American Rock Mechanics Association, Minneapolis

Freund, Dieter, Zichao Wang, Erik Rybacki, and Georg Dresen. 2004. "High-Temperature Creep of Synthetic Calcite Aggregates: Influence of Mn-Content." *Earth and Planetary Science Letters* 226 (3–4): 433–48. https://doi.org/10.1016/j.epsl.2004.06.020.

Frost H, Ashby M (1982) Deformation-mechanism maps. The plasticity and creep of metals and ceramics. Pergamon Press, Oxford

Gasc-Barbier M, Chanchole S, Be´rest P (2004) Creep behavior of Bure clayey rock. Appl Clay Sci 26:449–458

GAO, Yanan, Feng GAO, Zhizhen ZHANG, and Tao ZHANG. 2010. "Visco-Elastic-Plastic Model of Deep Underground Rock Affected by Temperature and Humidity." *Mining Science and Technology* 20 (2): 183–87. https://doi.org/10.1016/S1674-5264(09)60181-2.

Gasparik, Matus, Pieter Bertier, Yves Gensterblum, Amin Ghanizadeh, Bernhard M. Krooss, and Ralf Littke. 2014. "Geological Controls on the Methane Storage Capacity in Organic-

Rich Shales." *International Journal of Coal Geology* 123: 34–51. https://doi.org/10.1016/j.coal.2013.06.010.

Ghanizadeh, Amin, Matus Gasparik, Alexandra Amann-Hildenbrand, Yves Gensterblum, and Bernhard M. Krooss. 2014. "Experimental Study of Fluid Transport Processes in the Matrix System of the European Organic-Rich Shales: I. Scandinavian Alum Shale." *Marine and Petroleum Geology* 51: 79–99. https://doi.org/10.1016/j.marpetgeo.2013.10.013.

Gholami, R., A. Moradzadeh, V. Rasouli, and J. Hanachi. 2014. "Practical Application of Failure Criteria in Determining Safe Mud Weight Windows in Drilling Operations." *Journal of Rock Mechanics and Geotechnical Engineering* 6 (1): 13–25. https://doi.org/10.1016/j.jrmge.2013.11.002.

Götze, Lutz Christoph, Rainer Abart, Erik Rybacki, Lukas M. Keller, Elena Petrishcheva, and Georg Dresen. 2010. "Reaction Rim Growth in the System MgO-Al2O3-SiO2 under Uniaxial Stress." *Mineralogy and Petrology* 99 (3–4): 263–77. https://doi.org/10.1007/s00710-009-0080-3.

Green, Christopher, A., Peter Styles, and Brian J. Baptie. 2012. "Shale Gas Fracturing Review & Recommendations for Induced Seismic Migration," 26. http://www.businessgreen.com/digital_assets/5216/DECC_shale_gas_report.pdf.

Guo J, Liu Y (2012) Modeling of proppant embedment: elastic deformation and creep deformation. In: SPE international production and operations conference & exhibition. Society of Petroleum Engineers, Doha

Guo, Tiankui, Shicheng Zhang, Jun Gao, Jingchen Zhang, and Haiqing Yu. 2013. "Experimental Study of Fracture Permeability for Stimulated Reservoir Volume (SRV) in Shale Formation." *Transport in Porous Media* 98 (3): 525–42. https://doi.org/10.1007/s11242-013-0157-7.

Gupta, V. 1975. "The Creep Behavior of Standard Linear Solid." *Journal of Applied Polymer Science* 19.

Hagin P, Zoback M (2004) Viscous deformation of unconsolidated reservoir sands—Part 2: linear viscoelastic models. Geophysics 69:742–751

Hart, E.W. 1970. "A Phenomenological Theory for Plastic Deformation of Polycrystalline Metals." *Acta Metallurgica* 18: 599–610. https://doi.org/10.1016/0001-6160(70)90089-1.

Hausfather, Zeke. 2015. "Bounding the Climate Viability of Natural Gas as a Bridge Fuel to Displace Coal." *Energy Policy* 86: 286–94. https://doi.org/10.1016/j.enpol.2015.07.012.

Heap, M. J., P. Baud, P. G. Meredith, A. F. Bell, and I. G. Main. 2009. "Time-Dependent Brittle Creep in Darley Dale Sandstone." *Journal of Geophysical Research: Solid Earth* 114 (7): 1–22. https://doi.org/10.1029/2008JB006212.

Heap MJ, Baud P, Meredith PG (2009b) Influence of temperature on brittle creep in sandstones. Geophys Res Lett 36:L19305. doi:10. 1029/2009GL039373

Heller RJ, Zoback MD (2011) Adsorption, swelling and viscous creep of synthetic clay samples. In: 45th U.S. Rock Mechanics/ Geomechanics Symposium. American Rock Mechanics Association, San Francisco

Herrmann, J., E. Rybacki, H. Sone, and G. Dresen. 2018. "Deformation Experiments on Bowland and Posidonia Shale—Part I: Strength and Young's Modulus at Ambient and In Situ Pc–T Conditions." *Rock Mechanics and Rock Engineering* 0 (0): 0. https://doi.org/10.1007/s00603-018-1572-4.

Hobbs, Bruce, and Alison Ord. 2015. "Chapter 8 - Brittle Flow." In , edited by Bruce Hobbs and Alison B T - Structural Geology Ord, 243–85. Oxford: Elsevier. https://doi.org/https://doi.org/10.1016/B978-0-12-407820-8.00008-4.

Hol S, Zoback MD (2013) Creep behavior of coal and shale related to adsorption of reservoir fluids. In: 47th U.S. Rock Mechanics/ Geomechanics Symposium. American Rock Mechanics Association, San Francisco

Hollomon, J. 1947. "The Mechanical Euation of State." *Transactions of the Metallurgical Society*

of AIME 171: 535–45.

Holt, R. M., E. Fjær, O. M. Nes, and H.T. Alassi. 2011. "A Shaly Look at Brittleness." *American Rock Mechanics Association*, 1–10.

Holt, R.M., O.-M Nes, and E. Fjær. 2012. "Static vs . Dynamic Behavior of Shale." *American Rock Mechanics Association*.

Horsfield, Brian, Rolando Primio, and Hans-martin Schulz. 2011. "Geo-Energie : Konventionelle Und Unkonventionelle Fossile Ressourcen." *System Erde* 2 (2011): 16–31. https://doi.org/10.2312/GFZ.syserde.01.02.2.

Horsrud, P. 2001. "Estimating Mechanical Properties of Shale From Empirical Correlations." *Society of Petroleum Engineers* SPE 56017 (June): 68–73. https://doi.org/10.2118/56017-PA.

Hough, Edward, Christopher H Vane, Nigel JP Smith, and Vicky L Moss-Hayes. 2014. "The Bowland Shale in the Roosecote Borehole of the Lancaster Fells Sub-Basin, Craven Basin, UK: A Potential UK Shale Gas Play?" *SPE/EAGE European Unconventional Resources Conference and Exhibition*, no. December. https://doi.org/10.2118/167696-MS.

Howarth, Robert W., and Anthony Ingraffea. 2011. "Natural Gas: Should Fracking Stop?" *Nature* 477 (7364): 271–75. https://doi.org/10.1038/477271a.

Hughes, J David. 2013. "A Reality Check on the Shale Revolution." *Nature* 494: 307–8.

Ibanez, William D., and Andreas K. Kronenberg. 1993. "Experimental Deformation of Shale: Mechanical Properties and Microstructural Indicators of Mechanisms." *International Journal of Rock Mechanics and Mining Sciences And* 30 (7): 723–34. https://doi.org/10.1016/0148-9062(93)90014-5.

Ilgen, Anastasia G., Jason E. Heath, I. Yucel Akkutlu, L. Taras Bryndzia, David R. Cole, Yousif K. Kharaka, Timothy J. Kneafsey, Kitty L. Milliken, Laura J. Pyrak-Nolte, and Roberto Suarez-Rivera. 2017. "Shales at All Scales: Exploring Coupled Processes in Mudrocks."

Earth-Science Reviews 166: 132–52. https://doi.org/10.1016/j.earscirev.2016.12.013.

Imber, Jonathan, Howard Armstrong, Sarah Clancy, Susan Daniels, Liam Herringshaw, Ken McCaffrey, Joel Rodrigues, Joao Trabucho-Alexandre, and Cassandra Warren. 2014. "Natural Fractures in a United Kingdom Shale Reservoir Analog, Cleveland Basin, Northeast England." *AAPG Bulletin* 98 (11): 2411–37. https://doi.org/10.1306/07141413144.

International Energy Agency. 2018. "World Energy Balances: Overview."

Islam, Md Aminul, and Paal Skalle. 2013. "An Experimental Investigation of Shale Mechanical Properties through Drained and Undrained Test Mechanisms." *Rock Mechanics and Rock Engineering* 46 (6): 1391–1413. https://doi.org/10.1007/s00603-013-0377-8.

Jarvie, D M, R J Hill, and R M Pollastro. 2005. "Assessment of the Gas Potential and Yields from Shales: The Barnett Shale Model." *Unconventional Energy Resources in the Southern Midcontinent*, no. April 2015: 37–50.

Ji, Shaocheng, Qin Wang, Bin Xia, and Denis Marcotte. 2004. "Mechanical Properties of Multiphase Materials and Rocks: A Phenomenological Approach Using Generalized Means." *Journal of Structural Geology* 26 (8): 1377–90. https://doi.org/10.1016/j.jsg.2003.12.004.

Jiang Q, Qi Y, Wang Z, Zhou C (2013) An extended Nishihara model for the description of three stages of sandstone creep. Geophys J Int 193:841–854

Johnston, David H. 1987. "Physical Properties of Shale at Temperature and Pressure." *Geophysics* 52 (10): 1391–1401. https://doi.org/10.1190/1.1442251.

Jordan, Peter, and Rolf Nüesch. 1989. "Deformational Behavior of Shale Interlayers in Evaporite Detachment Horizons, Jura Overthrust, Switzerland." *Journal of Structural Geology* 11 (7): 859–71. https://doi.org/10.1016/0191-8141(89)90103-X.

Karato, Shun - Ichiro. 2008. *Deformation of Earth Materials - An Introduction to the Rheology of Solid Earth*. Cambridge University Press.

Kassis SM, Sondergeld CH (2010) Gas shale permeability: effects of roughness, proppant, fracture offset, and confining pressure. In: International oil and gas conference and exhibition in China. Society of Petroleum Engineers, Beijing

Kassner, Michael E., and Kamia Smith. 2014. "Low Temperature Creep Plasticity." *Journal of Materials Research and Technology* 3 (3): 280–88. https://doi.org/10.1016/j.jmrt.2014.06.009.

Kikumoto, Mamoru, Vu Pham Quang Nguyen, Hideaki Yasuhara, and Kiyoshi Kishida. 2017. "Constitutive Model for Soft Rocks Considering Structural Healing and Decay." *Computers and Geotechnics* 91: 93–103. https://doi.org/10.1016/j.compgeo.2017.07.003.

Könitzer, Sven F., Sarah J. Davies, Michael H. Stephenson, and Melanie J. Leng. 2014. "Depositional Controls on Mudstone Lithofacies in a Basinal Setting: Implications for the Delivery of Sedimentary Organic Matter." *Journal of Sedimentary Research* 84 (3): 198–214. https://doi.org/10.2110/jsr.2014.18.

Kranz, Robert L. 1980. "The Effects of Confining Pressure and Stress Difference on Static Fatigue of Granite." *Journal of Geophysical Research* 85 (80): 1854–66. https://doi.org/10.1029/JB085iB04p01854.

Kranz, Robert L., Harris William J., and Neville L. Carter. 1982. "Static Fatigue of Granite at 200 °C." *Geophysical Research Letters* 9 (1): 1–4.

Kuchler, Magdalena. 2017. "Post-Conventional Energy Futures: Rendering Europe's Shale Gas Resources Governable." *Energy Research and Social Science* 31 (October 2016): 32–40. https://doi.org/10.1016/j.erss.2017.05.028.

Kuila, U., D. N. Dewhurst, A. F. Siggins, and M. D. Raven. 2011. "Stress Anisotropy and Velocity Anisotropy in Low Porosity Shale." *Tectonophysics* 503 (1–2): 34–44. https://doi.org/10.1016/j.tecto.2010.09.023.

Kwon, Ohmyoung, and Andreas K. Kronenberg. 1994a. "Deformation of Wilcox Shale: Undrained Strengths and Effects of Strain Rate." *Rock Mechanics*.

Kwon O., Kronenberg AK. 1994b. "Deformation of Wilcox Shale: Undrained Strengths and Effects of Strain Rate." *Rock Mechanics.*

Lajtai, Emery Z., E J Scott Duncan, and B J Carter. 1991. "Technical Note - The Effect of Strain Rate on Rock Strength." *Rock Mechanics and Rock Engineering*, no. 24: 99–109. https://doi.org/10.1007/BF01032501.

Li, Quanshu, Huilin Xing, Jianjun Liu, and Xiangchon Liu. 2015. "A Review on Hydraulic Fracturing of Unconventional Reservoir." *Petroleum* 1 (1): 8–15. https://doi.org/10.1016/j.petlm.2015.03.008.

Li X, Shao Z (2016) Investigation of macroscopic brittle creep failure caused by microcrack growth under step loading and unloading in rocks. Rock Mech Rock Eng 49:2581–2593

Liu Y, Sharma MM (2005) Effect of fracture width and fluid rheology on proppant settling and retardation: an experimental study. In: SPE annual technical conference and exhibition. Society of Petroleum Engineers, Dallas

Li, Y., and A. Ghassemi. 2012. "Creep Behavior of Barnett , Haynesville , and Marcellus Shale." *American Rock Mechanics Association.*

Li, Zhichao, Lianchong Li, Bo Huang, Liaoyuan Zhang, Ming Li, Jiaqiang Zuo, Aishan Li, and Qinglei Yu. 2017. "Numerical Investigation on the Propagation Behavior of Hydraulic Fractures in Shale Reservoir Based on the DIP Technique." *Journal of Petroleum Science and Engineering* 154 (April): 302–14. https://doi.org/10.1016/j.petrol.2017.04.034.

Littke, R., B. Krooss, A. K. Uffmann, H. M. Schulz, and B. Horsfield. 2011. "Unconventional Gas Resources in the Paleozoic of Central Europe." *Oil and Gas Science and Technology* 66 (6): 953–77. https://doi.org/10.2516/ogst/2010033.

Lockner DA (1995) Rock Failure. In: Ahrens TJ (ed) Rock physics and phase relations: a handbook of physical constants. Ref. Shelf. AGU, Washington, pp 127–147

Main IG (2000) A damage mechanics model for power-law creep and earthquake aftershock and

foreshock sequences. Geophys J Int 142:151–161

Masri, M., M. Sibai, J. F. Shao, and M. Mainguy. 2014. "Experimental Investigation of the Effect of Temperature on the Mechanical Behavior of Tournemire Shale." *International Journal of Rock Mechanics and Mining Sciences* 70: 185–91. https://doi.org/10.1016/j.ijrmms.2014.05.007.

Masuti S, Barbot SD, Karato S-I, Feng L, Banerjee P (2016) Upper- mantle water stratification inferred from observations of the 2012 Indian Ocean earthquake. Nature 538:373–377

Mavko, Gary, Tapan Mukerji, and Jack Dvorkin. 2009. *The Rock Physics Handbook - Tools for Seismic Analysis of Porous Media*. Second Edi. Cambridge University Press.

McGlade, Christophe, Jamie Speirs, and Steve Sorrell. 2013. "Unconventional Gas - A Review of Regional and Global Resource Estimates." *Energy* 55: 571–84. https://doi.org/10.1016/j.energy.2013.01.048.

Mighani S, Taneja S, Sondergeld CH, Rai CS (2015) Nanoindentation creep measurements on shale. In: 49th U.S. Rock Mechanics/ Geomechanics Symposium. American Rock Mechanics Associ- ation, San Francisco

Meier, T., E. Rybacki, T. Backers, and G. Dresen. 2015. "Influence of Bedding Angle on Borehole Stability: A Laboratory Investigation of Transverse Isotropic Oil Shale." *Rock Mechanics and Rock Engineering* 48 (4): 1535–46. https://doi.org/10.1007/s00603-014-0654-1.

Meier, T., E. Rybacki, A. Reinicke, and G. Dresen. 2013. "Influence of Borehole Diameter on the Formation of Borehole Breakouts in Black Shale." *International Journal of Rock Mechanics and Mining Sciences* 62: 74–85. https://doi.org/10.1016/j.ijrmms.2013.03.012.

Meier, T. 2017. "Borehole Breakouts in Transversely Isotropic Posidonia Shale." Universität Potsdam.

Mikhail, R., and N. Guindy. 1971. "Rates of Low-Temperature Dehydration of Montmorillonite

and Illite." *Journal of Applied Chemistry and Biotechnology* 21 (4): 113–16.
https://doi.org/10.1002/jctb.5020210407.

Mittal, Abhinav, Chandra S Rai, and Carl H Sondergeld. 2018. "Proppant-Conductivity Testing
Under Simulated Reservoir Conditions: Impact of Crushing, Embedment, and Diagenesis on
Long-Term Production in Shales." *SPE Journal* 23 (04): 1304–15.
https://doi.org/10.2118/191124-PA.

Morales RH, Suarez-Rivera R, Edelman E (2011) Experimental evaluation of hydraulic fracture
impairment in shale reservoirs. In: 45th U.S. Rock Mechanics/Geomechanics Symposium.
American Rock Mechanics Association, San Francisco

Morley, C. K., C. von Hagke, R. L. Hansberry, A. S. Collins, W. Kanitpanyacharoen, and R.
King. 2017. "Review of Major Shale-Dominated Detachment and Thrust Characteristics in
the Diagenetic Zone: Part I, Meso- and Macro-Scopic Scale." *Earth-Science Reviews* 173
(August): 168–228. https://doi.org/10.1016/j.earscirev.2017.07.019.

Mouazen M, Poulesquen A, Vergnes B (2011) Correlation between thermal and rheological
studies to characterize the behavior of bitumen. Rheol Acta 50:169–178

Nara Y, Morimoto K, Yoneda T, Hiroyoshi N, Kaneko K (2011) Effects of humidity and
temperature on subcritical crack growth in sandstone. Int J Solids Struct 48:1130–1140

Naumann, Marcel, Udo Hunsche, and Otto Schulze. 2007. "Experimental Investigations on
Anisotropy in Dilatancy, Failure and Creep of Opalinus Clay." *Physics and Chemistry of
the Earth* 32 (8–14): 889–95. https://doi.org/10.1016/j.pce.2005.04.006.

Neeraj, T., D. H. Hou, G. S. Daehn, and M. J. Mills. 2000. "Phenomenological and
Microstructural Analysis of Room Temperature Creep in Titanium Alloys." *Acta Materialia*
48 (6): 1225–38. https://doi.org/10.1016/S1359-6454(99)00426-7.

Niandou, H., J.F. Shao, J.P. Henry, and D. Fourmaintraux. 1997. "Laboratory Investigation of
the Mechanical Behaviour of Tournemire Shale." *International Journal of Rock Mechanics
and Mining Sciences* 34 (1): 3–16. https://doi.org/10.1016/S1365-1609(97)80029-9.

Norris JQ, Turcotte DL, Moores EM, Brodsky EE, Rundle JB (2016) Fracking in Tight Shales: what is it, what does it accomplish, and what are its consequences? AnnuRev Earth Planet Sci 44:321–351

Ougier-Simonin, Audrey, François Renard, Claudine Boehm, and Sandrine Vidal-Gilbert. 2016. "Microfracturing and Microporosity in Shales." *Earth-Science Reviews* 162: 198–226. https://doi.org/10.1016/j.earscirev.2016.09.006.

Paterson, M. S. 1970. "A High-Pressure, High-Temperature Apparatus for Rock Deformation." *International Journal of Rock Mechanics and Mining Sciences And* 7 (5): 517–26. https://doi.org/10.1016/0148-9062(70)90004-5.

Paterson, M. S. 2013. *Materials Science for Structural Geology.* London: Springer. https://doi.org/10.1007/978-94-007-5545-1.

Paterson MS, Wong TF (2005) Experimental rock deformation—the brittle field, 2nd edn. Springer, Berlin

Paul, B. 1960. "Prediction of Elastic Constants of Multiphase Materials." *Transactions of the Metallurgical Society of AIME* 218: 36–41.

Patzek T, Male F, Marder M (2014) A simple model of gas production from hydrofractured horizontal wells in shales. AAPG Bull 98:2507–2529

Pedlow J, Sharma M (2014) Changes in shale fracture conductivity due to interactions with water-based fluids. In: SPE hydraulic fracturing technology conference. Society of Petroleum Engi- neers, The Woodlands

Petley, DN. 1999. "Failure Envelopes of Mudrocks at High Confining Pressures." *Geological Society, London, Special Publications* 158 (1): 61–71. https://doi.org/10.1144/GSL.SP.1999.158.01.05.

Ranalli G (1987) Rheology of the earth: deformation and flow processes in geophysics and geodynamics. Allen & Unwin, Boston

Rassouli, F. S., and MD Zoback. 2015. "Long-Term Creep Experiments on Haynesville Shale Rocks." *American Rock Mechanics Association.*

Reinicke A, Rybacki E, Stanchits S, Huenges E, Dresen G (2010) Hydraulic fracturing stimulation techniques and formation damage mechanisms—implications from laboratory testing of tight sandstone–proppant systems. Chemie der Erde - Geochem- istry 70(Supplement 3):107–117

Rickman, Rick, Michael J. Mullen, James Erik Petre, William Vincent Grieser, and Donald Kundert. 2008. "A Practical Use of Shale Petrophysics for Stimulation Design Optimization: All Shale Plays Are Not Clones of the Barnett Shale." *SPE Annual Technical Conference and Exhibition*, no. Wang: 1–11. https://doi.org/10.2118/115258-MS.

Rybacki E, Paterson MS, Wirth R, Dresen G (2003) Rheology of calcite–quartz aggregates deformed to large strain in torsion. J Geophys Res 108:2089. doi:10.1029/2002JB001833

Rybacki, E., J. Herrmann, R. Wirth, and G. Dresen. 2017. "Creep of Posidonia Shale at Elevated Pressure and Temperature." *Rock Mechanics and Rock Engineering*, 1–20. https://doi.org/10.1007/s00603-017-1295-y.

Rybacki, E., T. Meier, and G. Dresen. 2016. "What Controls the Mechanical Properties of Shale Rocks? - Part II: Brittleness." *Journal of Petroleum Science and Engineering* 144: 39–58. https://doi.org/10.1016/j.petrol.2016.02.022.

Rybacki, E., Andreas Reinicke, T. Meier, M. Makasi, and G. Dresen. 2015. "What Controls the Mechanical Properties of Shale Rocks? – Part I: Strength and Young's Modulus." *Journal of Petroleum Science and Engineering* 135: 702–22. https://doi.org/10.1016/j.petrol.2016.02.022.

Schmitt L, Forsans T, Santarelli FJ (1994) Shale testing and capillary phenomena. Int J Rock Mech Min Sci 31:441–447

Shah, M, S Shah, and A Sircar. 2017. "A Comprehensive Overview on Recent Developments in Refracturing Technique for Shale Gas Reservoirs." *Journal of Natural Gas Science and*

Engineering 46: 350–64. https://doi.org/10.1016/j.jngse.2017.07.019.

Sheorey, P.R. 1997. *Empirical Rock Failure Criteria.*

Sherby, O D, O A Ruano, and J Wadsworth. 1999. "Deformation Mechanisms in Crystalline Solids and {Newton}ian Viscous Behavior." *The Minerals, Metals and Materials Society*, 397–411.

Smith, N, P Turner, G Williams, British Geological Survey, Kingsley Dunham Centre, Nicker Hill, and Keyworth Ng. 2010. "UK Data and Analysis for Shale Gas Prospectivity." *Geological Society, London, Petroleum Geology Conference Series* 7: 1087–98. https://doi.org/10.1144/0071087.

Soliman, M. Y., Johan Daal, and Loyd East. 2012. "Fracturing Unconventional Formations to Enhance Productivity." *Journal of Natural Gas Science and Engineering* 8: 52–67. https://doi.org/10.1016/j.jngse.2012.01.007.

Sondergeld, Carl H., Kent Edward Newsham, Joseph Thomas Comisky, Morgan Craig Rice, and Chandra Shekhar Rai. 2010. "Petrophysical Considerations in Evaluating and Producing Shale Gas Resources." *SPE Unconventional Gas Conference.* https://doi.org/10.2118/131768-MS.

Sone, H, and MD Zoback. 2010. "Strength, Creep and Frictional Properties of Gas Shale Reservoir Rocks." *… Symposium and 5th US-Canada Rock ….* http://www.onepetro.org/mslib/servlet/onepetropreview?id=ARMA-10-463.

Sone H, Zoback MD (2011) Visco-plastic properties of shale gas reservoir rocks. In: 45th U.S. Rock Mechanics/Geomechanics Symposium. American Rock Mechanics Association, San Francisco

Sone, Hiroki, and Mark D. Zoback. 2013a. "Mechanical Properties of Shale-Gas Reservoir Rocks - Part 1: Static and Dynamic Elastic Properties and Anisotropy." *Geophysics* 78 (5): D381–92. https://doi.org/10.1190/geo2013-0050.1.

Sone, Hiroki, and Mark D. Zoback. 2013b. "Mechanical Properties of Shale-Gas Reservoir Rocks — Part 2: Ductile Creep, Brittle Strength, and Their Relation to the Elastic Modulus." *Geophysics* 78 (5): D393–402. https://doi.org/10.1190/geo2013-0051.1.

Sone, Hiroki, and Mark D. Zoback. 2014. "Time-Dependent Deformation of Shale Gas Reservoir Rocks and Its Long-Term Effect on the in Situ State of Stress." *International Journal of Rock Mechanics and Mining Sciences* 69: 120–32. https://doi.org/10.1016/j.ijrmms.2014.04.002.

Stegent NA, Wagner AL, Mullen J, Borstmayer RE (2010) Engi- neering a successful fracture-stimulation treatment in the Eagle

Ford shale. In: Tight Gas Completions Conference. Society of Petroleum Engineers, San Antonio

Stouffer DC, Dame LT (1996) Inelastic deformation of metals. Wiley, New York

Swan, G., J. Cook, S. Bruce, and R. Meehan. 1989. "Strain Rate Effects in Kimmeridge Bay Shale." *International Journal of Rock Mechanics and Mining Sciences & Geomechanics Abstracts* 26 (2): 135–49. https://doi.org/10.1016/0148-9062(89)90002-8.

Tan, Jingqiang, Brian Horsfield, Reinhard Fink, Bernhard Krooss, Hans Martin Schulz, Erik Rybacki, Jinchuan Zhang, Christopher J. Boreham, Ger Van Graas, and Bruce A. Tocher. 2014. "Shale Gas Potential of the Major Marine Shale Formations in the Upper Yangtze Platform, South China, Part III: Mineralogical, Lithofacial, Petrophysical, and Rock Mechanical Properties." *Energy and Fuels* 28 (4): 2322–42. https://doi.org/10.1021/ef4022703.

Teixeira, Marcello Goulart, Frédéric Donzé, François Renard, Hamed Panahi, Efthymios Papachristos, and Luc Scholtès. 2017. "Microfracturing during Primary Migration in Shales." *Tectonophysics* 694: 268–79. https://doi.org/10.1016/j.tecto.2016.11.010.

Vales, F., D. Nguyen Minh, H. Gharbi, and A. Rejeb. 2004. "Experimental Study of the Influence of the Degree of Saturation on Physical and Mechanical Properties in Tournemire Shale (France)." *Applied Clay Science* 26 (1–4 SPEC. ISS.): 197–207.

https://doi.org/10.1016/j.clay.2003.12.032.

van Oort E (2003) On the physical and chemical stability of shales. J Pet Sci Eng 38:213–235

Villamor Lora, Rafael, Ehsan Ghazanfari, and Enrique Asanza Izquierdo. 2016. "Geomechanical Characterization of Marcellus Shale." *Rock Mechanics and Rock Engineering* 49 (9): 3403–24. https://doi.org/10.1007/s00603-016-0955-7.

Volk LJ, Raible CJ, Carroll HB, Spears JS (1981) Embedment of high strength proppant into low-permeability reservoir rock. In: SPE/ DOE low permeability gas reservoirs symposium. Society of Petroleum Engineers, Denver

Wang, HanYi. 2016. "What Factors Control Shale Gas Production Decline Trend: A Comprehensive Analysis and Investigation." *SPE/IAEE Hydrocarbon Economics and Evaluation Symposium*, no. May: 32. https://doi.org/10.2118/179967-MS.

Warpinski, N. R., M. J. Mayerhofer, M. C. Vincent, C. L. Cipolla, and E. R. Lolon. 2009. "Stimulating Unconventional Reservoirs: Maximizing Network Growth While Optimizing Fracture Conductivity." *Journal of Canadian Petroleum Technology* 48 (10): 39–51. https://doi.org/10.2118/114173-PA.

Wilshire B, Burt H (2008) Damage evolution during creep of steels. Int J Press Vessels Pip 85:47–54

Wiseall, A. C., R. J. Cuss, E. Hough, and S. J. Kemp. 2018. "The Role of Fault Gouge Properties on Fault Reactivation during Hydraulic Stimulation; an Experimental Study Using Analogue Faults." *Journal of Natural Gas Science and Engineering* 59 (July): 21–34. https://doi.org/10.1016/j.jngse.2018.08.021.

Wu, Shan, Hongkui Ge, Xiaoqiong Wang, and Fanbao Meng. 2017. "Shale Failure Processes and Spatial Distribution of Fractures Obtained by AE Monitoring." *Journal of Natural Gas Science and Engineering* 41: 82–92. https://doi.org/10.1016/j.jngse.2017.02.015.

Yang, Shengyu, Brian Horsfield, Nicolaj L. Mahlstedt, Michael H. Stephenson, and Sven F.

Könitzer. 2015. "On the Primary and Secondary Petroleum Generating Characteristics of the Bowland Shale, Northern England." *Journal of the Geological Society, London* 173 (2): 292–305. https://doi.org/10.1144/jgs2015-056.

Yang Y, Zoback M (2016) Viscoplastic deformation of the Bakken and adjacent formations and its relation to hydraulic fracture growth. Rock Mech Rock Eng 49:689–698

Yu HD, Chen WZ, Gong Z, Tan XJ, Ma YS, Li XL, Sillen X (2015) Creep behavior of boom clay. Int J Rock Mech Min Sci 76:256–264

Zener, Clarence, and J. H. Hollomon. 1946. "Problems in Non-Elastic Deformation of Metals." *Journal of Applied Physics* 17 (2): 69–82. https://doi.org/10.1063/1.1707696.

Zhang C, Rothfuchs T (2004) Experimental study of the hydro- mechanical behaviour of the Callovo-Oxfordian argillite. Appl Clay Sci 26:325–336

Zhang J, Kamenov A, Zhu D, Hill D (2013) Laboratory measurement of hydraulic fracture conductivities in the Barnett Shale. In: International Petroleum Technology Conference. International Petroleum Technology Conference, Beijing

Zhang J, Ouyang L, Zhu D, Hill AD (2015) Experimental and numerical studies of reduced fracture conductivity due to proppant embedment in the shale reservoir. J Pet Sci Eng 130:37–45

Zhang D, Ranjith PG, Perera MSA (2016a) The brittleness indices used in rock mechanics and their application in shale hydraulic fracturing: a review. J Pet Sci Eng 143:158–170

Zhang J, Zhu D, Hill AD (2016b) Water-induced damage to propped- fracture conductivity in shale formations. SPE Prod Oper 31:147–156

Zhang, Xiaochun, Nathan P. Myhrvold, Zeke Hausfather, and Ken Caldeira. 2016. "Climate Benefits of Natural Gas as a Bridge Fuel and Potential Delay of Near-Zero Energy Systems." *Applied Energy* 167: 317–22. https://doi.org/10.1016/j.apenergy.2015.10.016.

Zoback, M.D. 2007. *Reservoir Geomehanics. First Edition.* Cambridge University Press.